

AD736720

ARL 71-0243
NOVEMBER 1971



Aerospace Research Laboratories

ON THE NEAR FLOW FIELD GENERATED BY THE SUPERSONIC FLOW OVER REARWARD FACING STEPS

JAIN-MING WU

MICHAEL W. SU

TREVOR H. MOULDEN

THE UNIVERSITY OF TENNESSEE SPACE INSTITUTE

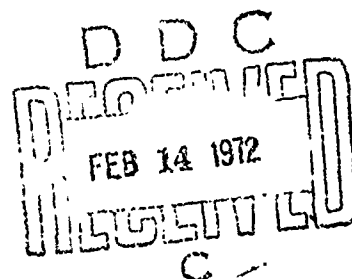
TULLAHOMA, TENNESSEE

CONTRACT NO. F33615-70-C-1645

PROJECT NO. 7063

Approved for public release; distribution unlimited.

Reproduced by
NATIONAL TECHNICAL
INFORMATION SERVICE
Springfield, VA 22151



AIR FORCE SYSTEMS COMMAND

United States Air Force

NOTICES

When Government drawings, specifications, or other data are used for any purpose other than in connection with a definitely related Government procurement operation, the United States Government thereby incurs no responsibility nor any obligation whatsoever; and the fact that the Government may have formulated, furnished, or in any way supplied the said drawings, specifications, or other data, is not to be regarded by implication or otherwise as in any manner licensing the holder or any other person or corporation, or conveying any rights or permission to manufacture, use, or sell any patented invention that may in any way be related thereto.

Agencies of the Department of Defense, qualified contractors and other government agencies may obtain copies from the

Defense Documentation Center
Cameron Station
Alexandria, Virginia 22314

ACCESSION FOR	
GPSTI	WHITE SECTION <input checked="" type="checkbox"/>
DDC	DIFF. SECTION <input type="checkbox"/>
UNANNOUNCED	<input type="checkbox"/>
JUSTIFICATION	
BY	
DISTRIBUTION AVAILABILITY CODES	
DIST.	AVAIL. STATE
A	

This document has been released to the

CLEARINGHOUSE
U. S. Department of Commerce
Springfield, Virginia 22151

for the sale to the public.

Copies of ARL Technical Documentary Reports should not be returned to Aerospace Research Laboratories unless return is required by security considerations, contractual obligations or notices on a specified document.

UNCLASSIFIED

Security Classification

DOCUMENT CONTROL DATA - R & D		
(Security classification of title, body of abstract and indexing annotation must be entered when the overall report is classified)		
1. ORIGINATING ACTIVITY (Corporate author) University of Tennessee Space Institute Tullahoma, Tennessee 37388		2a. REPORT SECURITY CLASSIFICATION UNCLASSIFIED
		2b. GROUP
3. REPORT TITLE Near Flow Field Generated by the Supersonic Flow over Rearward Facing Steps		
4. DESCRIPTIVE NOTES (Type of report and inclusive dates) Scientific - Final		
5. AUTHOR(S) (First name, middle initial, last name) Jain-Ming Wu Michael W. Su Trevor A. Moulden		
6. REPORT DATE November 1971	7a. TOTAL NO. OF PAGES 172 176	7b. NO. OF REFS
8a. CONTRACT OR GRANT NO. F33615-70-C-1645	8b. ORIGINATOR'S REPORT NUMBER(S)	
b. PROJECT NO. 7063-00-12		
c. DoD Element 61102F	9b. OTHER REPORT NO(S) (Any other numbers that may be assigned this report)	
d. DoD Subelement 681307	ARL 71-0243	
10. DISTRIBUTION STATEMENT Approved for public release; distribution unlimited.		
11. SUPPLEMENTARY NOTES TECH OTHER		12. SPONSORING MILITARY ACTIVITY Aerospace Research Laboratories (LV) Wright-Patterson AFB, Ohio 45433
13. ABSTRACT An investigation of the flow field generated by a rearward facing step at supersonic speeds has been conducted. Measurements were made and evaluated in the oncoming boundary layer, in the free shear layer, the lip shock and in the wake (or reattachment) shock region. Pitot and static pressure surveys were conducted, along with hot wire measurements and flow visualization studies. The measured free shear layer profiles were compared at different free stream Mach numbers, Reynolds numbers and step heights. A new technique was established for reducing the hot wire data. This was based upon the heat transfer correlation formula, and allows a broader range of applicability; in both the low Reynolds number region and in the free shear layer where the flow field is changing rapidly. This technique when applied to the measurements allowed the flow structure in the recirculating region to be explored. The low base pressure generated by the step influences the flow field ahead of the step and the extent of this upstream influence has been discussed. A new base pressure correlation parameter has also been developed for fully laminar and transitional flow.		

DD FORM 1 NOV 65 1473

UNCLASSIFIED

Security Classification

ARL 71-0243

**ON THE
NEAR FLOW FIELD GENERATED BY THE SUPERSONIC
FLOW OVER REARWARD FACING STEPS**

*JAIN-MING WU, MICHAEL W. SU, TREVOR H. MOULDEN
THE UNIVERSITY OF TENNESSEE SPACE INSTITUTE
TULLAHOMA, TENNESSEE*

NOVEMBER 1971

**CONTRACT NO. F33615-70-C-1645
PROJECT NO. 7063**

Approved for public release; distribution unlimited.

**AEROSPACE RESEARCH LABORATORIES
AIR FORCE SYSTEMS COMMAND
UNITED STATES AIR FORCE
WRIGHT-PATTERSON AIR FORCE BASE, OHIO**

FOREWORD

This technical report was prepared at the University of Tennessee Space Institute, Tullahoma, Tennessee. The research reported herein was conducted by Dr. J. M. Wu, Associate Professor of Aerospace Engineering at the University of Tennessee Space Institute, under contract to the Office of Aerospace Research, USAF. The contract was monitored by Dr. Max G. Scherberg of the Aerospace Research Laboratories.

The authors wish to acknowledge the benefits received from many fruitful discussions on all aspects of the work reported herein with Dr. Max G. Scherberg. Excellent cooperation and help from Mr. J. C. Donaldson, Project Engineer, and the staff at the von Karman Gas Dynamics Facility of the Arnold Engineering and Development Center, Arnold Air Force Station, Tennessee, is also acknowledged for their conducting of the wind tunnel tests. Some constructive suggestions on hot-wire techniques were received from Dr. C. Forbes Dewey, Jr. of Massachusetts Institute of Technology. Some contributions on data analysis by Dr. L. Wilhelm are also acknowledged.

ABSTRACT

An investigation of the flow field generated by a rearward facing step at supersonic speeds has been conducted. Measurements were made and evaluated in the oncoming boundary layer, in the free shear layer, the lip shock and in the wake (or reattachment) shock region. Pitot and static pressure surveys were conducted, along with hot wire measurements and flow visualization studies. The measured free shear layer profiles were compared at different free stream Mach numbers, Reynolds numbers and step heights.

A new technique was established for reducing the hot wire data. This was based upon the heat transfer correlation formula, and allows a broader range of applicability; in both the low Reynolds number region and in the free shear layer where the flow field is changing rapidly. This technique when applied to the measurements allowed the flow structure in the recirculating region to be explored.

The low base pressure generated by the step influences the flow field ahead of the step and the extent of this upstream influence has been discussed. A new base pressure correlation parameter has also been developed for fully laminar and transitional flows.

TABLE OF CONTENTS

ABSTRACT	PAGE NUMBER
1. Introduction	1
2. Experimental Techniques.	7
3. Improved Hot Wire Technique for Low Reynolds Number Compressible Flows.	18
4. Flow Upstream of Separation.	33
5. Flow Downstream of Separation	51
6. A New Base Pressure Correlation.	76
7. The Influence of an Overhang Mounted at the Separation Corner.	86
8. Hot-Wire Measurements in Recirculating Region and Free Shear-Layer	90
9. An Estimation of the Shear-Layer Temperature Distribution	101
10. The Wake Shock	113
11. Conclusions and Recommendations.	121
Bibliography	
Appendices	

LIST OF SYMBOLS

Nu	Nusselt number
Re	Reynolds number
I	current
R	hot wire resistance
A, B	constants in hot wire formula
M	Mach number
V	local flow velocity
Ku	Knudsen Number
T	Temperature
ψ	End loss correction factor; stream function
l	hot wire length
d	hot wire diameter
h	heat transfer coefficient
x, y	coordinate directions
m, n	coefficients in heat transfer equation (eq. 8)
ξ, η	see equations (16, 17)
μ	viscosity coefficient
k	thermal conductivity
p	pressure
H	step height
L	length from model leading-edge to stop
γ	ratio of specific heats
δ	boundary-layer thickness
ρ	density of air
u, v	velocity components along directions x, y

Δ	streamtube width
i, j	indexes
Re_c	reduced Reynolds number for base pressure correlation
A, D	functions in base pressure correlation (Fig. 35)
C_p	specific heat at constant pressure
Pr	Prandtl Number
τ	transformed temperature
f	Blasius stream function
β	wake shock angle
ν	Prandtl-Meyer angle
F, G	Functions in hot wire analysis
Q	heat flux

SUBSCRIPTS

m	measured values (current, resistance, etc.)
a	zero current values
aw	adiabatic wire temperature
∞	Free stream conditions
o	stagnation (pitot) conditions
ox oy }	stagnation conditions before and after shock wave
s	static conditions (pressure)
t	total (reservoir) conditions
b	value on base
r	radiation loss
h	corrective loss

SUPERSCRIPTS

(overbar) indicates non-dimensional values
fluctuating velocity components

LIST OF FIGURES

TITLE	PAGE
1. Flow Pattern for Supersonic Flow Over a Rearward Facing Step	2
2. Model Details	8
3. Splitter Plate Details	10
4. Combination Thermocouple Pitot Probe Details	11
5. Disk Static Pressure Probe Details	13
6. Hot-wire Anemometer Probe Details	15
7. Typical Wire Resistance Calibration	16
8. Typical Measurements in Recirculating Region	28
9. Overheat Effect on Reduced Heat Transfer Rate	29
10. Surface Pressure Distributions at $M_\infty = 2.5$	34
11. Surface Pressure Distributions at $M_\infty = 3.5$	35
12. Surface Pressure Distributions at $M_\infty = 5.0$	36
13. Correlation of Surface Pressure Upstream of Separation Corner	38
14. Typical Pitot Surveys of Approaching Boundary-Layer	40
15. Isentropic Streamtube Approximation	45
16. Estimated Mach number and Static Pressure Distribution at $M_\infty = 5.02$	48
17. Estimated Mach number and Static Pressure Distribution at $M_\infty = 3.5$	50
18. Typical Pitot Measurements in the Wake of a Backstep at $M_\infty = 3.5$	52
19. Pitot Pressure Profiles in and Above Recirculating Region	53

TITLE	PAGE
20. Pitot Pressure Profiles Around Separation Corner	54
21. Pitot Pressure Profile Immediately Downstream of Separation	56
22. Comparison of Measured Pitot Profiles with Prandtl-Meyer Expansion at $M_{\infty} = 2.5$	58
23. Comparison with Prandtl-Meyer Expansion at $M_{\infty} = 3.5$	59
24. Comparison with Prandtl-Meyer Expansion at $M_{\infty} = 5.0$	60
25. Comparison of Measured and Computed Pitot Pressures at $M_{\infty} = 3.5$	64
26. Comparison of Measured and Computed Pitot Pressures at $M_{\infty} = 5.07$	65
27. Typical Results of Inviscid Rotational Characteristics	66
28. Calculated Flow Properties Along Lip Shock by Inviscid Rotational Characteristics	68
29. Comparisons of Pitot Pressure Profiles for Different Reynolds numbers and Inviscid Flow Theory $M_{\infty} = 3.5$	69
30. Pitot Measurements of Different Reynolds Number Flow at $M_{\infty} = 2.5$	71
31. Shear Layer Mach Number Profiles for Different Reynolds Number Flows at $M_{\infty} = 2.5$	72
32. Comparison of Free Stream Mach Number Effects at a Fixed Reynolds Number	73
33. Influence of Step Height on Pitot Pressure Profiles	75
34. Parameters Pertinent to the Base Pressure Correlation	77
35. Base Pressure Correlation	82
36. Comparison of Measured Base Pressure and Base Pressure Computed from Correlation	84
37. Base Pressure Correlation for Six Degree Wedge	85
38. Surface Pressure Distributions With and Without Overhang at $M_{\infty} = 3.5$	87

TITLE	PAGE
39. Surface Pressure Distributions With and Without Overhang at $M_\infty = 2.5$	88
40. Continuous Hot Wire Resistance Mapping	91
41. Comparison Among Measured Hot-Wire, Pitot and Static Pressure Profiles	93
42. Typical Reduced Results From Hot Wire Measurements	95
43. Hot-Wire Recovery Temperature in Recirculating Region and Shear Layer	96
44. Hot-Wire Heat Transfer Coefficient in Recirculating Region and Shear Layer	97
45. Mach Number in Recirculating Region and Shear Layer	98
46. Stagnation Temperature in Recirculating Region and Shear Layer	100
47. Coordinate System for Shear Layer Calculations	102
48. Initial Profiles for Shear Layer Calculations Abiabatic wall conditions. $Pr = 0.72$	109
49. Development of Shear Layer Static Temperature Distribution (Equ. 52)	110
50. Comparison With Experimental Data	112
51. Wake Shock Data	114
52. Cavity Length Comparison	116
53. Properties of the Flow Model	118
54. Calculated Wake Shock Orientation	120
55. Pressure Recovery Distribution at $M_\infty = 2.5$	146
56. Pressure Recovery Distribution at $M_\infty = 3.5$	147
57. Pressure Recovery Distribution at $M_\infty = 5.07$	148
58. Comparison of Hot Wire Resistances at Three Input Currents	157
59. Recovery Factor in Transitional Regime	159

LIST OF TABLES

TITLE	PAGE
1. Base Pressure Correlation	81
2. Orifice Dimensions in Wind Tunnel Model	161

CHAPTER I

INTRODUCTION

It has been known for sometime that the development of the entire wake flow generated by a blunt-base slender body at supersonic and hypersonic speeds depends to a great extent on the characteristics of the near wake [1, 2].¹ Thus, the near wake problem has been the subject of intensive studies in recent years. The importance of the detailed understanding of near wake for far wake studies can be illustrated by the fact that the separated boundary layer cannot be entrained by the recirculating region and must pass downstream into the far wake. A description of the flow region is shown in Figure 1.

The near wake is in essence a strong interaction problem. For example, the base pressure determines the degree of expansion and separation for the approaching boundary layer, while the separation process and the free shear layer growth provide the conditions before the recompression process, which, in turn, determines the base pressure, the free shear layer controls the structure of the recirculating region. Therefore, the free shear layer,

¹Numbers in brackets refer to similarly numbered references in the bibliography.

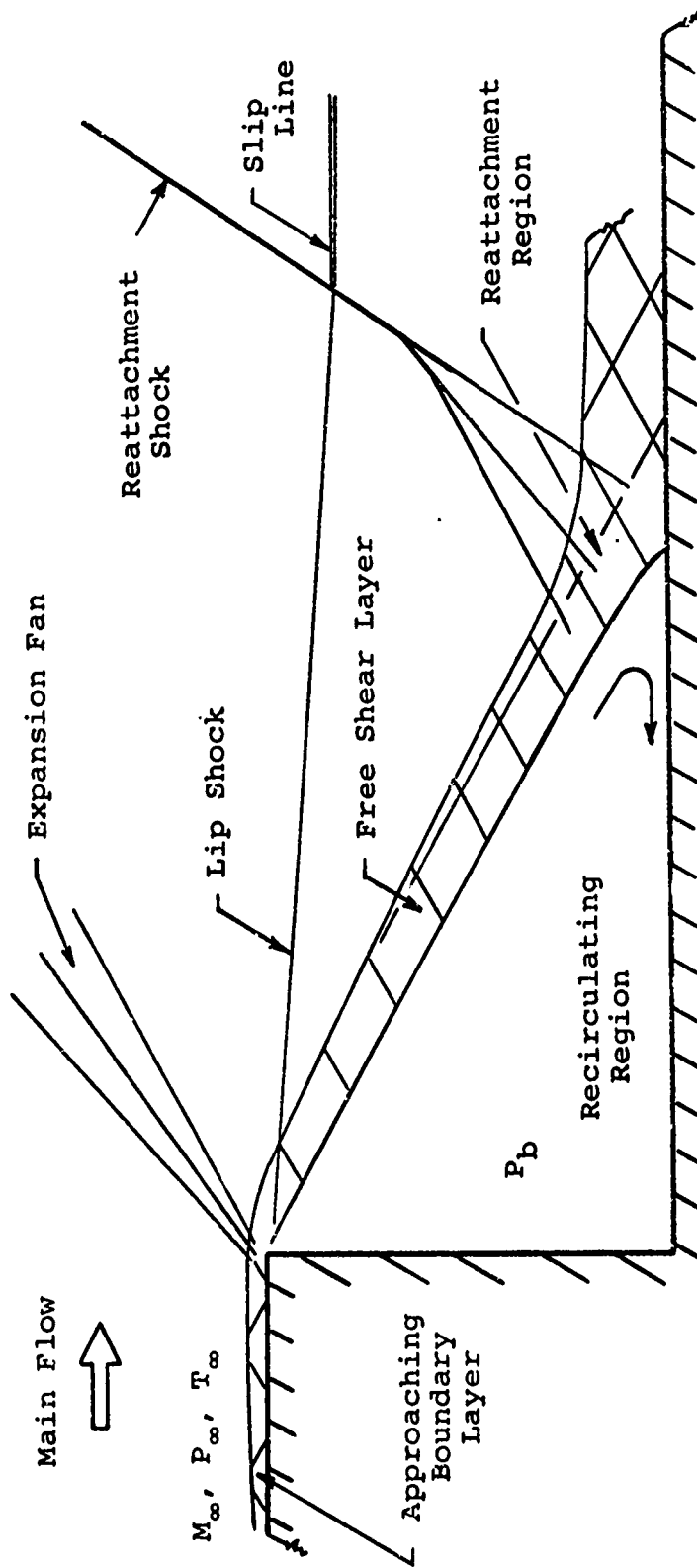


Figure 1. Flow Pattern for Supersonic Flow over a Rearward Facing Step.

the recirculation and the neck regions are intimately coupled with one another. The final solution to this problem depends on the balance of these regions.

The fundamental difficulty in near wake problems lies in the fact that the well established asymptotic techniques, that form the backbone of fluid mechanics, cannot be applied with confidence. For instance, the boundary layer theory cannot be applied in the expansion corner and the recirculating region. Only the Navier-Stokes equations are adequate to describe the complete flow field. However, a successful numerical solution to these equations seems not to be feasible in the near future. New avenues must be attempted in establishing a physically realistic model. It is, therefore, very necessary to experimentally describe the detail flow structure in order to determine the relative importance of these flow regions and to verify the existing theoretical models.

It was Chapman [3] who first recognized the importance of the free shear layer shed from the body surface. He introduced the concept of "dividing streamline" separating the recirculating fluid from the fluid entrained by mixing with the external uniform inviscid flow. However, the uniform parallel inviscid flow is a severe idealization of the corner expansion process, which is valid only when the oncoming boundary layer thickness is very thin or the free stream Reynolds number is very large.

Crocco and Lees [4] proposed the concept that the compression in the near wake at supersonic speed is a smooth viscous-inviscid interaction phenomenon rather than a sudden isentropic process as assumed by Chapman. The mixing between the internal dissipative flows and the external nearly isentropic streams is regarded as a fundamental physical process. Their theory shows the proper variation of base pressure with Reynolds number; however, in order to bring out the main aspects of their theory, the treatments of the recirculating flow and the corner expansion process were somewhat crude.

The problem of upstream influence of the low base pressure has been investigated by Scherberg & Smith [18], Baum [5], Olsson and Messiter [6], and Weiss and Nelson [7]. The problem of expansion and separation of the approaching boundary layer in the neighborhood of a sharp corner at the base has been studied by Scherberg & Smith [18], Hama [8], Weiss and Weinbaum [9], Adamson [10], and Zakky [11]. The recirculating region has been attacked by Batchelor [12], Burggraf [13], Weiss [14], Scherberg [15], Roache [16], and Erdos and Zakky [17]. Despite the strong interacting (or coupling) nature of the near wake, so far, the problems on separation corner, free shear layer and recirculating region have been mainly analytically examined independently of each other. The application of inviscid theory to determine the expansion around a separation corner remains to be justified by experiments. There

appears to be a controversy [8] as to cause of the lip shock. The effects of the expanded boundary layer on the development of the inner free shear layer and the structure of the recirculating region have not been investigated rigorously. No attempt has been made to correlate the base pressure for the transitional flow up to date. Many valuable experimental investigations in the near wake of a blunt-based slender body have been conducted by Scherberg and Smith [18], Batt and Kubota [19], Roshko and Thomke [20], Lewis and Behrens [21], Todisco and Pallone [22], Rom [23], Charwat and Yakura [24], and many others. However, more information is still needed in the regions of the upstream influence, corner expansion, free shear layer and the recirculating flow.

The objectives of this investigation are to study experimentally:

1. The upstream influence, the corner expansion process, and the comparisons with the characteristics solution and with the Prandtl-Meyer theory.
2. The basic characteristics of the recirculating region.
3. The effects of Reynolds number, Mach number and step height on the separated boundary layer.
4. The geometry of the reattachment, or wake, shock.

The upstream influence of the low base pressure was studied through the use of very densely distributed surface

pressure measurements and pitot surveys of the approaching layer. Very extensive pitot surveys were conducted immediately downstream of the corner to study the rapid expansion process and the formation of the lip shock. The free shear layer growth was also investigated by pitot pressure measurements. Because much experimental information has been accumulated at $M_\infty = 3.5$, $Re_{\infty,L} = 1.0 \times 10^6$, the hot-wire measurements were conducted at this condition.

Hot-wire anemometer probes were used to obtain the absolute velocity and total temperature in the recirculating region and the free shear layer. The Reynolds number based on wire diameter is not only very low in the recirculating region but also changes very abruptly across the free shear layer. Because of the wide range of application (M , Re_0) and the complicated heat transfer formula, it is almost impossible to apply the conventional hot-wire technique. Therefore, a simplified data reduction method was developed for this investigation.

This experimental investigation is part of the Separated Flow Program, Aeronautical Research Laboratory, (ARL), Thermodynamics Division, Wright-Patterson Air Force Base, Ohio, and a continuation of the research efforts of Rom [23] and Scherberg and Smith [18]. The test model, pitot-probe and hot-wire holders were designed and built at the ARL. Many pitot-pressure surveys analyzed in this study were also conducted by Smith [25] during the previous test program. Some results of this investigation were presented by Wu, Su and Scherberg [26].

CHAPTER II

EXPERIMENTAL TECHNIQUES

1. WIND TUNNEL DESCRIPTION

Tests were conducted in Tunnels A and D of the von Karman Gas Dynamics Facility (VKF) at the Arnold Engineering Development Center (AEDC) [27]. Tunnel A is a continuous, closed-circuit, variable density supersonic wind tunnel with an automatically driven, flexible plate-type nozzle and a 40 by 40 inch test section. The tunnel can be operated at Mach numbers from 1.5 to 6 and unit Reynolds numbers per inch between 0.025×10^6 and 0.59×10^6 .

Tunnel D is an intermittent supersonic wind tunnel with a manually adjusted, flexible-plate-type nozzle and a 12 by 12 inch test section. The tunnel operates at Mach numbers from 1.5 to 5.0, at stagnation pressures from 5 to 60 psia and at stagnation temperatures up to about 80°F.

2. WIND TUNNEL MODELS

The model for Tunnel A is shown in Figure 2. It is a two-dimensional rearward facing step model, 9 inches wide with variable step heights of 0.443 and 0.75 inches and it is the same model as used in the earlier tests [25, 28, 29, 30]. Sideplates, fitted with optical quality glass windows, were attached to the model to obtain approximately

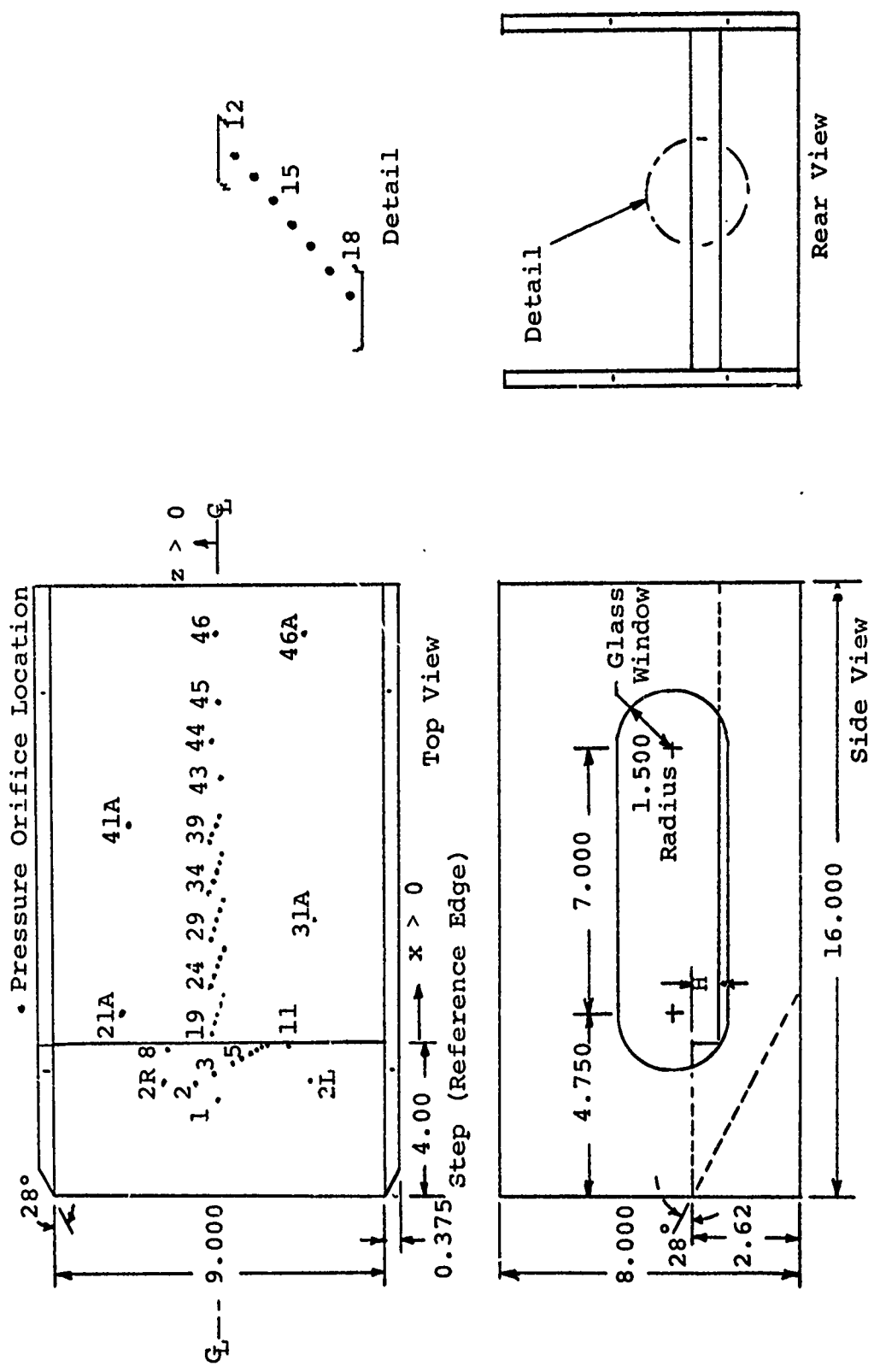


Figure 2. Model Details.

two-dimensional flow. The diameter of the leading edges of the model and sideplates were less than 0.002 inch. The maximum Reynolds number based on tunnel free stream conditions and the leading edge diameter was 1000. Eleven pressure orifices were located on the model top surface, 34 on the lower reattachment wall and seven on the vertical step face, dimensions of pressure orifices are specified in Appendix G. A longitudinal vertical splitter plate instrumented with 22 orifices was used for static pressure measurements in and near the recirculating region, the details are shown in Figure 3.

The model for the Tunnel D testing was furnished by VKF, AEDC. This model spanned the test section and was 12 inches wide and did not have sideplates. The height of the step could be adjusted to 0.75 inch and 0.225 inch. A splitter plate was used for oil flow studies and static pressure measurement [28].

3. PITOT PRESSURE MEASUREMENTS

The model boundary layer, expansion region and free shear layer were surveyed with a flattened combination pitot-thermocouple probe. The probe is 0.01 inch high and with a 0.004 inch by 0.06 inch opening, see Figure 4. The probe was always pointed upstream and parallel to the free stream direction. No attempt has been made to correct the errors due to flow inclination

All dimensions in inches

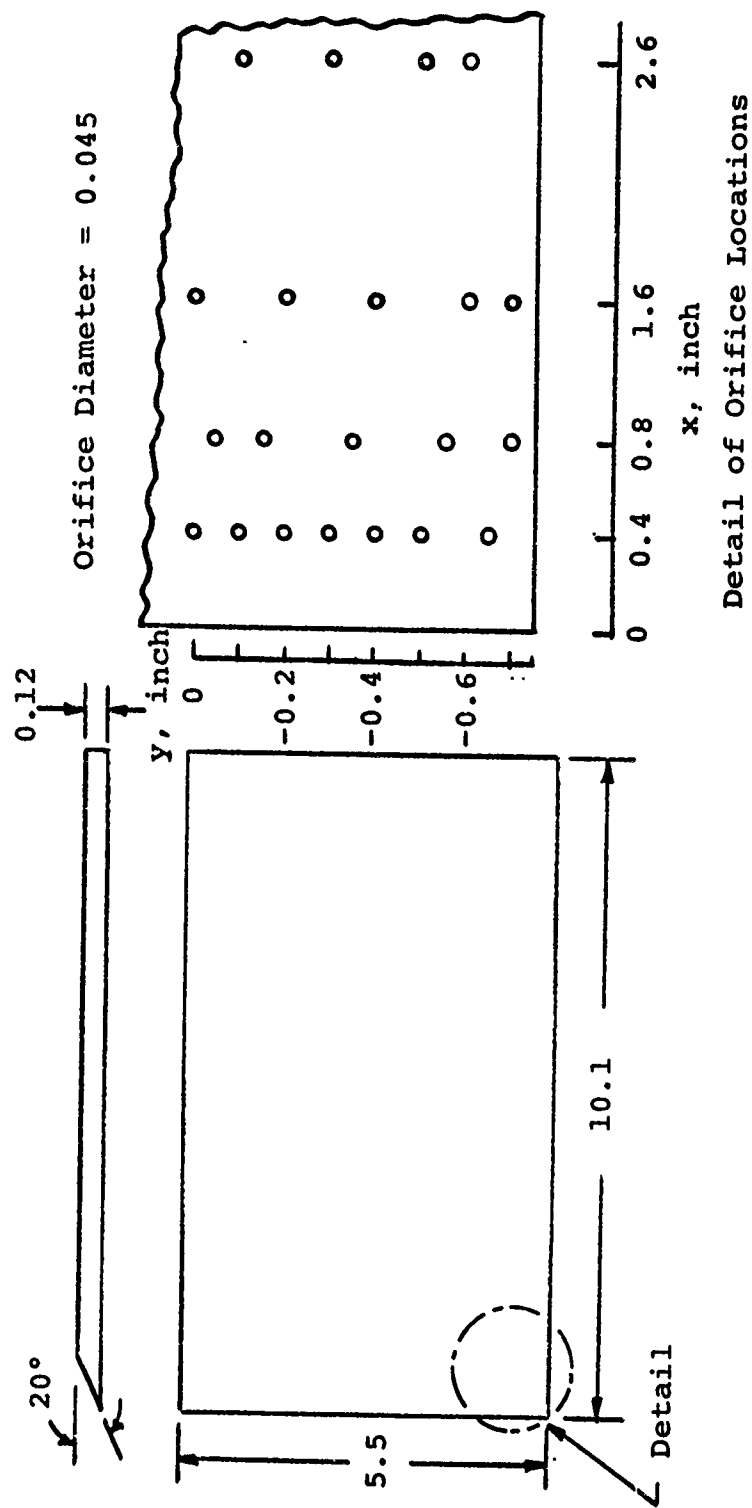


Figure 3. Splitter Plate Details.

All dimensions in inches

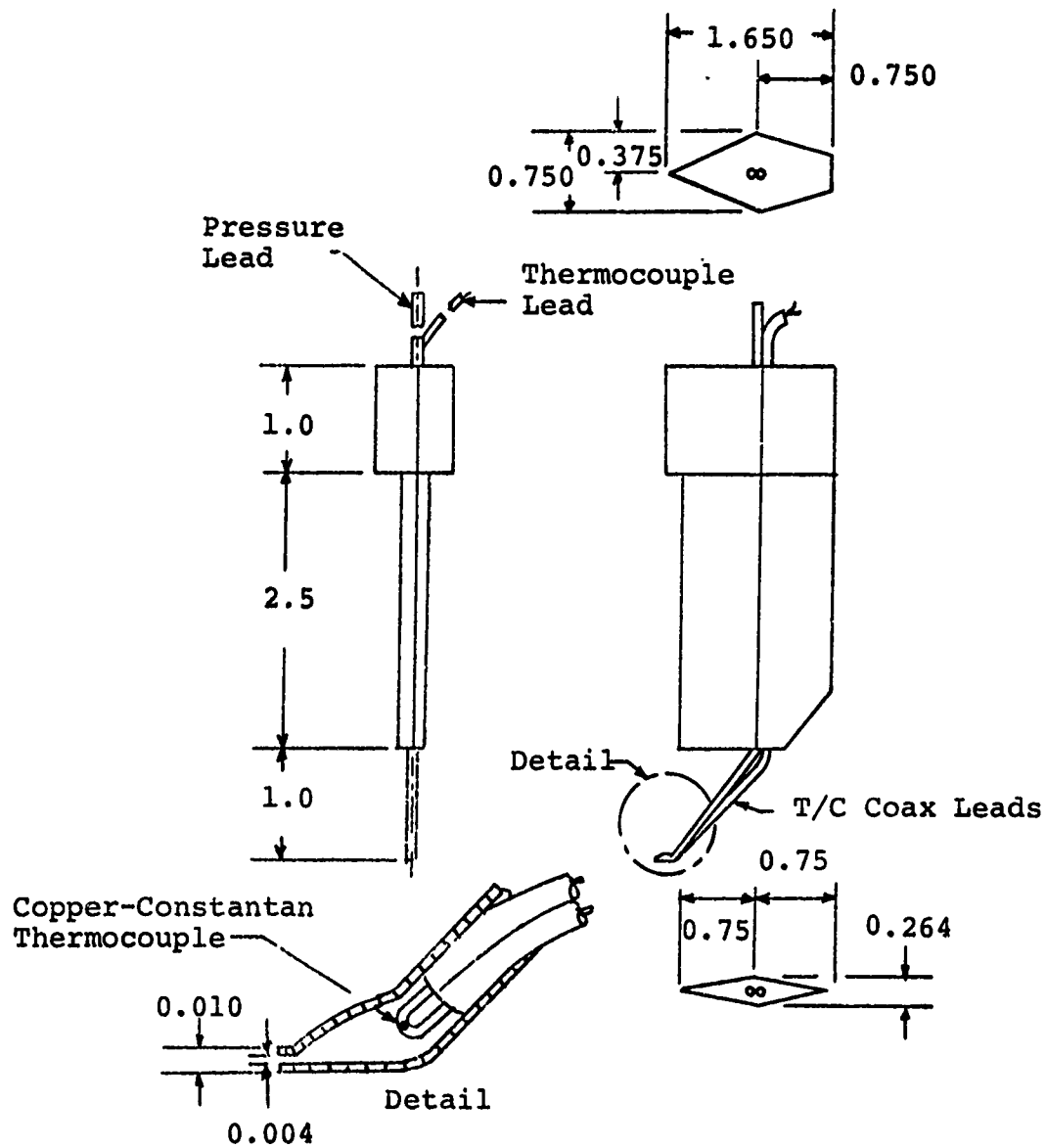


Figure 4. Combination Thermocouple Pitot Probe Details.

and low Reynolds number. The height of the probe centerline can be varied with an accuracy of ± 0.001 inch.

The pitot pressure measurements were made with a 15-psid transducer calibrated for ranges of 15, 5, 1, and 0.3 psia. Whenever possible, a near vacuum reference was used; otherwise, a 2-psid reference was employed. The transducer is considered to be accurate to within ± 1.0 percent of the range used.

4. STATIC PRESSURE MEASUREMENTS

Limited static pressure profiles were conducted with a 0.25 inch diameter "disk type" probe. A 0.047 inch diameter orifice was located at the center of the disk as shown in Figure 5. Because of the relatively large orifice diameter, the measurements are not accurate in the regions of abrupt pressure changes such as the expansion region. Static pressure measurements were made with a 5-psid transducer reference to a near vacuum. The transducer was calibrated for ranges of 2.0, 1.0, and 0.3 psia, and was considered to be accurate to within ± 1.0 percent of the range used.

Model surface pressures were measured with a pressure scanning system which used 15-psid or 5-psid transducers reference to a near vacuum. The 15-psid transducers were calibrated for ranges of 5 and 1 psia, and were considered accurate to within ± 0.4 and ± 1.0 percent,

All dimensions in inches

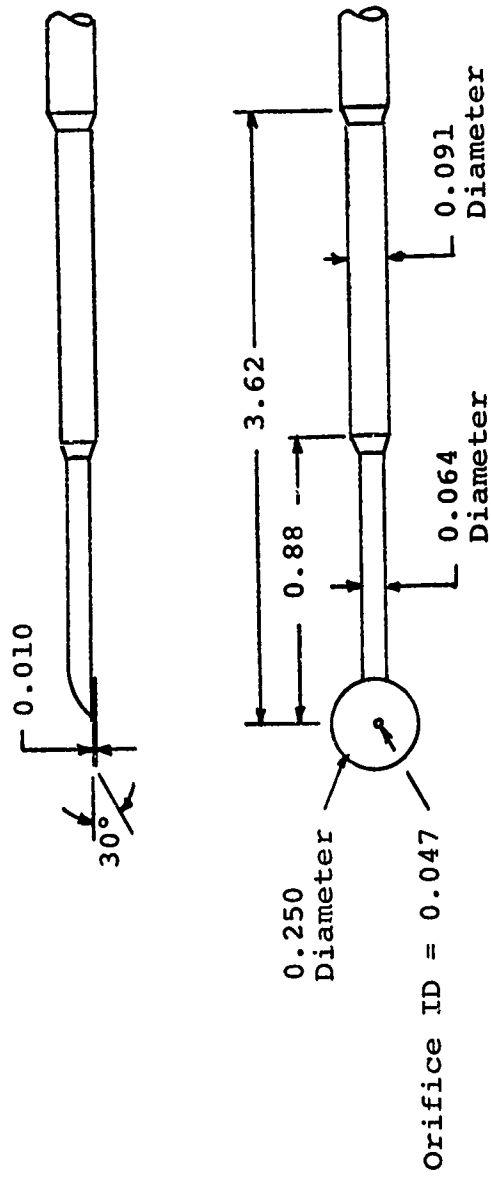


Figure 5. Disk Static Pressure Probe Details.

respectively, of the full scale of the range used. The lower surface pressures, such as base pressure, were measured with the pressure scanning system using 5-psid transducers reference to a near vacuum. The transducers were calibrated for ranges of 5, 1.67, and 0.33 psia. These transducers were considered accurate to within ± 0.2 , ± 0.3 , and ± 1.0 percent, respectively, of the range used.

5. HOT-WIRE MEASUREMENTS

The hot-wire holders as shown in Figure 6 were designed so that the measuring wire was offset from the supporting stem which was made [25] long and thin to cause minimum disturbance to the flow structure. Each probe consisted of platinum - 10 percent rhodium wire approximately 0.00022 inch in diameter and 0.065 inch in length. A thermocouple was attached to one needle of each probe approximately 0.1 inch from the tip to measure the temperature of the wire support. All wires were annealed and calibrated following the method outlined by Dewey [31]. From these calibration measurements, the linear temperature resistance relation was obtained as shown in Figure 7.

The hot-wire measurements were made using constant current equipment of Shapiro-Edwards design. Wire resistance was measured by a precision bridge with an accuracy of ± 0.01 ohm. Wire heating currents were set, using a precision potentiometer with ranges of 0.1 amp and 0.01

All dimensions in inches

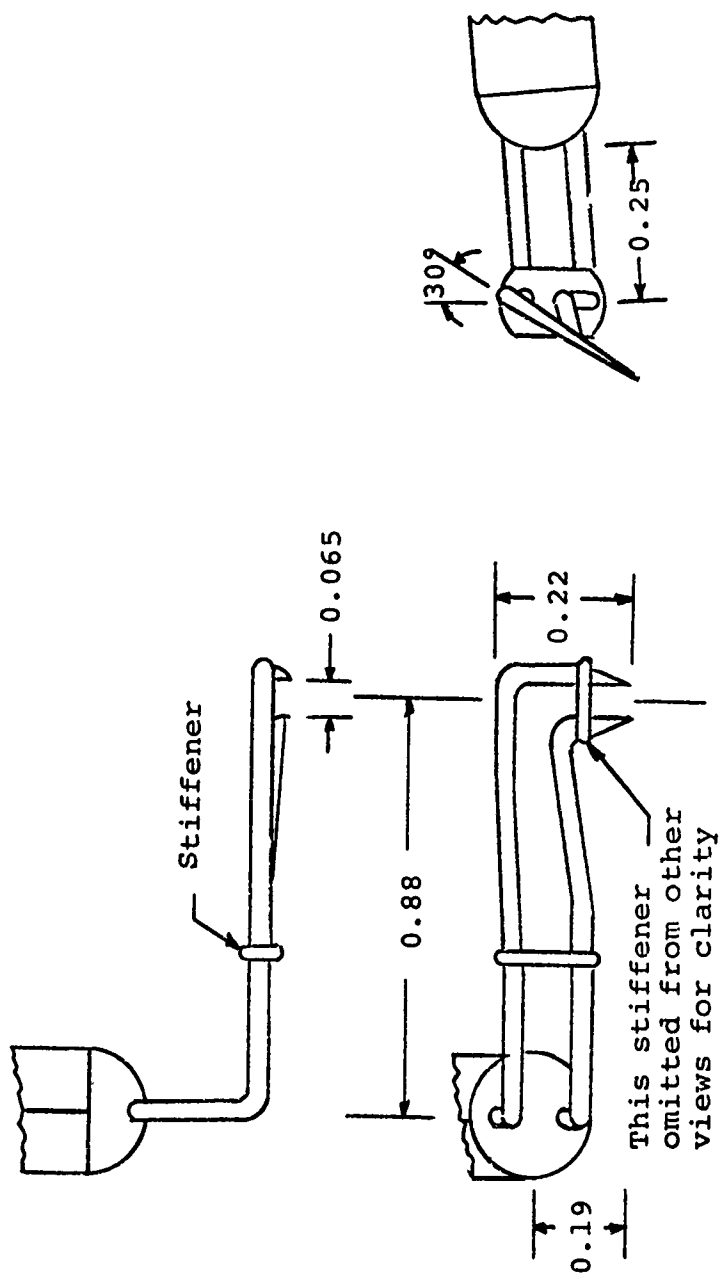


Figure 6. Hot-Wire Anemometer Probe Details.

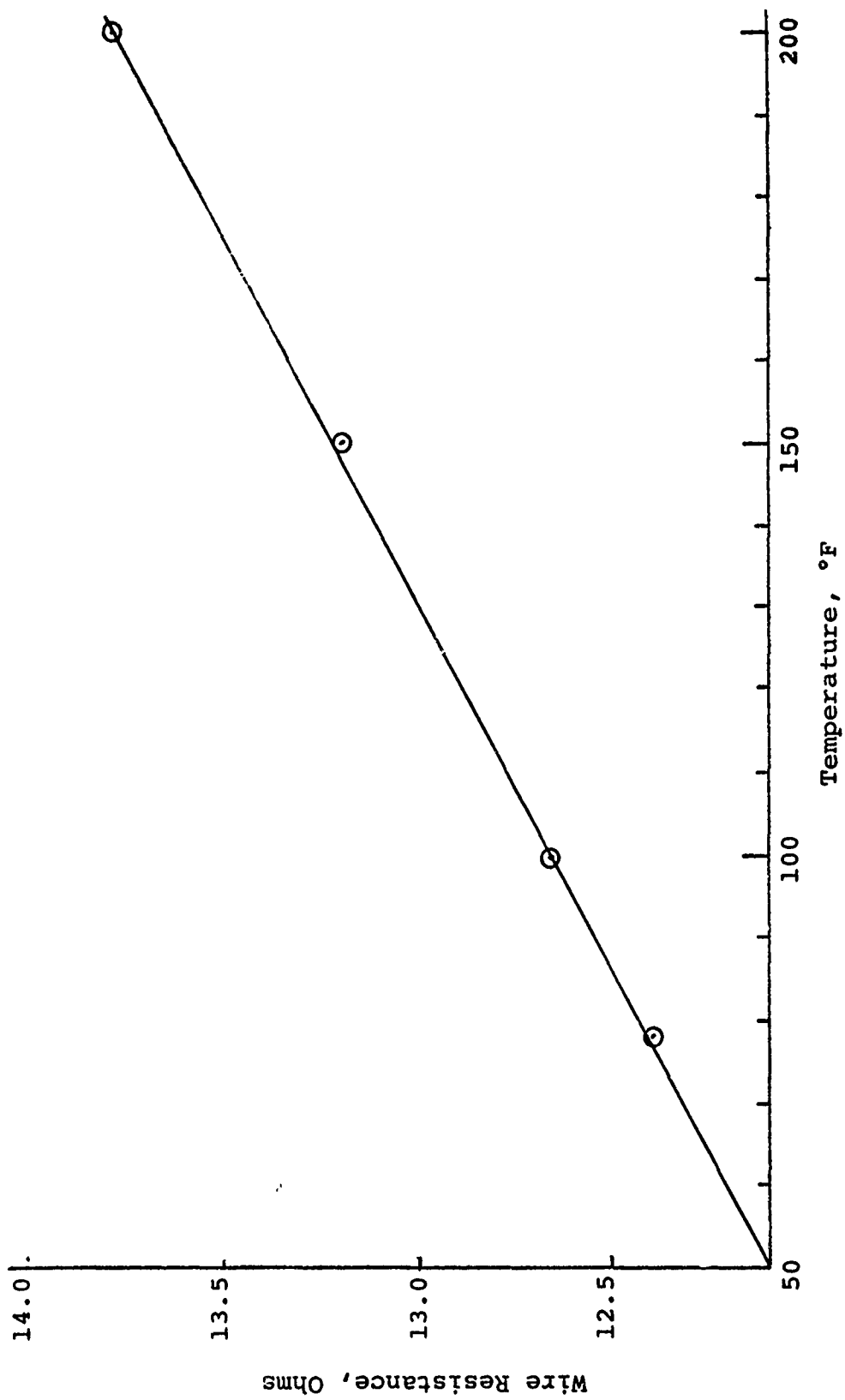


Figure 7. Typical Wire Resistance Calibration.

amp full scale with an accuracy of ± 0.1 percent of full scale. The measurements of wire support temperature were accurate to within ± 1.0 degree.

CHAPTER III

IMPROVED HOT-WIRE TECHNIQUE FOR LOW REYNOLDS NUMBER COMPRESSIBLE FLOWS

1. GENERAL DISCUSSION ON HOT-WIRE TECHNIQUES

The hot-wire methods have been used for a number of years to measure the mean or fluctuating flow properties of a fluid stream. The basic principle of the hot-wire method may be stated as follows. If a small wire is placed in a moving medium and heated to a temperature higher than that of the medium, there will be heat transfer from the wire to the flow. The rate of heat exchange depends on the geometrical and physical properties of the wire, the physical characteristics of the medium, the Joule heating, and the flow conditions. From the measured rate of heat exchange, one can determine the flow condition. The fundamental information needed in order to use a hot-wire probe is the governing law of heat transfer from a single fine wire under the conditions of which the measurements will be performed.

The dependence of the Nusselt number on the Reynolds number for incompressible flow was first established by King [32]. He found that the Nusselt number, Nu , is a linear function of the square root of the Reynolds number, Re , i.e.,

$$Nu = A + B Re^{1/2} \quad (1)$$

where A and B are constants. This equation may be reduced to:

$$\frac{I_m^2 R_m}{R_m - R_a} = A' + B' V^{1/2} \quad (2)$$

where I_m is the current passing through the wire at the wire resistance R_m , R_a is the wire resistance at zero current, A' and B' are constants and V is the velocity of the flow.

From Equation (2), one knows that once A' and B' are experimentally calibrated, the velocity V can be determined if $(I_m^2 R_m)/(R_m - R_a)$ is measured. For compressible flow, Equation (1) takes a more complicated form [33], i.e.,

$$Nu = A + B(M) Re^{1/2} \quad (3)$$

where B, previously a pure constant, is now a function of the flow Mach number M. Consequently, the calibration process is more complicated. Now, if the flow density is very low such that in the region of the slip or the free molecular flows, the functional relationship between Nusselt and Reynolds numbers becomes very complicated. Also, at very low Reynolds number, the velocity induced by buoyancy may be of greater importance. The natural convection shall be included in the heat transfer analysis.

Neglecting natural convection, Dewey [34] gave the following functional relationships:

$$Nu_o = A(Re_o) B(Re_o, M) Re_o^N(Re_o) \quad (4)$$

$$T_{aw} = T_{aw}(M, Kn) \quad (5)$$

where

$$Re_o = Re_o(M, T_o, p_s)$$

$$Kn = \frac{\pi \gamma}{2}^{1/2} \frac{M}{Re_\infty}$$

The detail expressions are very much involved, and will be discussed later. One realizes that it may not be wise to attempt the calibration technique. A new method must be developed to overcome this difficulty.

Most of the hot-wires are of a rather fine wire; their length-to-diameter ratio usually varies from 100 to 300. The wire materials, on the other hand, are good heat conducting metals. A substantial portion of the heat generated in the wire is conducted away toward the cooler ends of the wire supports. In order to obtain the correct value of heat transferred by convection to the surrounding air, this conduction heat loss must be separated from the total heat loss.

In the continuum flow, the conductive heat loss is usually only a small fraction of the convective heat loss,

if the wire length-to-diameter ratio ℓ/d exceeds 100. The end loss can be taken into account as a correction factor. It only modifies the total heat loss by a constant factor which is almost independent of the flow velocity. However, in the low density flows, the end loss encountered may be very appreciable even for a large ℓ/d case. To obtain a reliable and meaningful result, great care must be exercised when the end loss correction technique is employed. A hot-wire calibrated in a uniform flow has the end loss effect included in the calibration. However, if the probe supports are subjected to a large temperature gradient, the support temperature is different from that for uniform flow, and the change in end losses will invalidate a calibration made in uniform flow. It then becomes necessary to calculate the end losses with the measured support temperature.

Dewey [31] developed an end loss correction technique for the hot-wire measurements in low Reynolds number hypersonic flow. The end loss correction factors, ψ_N and ψ_R were derived in terms of Nu_0 , then ψ_N , ψ_R and the empirical heat transfer correlation formula were coupled to solve for flow field parameters. Also, the expression for ψ_N is formulated with some approximations. Because the method of successive substitution was used to solve the simultaneous equations, the calculation was found to

be nonconvergent for $M < 1.5$ [35]. Dewey's technique is reviewed in Appendix A.

If one is interested in the hot-wire measurement in the low Reynolds number supersonic or subsonic flow where the end correction is even more important, one must keep in mind that approximations shall be kept at a minimum whenever possible, and that any approximations employed need careful justification.

One of the objectives of this investigation is to explore the basic characteristics of the recirculating region by hot-wire measurements. The recirculating region was once considered a "dead air" region. The velocities in a portion of this region are low subsonic and the Reynolds number based on the hot-wire diameter is also very low. In order to obtain meaningful measurements, a direct and more simple technique was developed to determine the convective heat transfer coefficient h and the recovery temperature T_{aw} of the wire [36]. This technique, of course, is applicable to the supersonic and hypersonic flows as well.

2. DIRECT DETERMINATION OF h AND T_{aw}

As discussed in the last section, if one follows Dewey's approach, one must solve the following two equations simultaneously for the flow field parameters:

$$T_{aw}(M, Kn) = T_{aw_m} \psi_R (Nu_O)$$

$$Nu_O(M, Re_O) = Nu_m \psi_N (Nu_O)$$

Because of the complicated relationship of the above equations, the method of successive approximation may not always produce convergent solutions to the system of equations. Also, the approximations for ψ_N may introduce error in low Reynolds number supersonic or subsonic flow.

It will be shown that:

1. The end loss correction factors, ψ_N and ψ_R , are not really necessary for the hot-wire data reduction, and the approximations required to obtain ψ_N can be eliminated.
2. h and T_{aw} can be reduced directly from the hot-wire measurements, i.e.,

$$h = h(R_m, I_m)$$

$$T_{aw} = T_{aw}(R_m, I_m)$$

3. The flow field parameters can be solved much easier from the following two equations:

$$T_{aw} = T_{aw}(M, Kn)$$

$$hd/k_O = Nu_O(M, Re_O)$$

Parts 1 and 2 above are discussed in this section, and part 3 will be discussed in the next section.

The steady state heat balance at any section of a finite wire is

$$I_m^2 R + \left(\frac{\pi d^2 \ell}{4}\right) k_w \frac{d^2 T}{dx^2} = \pi d \ell h (T - T_{aw}) \quad (6)$$

Where the right hand side of the equation represents the convective heat loss, the second term on the left hand side is the heat loss by conduction, and $I_m^2 R$ is the Joule heating. This equation involves the following assumptions:

1. The convective heat transfer coefficient, h , is a constant and is equal to the value which would be measured by an infinite wire at the same current. This implies that the external flow is uniform along the wire.
2. The adiabatic wire temperature, T_{aw} , is a constant and is equal to the value of an infinitely long wire.
3. Natural convection and radiation are negligible.
4. The wire thermal conductivity is independent of temperature within the heated range.
5. Wire thermal resistance varies linearly with temperature, i.e.,

$$R = a + bT \quad (7)$$

and R is the resistance of the wire of length ℓ .

6. Each cross-section of the wire is at uniform T , h and T_{aw} .

The heat transfer equation can be rearranged as

$$\frac{d^2 T}{dx^2} - m^2 T + n = 0 \quad (8)$$

where

$$n = \frac{4(\pi d l h T_{aw} + a I_m^2)}{\pi d^2 l k_w} \quad (9)$$

$$m^2 = \frac{4(\pi d l h - b I_m^2)}{\pi d^2 l k_w} \quad (10)$$

and the boundary conditions are $T = T_s$ at $x = \pm l/2$ where T_s is the temperature of the supports. The solution to the above equation is

$$T = \frac{n}{m^2} - \left(\frac{n}{m^2} - T_s \right) \frac{\cosh mx}{\cosh ml/2} \quad (11)$$

and the measured resistance of the wire is

$$R_m = \frac{2}{l} \int_0^{l/2} R(T) dx = a + b \frac{n}{m^2} - \frac{b(n/m^2 - T_s)}{ml/2} \tanh \frac{ml}{2} \quad (12)$$

Note that h and T_{aw} are the two unknowns that one wishes to determine from the hot-wire measurements. h and T_{aw} are related to the measurable R_m and I_m by the above nonlinear algebraic equation. If two wire resistances are measured

at two different currents, two equations may be obtained from Equation (12) to determine h and T_{aw} , i.e.,

$$R_{m_1} = R_{m_1}(h, T_{aw}, I_{m_1})$$

$$R_{m_2} = R_{m_2}(h, T_{aw}, I_{m_2})$$

By operating at several currents, many pairs of equations can be solved for h and T_{aw} . However, as observed by Vrebalovich [37], the solutions depend on the degree of wire heating.

This problem can be overcome by calculating h and T_{aw} with the measurements corresponding to the no overheating condition, i.e., $I \rightarrow 0$. The following two equations can be obtained from Equation (12):

$$R_m \Big|_{I \rightarrow 0} = (a + b T_{aw}) - \frac{b(T_{aw} - T_s) \tanh S}{S} \quad (13)$$

$$\begin{aligned} \frac{dR_m}{dI_m^2} \Big|_{I \rightarrow 0} &= b \left(\frac{a + b T_{aw}}{\pi d l h} \right) \left(1 - \frac{\tanh S}{S} \right) \\ &+ \frac{b^2 (T_{aw} - T_s)}{2S} \left(\frac{\operatorname{sech}^2 S}{\pi d \sqrt{h d k_w}} - \frac{\tanh S}{\pi d l h} \right) \end{aligned} \quad (14)$$

where

$$S = \frac{l}{d} \sqrt{h d / k_w} \quad (15)$$

and a plot of R_m versus I_m^2 allows the quantities

$$\left. \frac{dR_m}{dI_m^2} \right|_{I \rightarrow 0}, \quad R_m \Big|_{I \rightarrow 0}$$

to be extrapolated from the measurements which are shown in Figure 8. Equations (13) and (14) can be solved for h and T_{aw} , the details are described in Appendix B. Typical results computed with and without overheat are shown in Figure 9.

3. REDUCTION OF FLOW PROPERTIES

It is shown that the hot-wire is capable of providing two thermodynamic measurements: h and T_{aw} . If sufficiently accurate relations are also known to relate them to the other parameters of the flow (such as Mach number and Reynolds number), the flow field parameters can be defined if another thermodynamic measurement such as the static or pitot pressure is conducted.

Because of the wide range of Mach numbers and Reynolds numbers encountered (from the shear layer to the recirculating region), it is necessary to have the analytical expressions for the empirical correlations suitable for computer calculation. The correlation formula proposed by Dewey was employed, because the accuracy of his expressions is superior to several of the earlier correlation relations [34]. The Nusselt number and

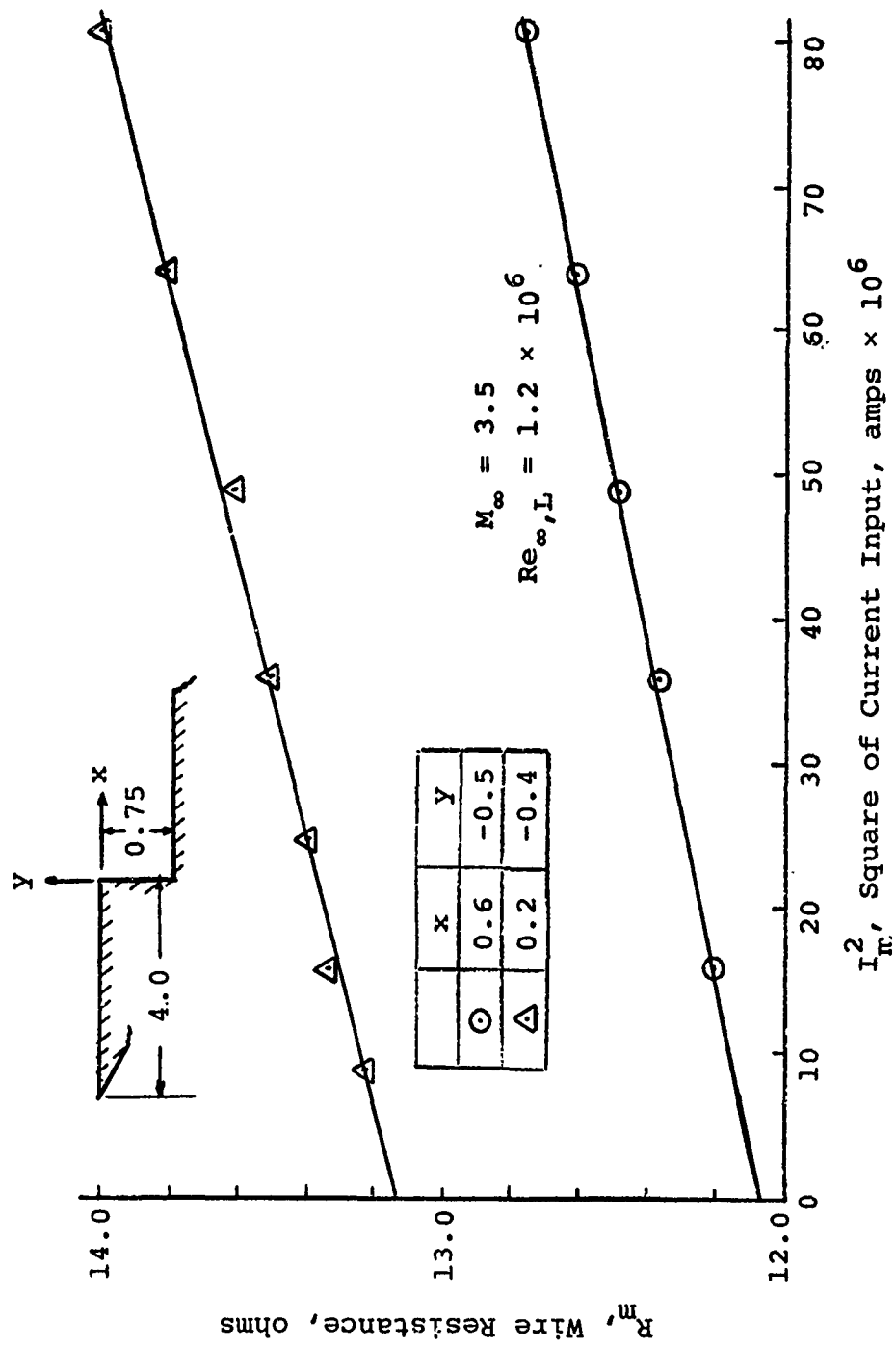


Figure 8. Typical Measurements in Recirculating Region.

$M_\infty = 3.5$
 $Re_{\infty, L} = 1.2 \times 10^6$
 $L = 4.0$ inches
 $H = 0.75$ inch

	x	y
○	0.2	-0.4
▽	0.4	-0.4
□	0.6	-0.4
◇	1.0	-0.5

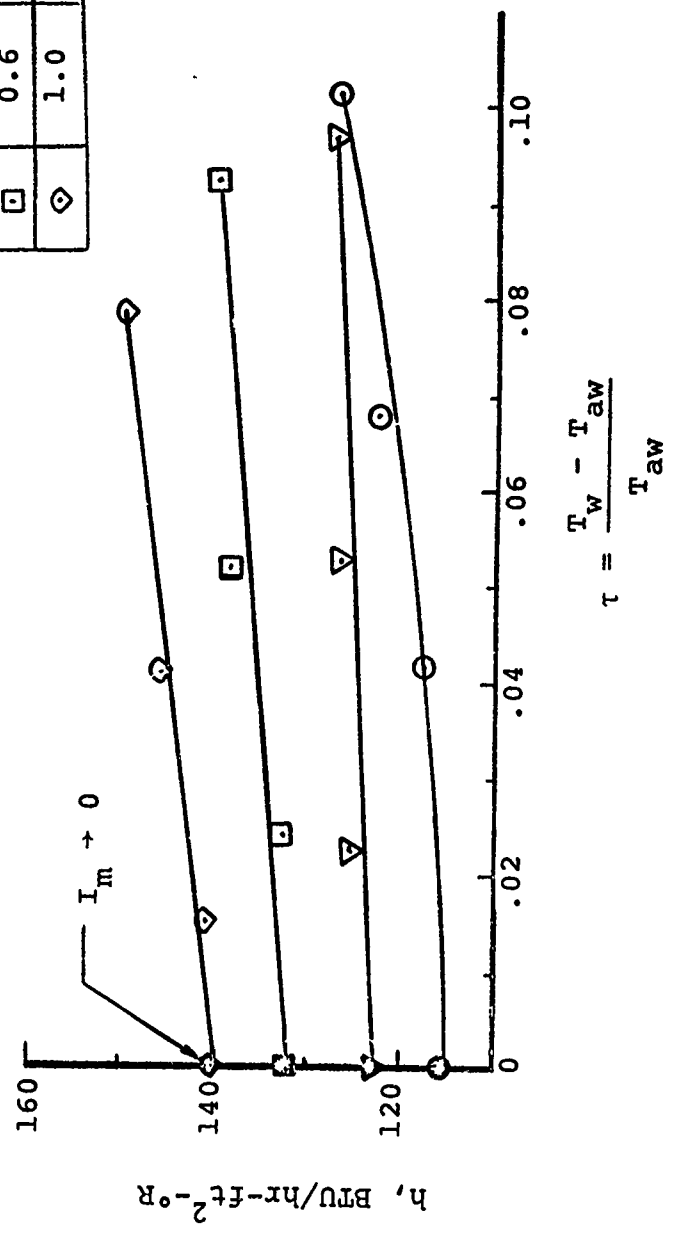


Figure 9. Overheat Effect on Reduced Heat Transfer Rate.

recovery factor are related to the Reynolds number and Mach number by the following expressions:

$$Nu_O(Re_O, M) = \xi(Re_O, \infty) \psi(Re_O, M) \quad (16)$$

$$\eta(M, Kn) = \frac{T_{aw}}{T_O} = \eta_c + \bar{\eta}_* (\eta_f - \eta_c) \quad (17)$$

in the range $2 \times 10^{-2} < Re_O < 10^3$ and $M > 0.2$, where $\xi(Re_O, \infty)$ represents the heat transfer correlation at the hypersonic Mach number as a result of the hypersonic "freeze." η is the ratio of wire recovery temperature to the free stream stagnation temperature, and the subscripts f and c denote free molecular and high Reynolds number continuum limits respectively.

The Nusselt number varies monotonically from the continuum heat transfer law $Nu_O \sim Re_O^{0.5}$ at higher Reynolds numbers to $Nu_O \sim Re_O$ in free molecular flow. Equation (16) and (17) are shown in Figure 1 and 2 of Reference [34]. The heat transfer correlation is accurate to ± 7 percent, and the normalized recovery factor $\bar{\eta}_*$ is accurate to ± 10 percent for $M > 0.6$ [34]. Therefore, the reduced flow properties shall only be used in a qualitative manner.

The detailed expressions are:

$$\xi(Re_O, \infty) = Re_O^n [0.1400 + 0.2302 \left(\frac{Re_O^{0.7114}}{15.44 + Re_O^{0.7114}} \right)]$$

$$+ \left(\frac{0.01569}{0.3077 + \text{Re}_O^{0.7378}} \right) \left(\frac{15}{15 + \text{Re}_O^3} \right) \Big]$$

$$\psi(\text{Re}_O, M) = 1 + A(M) \left[1.834 - 1.634 \left(\frac{\text{Re}_O^{1.109}}{2.765 + \text{Re}_O^{0.109}} \right) \right]$$

$$\times \left[1 + \left(0.300 - \frac{0.0650}{M^{1.670}} \right) \left(\frac{\text{Re}_O}{4 + \text{Re}_O} \right) \right]$$

$$n = 1 - \frac{1}{2} \left(\frac{\text{Re}_O^{0.6713}}{2.571 + \text{Re}_O^{0.6713}} \right)$$

$$A(M) = \frac{0.6039}{M} + 0.5701 \left[\left(\frac{M^{1.222}}{1 + M^{1.222}} \right)^{1.569} - 1 \right]$$

$$\eta_c = 1 - 0.050 \left(\frac{M^{3.5}}{1.175 + M^{3.5}} \right)$$

$$(\eta_f - \eta_c) = 0.2167 \left(\frac{M^{2.80}}{0.8521 + M^{2.80}} \right)$$

$$\bar{\eta}_* = \left(\frac{\text{Kn}_\infty^{1.193}}{0.4930 + \text{Kn}_\infty^{1.193}} \right)$$

and

$$\text{Re}_O = \frac{\rho_\infty V_\infty d}{\mu_O} = \left(\frac{\gamma g}{R} \right)^{.5} \frac{d p_s M}{\mu_O (T_O)^{.5}} \left(1 + \frac{\gamma-1}{2} M^2 \right)^{.5}$$

$$Kn_{\infty} = (\lambda_{\infty}/d) = (\pi\lambda/2)^{1/2} (M/Re_{\infty})$$

Since p_s is measured, Equation (16) and Equation (17) can be solved for M and T_o by Newton-Raphson iteration scheme. This is discussed in Appendix C.

All computations of flow properties were made using $\gamma = 1.4$ and the power law for viscosity and thermal conductivity, or

$$\frac{\mu_o}{\mu} = \left(\frac{T_o}{T}\right)^{0.76}$$

$$\frac{k_o}{k} = \left(\frac{T_o}{T}\right)^{0.86}$$

It was found that for $M < 0.3$, there was a numerical convergence problem. This is probably due to the inaccuracy of Dewey's correlation formula in that very low Mach number range.

CHAPTER IV

FLOW UPSTREAM OF SEPARATION

1. SURFACE STATIC PRESSURE DISTRIBUTION

Surface pressure measurements upstream of the separation corner are presented in Figures 10, 11, and 12 for $M_\infty = 2.5, 3.5, 5.0$ and various Reynolds numbers*. The pressure distribution is the combined results of the viscous weak interaction and the upstream influence of the base pressure. The viscous interaction effect is pointed out by Baum [5] based on Hama's data [8]. In order to isolate the weak interaction effect, the surface pressure is normalized by p_1 which is the measured pressure at the orifice furthest (1.5 inch) upstream from the corner.

A significant fraction of the pressure drop occurring upstream of the corner can be seen. This indicates that the signal of lower base pressure is transmitted through the subsonic portion of the approaching boundary layer, and the expansion actually begins upstream of the corner, which, consequently introduces an appreciably normal pressure gradient. At the same free stream Mach number, the degree of upstream influence gets larger as the Reynolds number becomes lower. The length of upstream influence increases with increasing Mach number. These seem to imply that the

*from 0.2 to 2.0×10^6

$M_\infty = 2.5$
 $L = 4.0$ inches
 $H = 0.75$ inch

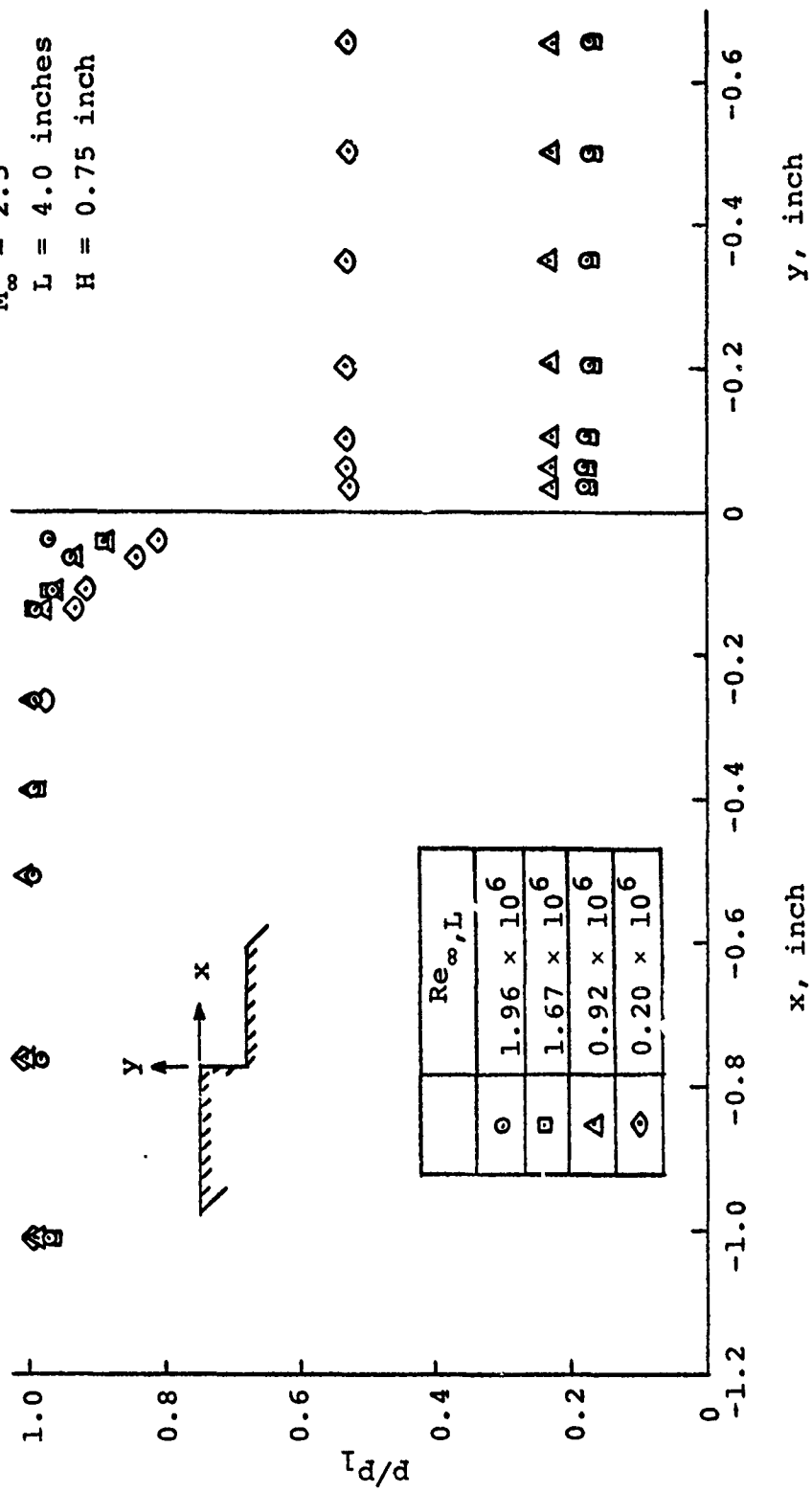


Figure 10. Surface Pressure Distributions at $M_\infty = 2.5$.

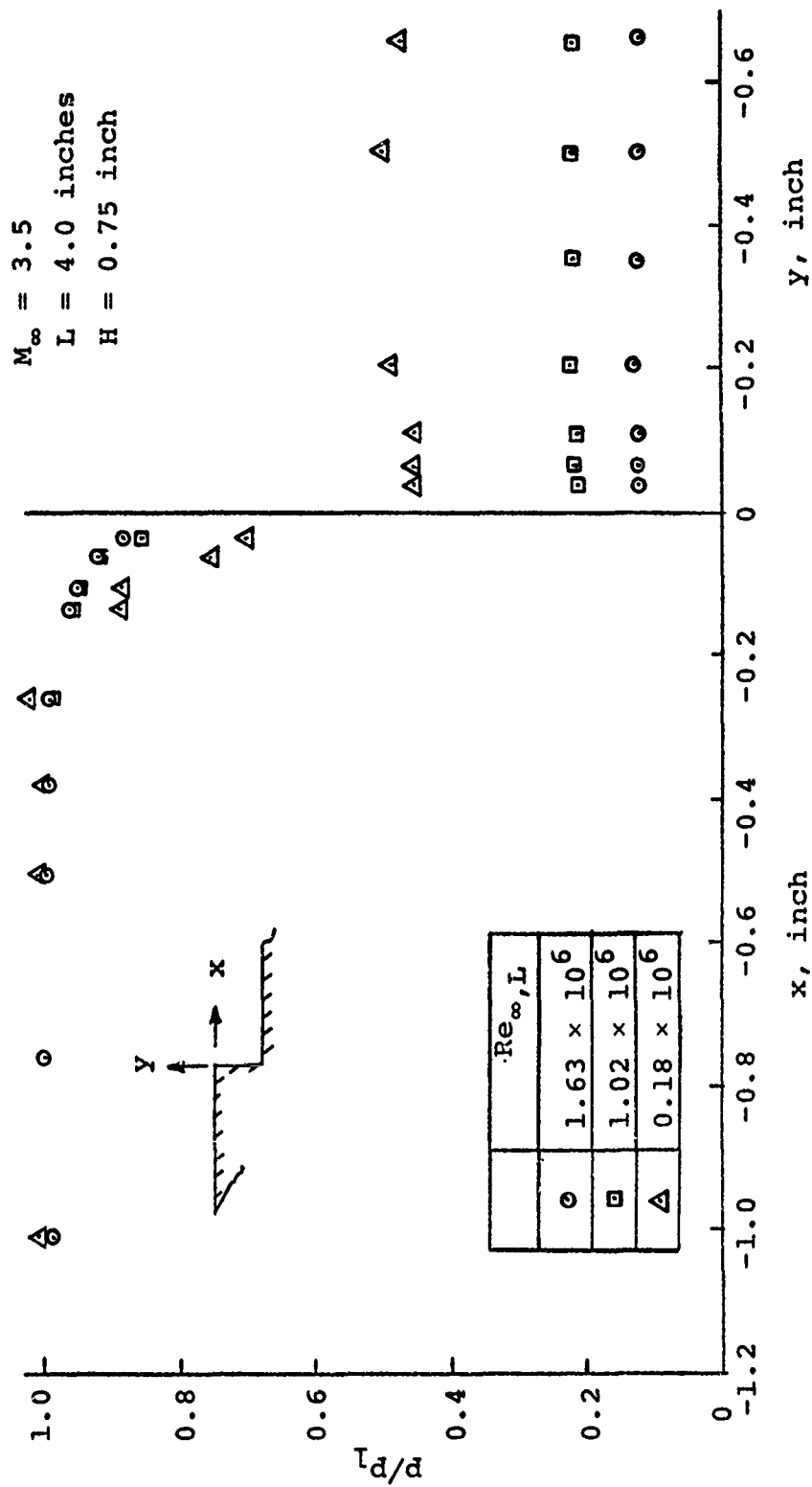


Figure 11. Surface Pressure Distributions at $M_\infty = 3.5$.

$M_\infty = 5.0$
 $L = 4.0$ inches
 $H = 0.75$ inch

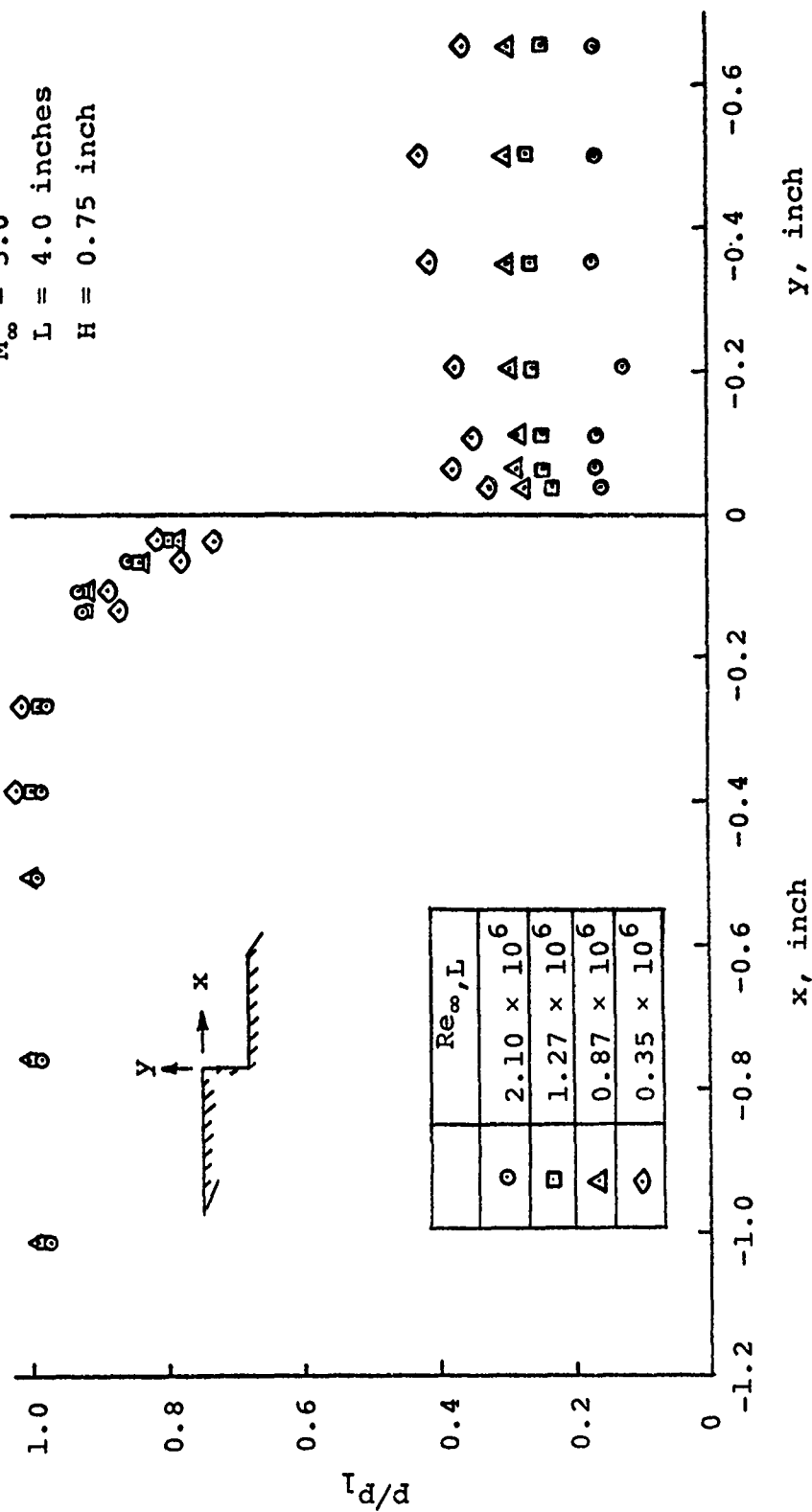


Figure 12. Surface Pressure Distributions at $M_\infty = 5.0$.

boundary layer thickness is a characteristic length in this region.

2. CORRELATION OF SURFACE PRESSURE

The surface pressures are correlated by the parameter x/δ , where δ is the boundary layer thickness at the separation corner computed as if there were no upstream influence [4].

$$\frac{\delta}{L} = [5.0 + 1.2 (\gamma-1) M_{\infty}^2] / \sqrt{Re_{\infty,L}} \quad (18)$$

The result of correlation for free stream Mach number from 2.5 to 5.0 and free stream Reynolds number per inch from 0.04×10^6 to 0.53×10^6 is shown in Figure 13. The correlation reveals that the upstream influence is a function of δ . The signal of the lower base pressure can be propagated upstream to a distance of about five times the thickness of the approaching boundary layer. It appears from this study that the step height has no effect on the upstream influence. The results of a 6° wedge [8] are also included in Figure 13.

Based on Figure 13, it is quite possible that, right at the corner, the pressure ratio might decrease to about 0.528. This suggests that a fluid element initially close to the surface (just outside of the

thin viscous layer) might accelerate to the sonic speed at the corner as speculated by some investigators [6]. This will be further discussed based on pitot-probe measurements in the next section.

3. ORDER OF MAGNITUDE ANALYSIS

A typical pitot pressure survey of the approaching boundary layer at $M_\infty = 5.0$ is presented in Figure 14. Because the height of the pitot-probe used in this study was relatively large compared to the measured boundary layer thickness, there was some probe interference. The interference has been shown to be severe at the outer edge of the boundary layer [38, 39, 40]. Due to the unknown normal pressure gradient, the reduction of the measured pitot pressures requires some approximation.

In order to estimate the relative importance of the terms in the equations of motion in a region of interest, one introduces the following nondimensional variables. They are all of order of unity.

$$\begin{aligned}\bar{x} &= x/X & , & & \bar{y} &= y/\delta \\ \bar{u} &= u/u_\infty & , & & \bar{\rho} &= \rho/\rho_\infty \\ \bar{p} &= p/\rho_\infty u_\infty^2 & , & & \bar{\mu} &= \mu/\mu_\infty\end{aligned}\tag{19}$$

Then, from the continuity equation of compressible flow, one knows that the nondimensional velocity \bar{v} has

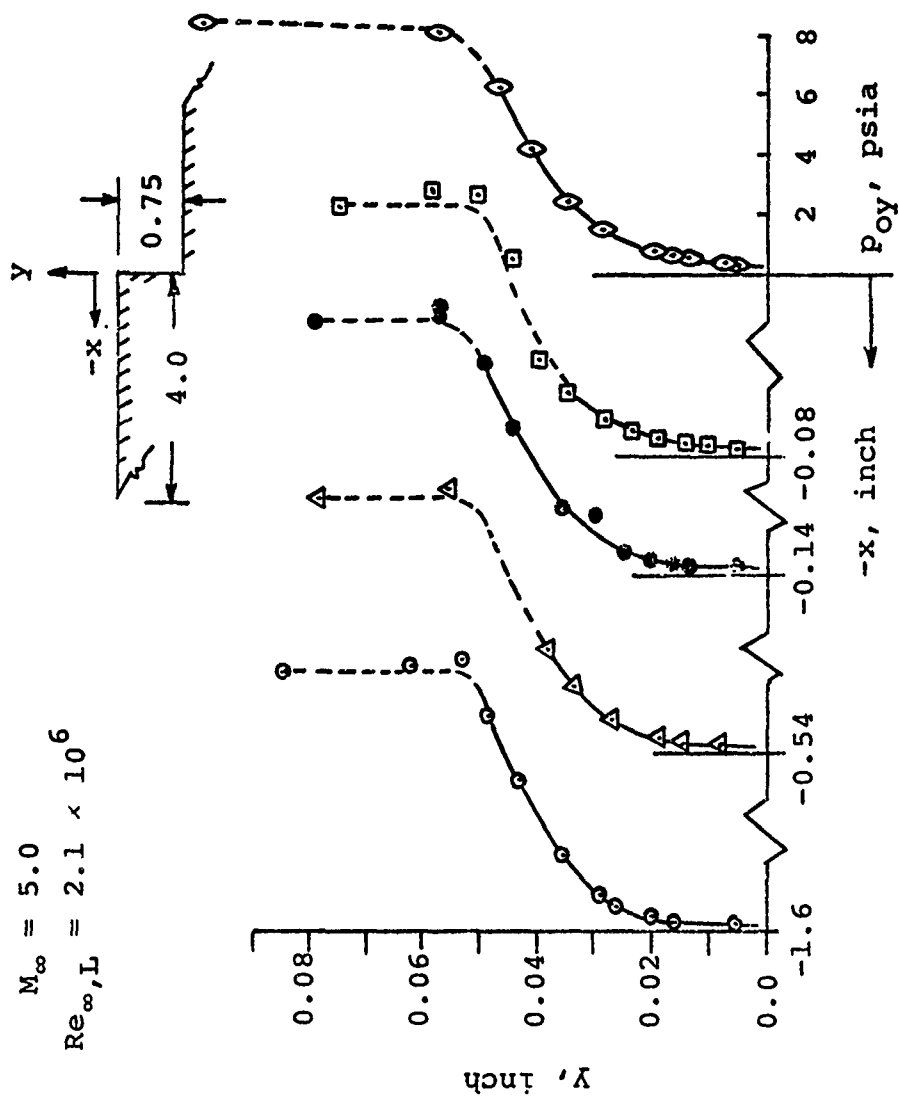


Figure 14. Typical Pitot Surveys of Approaching Boundary Layer.

to be defined as

$$\bar{v} = (v/u_{\infty}) (X/\delta) \quad (20)$$

With the nondimensional variables defined in Equations (19) and (20), the nondimensional form of the Navier-Stokes equations for the steady two-dimensional compressible flow are:

$$\begin{aligned} \bar{\rho} \bar{u} \frac{\partial \bar{u}}{\partial \bar{x}} + \bar{\rho} \bar{v} \frac{\partial \bar{u}}{\partial \bar{y}} = & - \frac{\partial \bar{p}}{\partial \bar{x}} + \frac{\mu_{\infty}}{\rho_{\infty} u_{\infty} X} \left(\frac{X}{\delta} \right)^2 \frac{\partial}{\partial \bar{y}} \left(\bar{\mu} \frac{\partial \bar{u}}{\partial \bar{y}} \right) \\ & + \frac{\mu_{\infty}}{\rho_{\infty} u_{\infty} X} \left[\bar{\mu} \frac{\partial^2 \bar{u}}{\partial \bar{x}^2} + \frac{\bar{\mu}}{3} \left(\frac{\partial^2 \bar{u}}{\partial \bar{x}^2} + \frac{\partial^2 \bar{v}}{\partial \bar{x} \partial \bar{y}} \right) \right. \\ & \left. - \frac{2}{3} \frac{\partial \bar{\mu}}{\partial \bar{x}} \left(\frac{\partial \bar{u}}{\partial \bar{x}} + \frac{\partial \bar{v}}{\partial \bar{y}} \right) + 2 \frac{\partial \bar{\mu}}{\partial \bar{x}} \frac{\partial \bar{u}}{\partial \bar{x}} + \bar{\mu} \frac{\partial \bar{\mu}}{\partial \bar{y}} \frac{\partial \bar{v}}{\partial \bar{x}} \right] \end{aligned} \quad (21)$$

$$\begin{aligned} \frac{\delta}{X} \left[\bar{\rho} \bar{u} \frac{\partial \bar{v}}{\partial \bar{x}} + \bar{\rho} \bar{v} \frac{\partial \bar{v}}{\partial \bar{y}} \right] = & - \frac{X}{\delta} \frac{\partial \bar{p}}{\partial \bar{y}} \\ & + \frac{\mu_{\infty}}{\rho_{\infty} u_{\infty} X} \left(\frac{X}{\delta} \right) \left[\bar{\mu} \frac{\partial^2 \bar{v}}{\partial \bar{y}^2} + \frac{\bar{\mu}}{3} \left(\frac{\partial^2 \bar{u}}{\partial \bar{x} \partial \bar{y}} + \frac{\partial^2 \bar{v}}{\partial \bar{y}^2} \right) \right. \\ & \left. - \frac{2}{3} \frac{\partial \bar{\mu}}{\partial \bar{y}} \left(\frac{\partial \bar{u}}{\partial \bar{x}} + \frac{\partial \bar{v}}{\partial \bar{y}} \right) + 2 \frac{\partial \bar{v}}{\partial \bar{y}} \frac{\partial \bar{\mu}}{\partial \bar{y}} + \frac{\partial \bar{u}}{\partial \bar{y}} \frac{\partial \bar{\mu}}{\partial \bar{x}} \right] \\ & + \frac{\mu_{\infty}}{\rho_{\infty} u_{\infty} X} \left(\frac{\delta}{X} \right) \left[\frac{\partial^2 \bar{u}}{\partial \bar{x}^2} + \frac{\partial \bar{v}}{\partial \bar{x}} \frac{\partial \bar{\mu}}{\partial \bar{x}} \right] \end{aligned} \quad (22)$$

If one is interested in the development of the boundary layer along a whole body, then X is the body length, $\delta/L \ll 1$; and Equations (21) and (22) can be approximated by:

$$\bar{\rho} \bar{u} \frac{\partial \bar{u}}{\partial \bar{x}} + \bar{\rho} \bar{v} \frac{\partial \bar{u}}{\partial \bar{y}} = - \frac{\partial \bar{p}}{\partial \bar{x}} + \frac{\mu_{\infty}}{\rho_{\infty} u_{\infty} L} \left(\frac{\delta^2}{L} \right) \frac{\partial}{\partial \bar{y}} \left(\bar{\mu} \frac{\partial \bar{u}}{\partial \bar{y}} \right) \quad (23)$$

$$\frac{\partial \bar{p}}{\partial \bar{y}} = 0 \left(\frac{\delta^2}{L} \right) \quad (24)$$

since for laminar boundary layer flow

$$\left(\frac{\delta^2}{L} \right) \sim \frac{1}{Re_{\infty, L}}$$

Equations (23) and (24) reduce to the boundary layer equations.

However, if one is interested in a region whose axial distance is comparable to the boundary layer thickness, then $X \approx \delta$, $\delta/X \approx 1$; and Equations (21) and (22) can be approximated by:

$$\bar{\rho} \bar{u} \frac{\partial \bar{u}}{\partial \bar{x}} + \bar{\rho} \bar{v} \frac{\partial \bar{u}}{\partial \bar{y}} = - \frac{\partial \bar{p}}{\partial \bar{x}} + \frac{\mu_{\infty}}{\rho_{\infty} u_{\infty} \delta} \text{ (viscous terms)} \quad (25)$$

$$\bar{\rho} \bar{u} \frac{\partial \bar{v}}{\partial \bar{x}} + \bar{\rho} \bar{v} \frac{\partial \bar{v}}{\partial \bar{y}} = - \frac{\partial \bar{p}}{\partial \bar{y}} + \frac{\mu_{\infty}}{\rho_{\infty} u_{\infty} \delta} \text{ (viscous terms)} \quad (26)$$

since for laminar flow

$$\frac{\mu_{\infty}}{\rho_{\infty} u_{\infty} \delta} \sim \frac{1}{(Re_{\infty, L})^{0.5}} \sim \frac{\delta}{L}$$

then Equations (25) and (26) become

$$\bar{\rho} \bar{u} \frac{\partial \bar{u}}{\partial \bar{x}} + \bar{\rho} \bar{v} \frac{\partial \bar{u}}{\partial \bar{y}} = - \frac{\partial \bar{p}}{\partial \bar{x}} + \frac{\delta}{L} \quad (\text{viscous terms}) \quad (27)$$

$$\bar{\rho} \bar{u} \frac{\partial \bar{v}}{\partial \bar{x}} + \bar{\rho} \bar{v} \frac{\partial \bar{v}}{\partial \bar{y}} = - \frac{\partial \bar{p}}{\partial \bar{y}} + \frac{\delta}{L} \quad (\text{viscous terms}) \quad (28)$$

Based on pitot measurements close to the corner, one finds that the static pressure reaches the free stream value at about 2δ in the y direction. This, and the fact that the boundary layer begins to accelerate 5δ ahead of the corner, suggests that Equations (27) and (28) are the approximate equations of motion in the region of upstream influence.

It follows from Equations (27) and (28) that the viscous forces on a fluid element are of the order δ/L smaller than the pressure and the inertial forces in the major portion of the expansion (except in the thin viscous layer adjacent to the wall where non-slip conditions must be satisfied). Also, the momentum equation in the y direction is as important as that in the x direction. Therefore, it will be a good approximation to treat the acceleration of the approaching boundary layer and the following rapid expansion downstream of the corner

isentropically. Since there is strong entropy gradient in the boundary layer before acceleration, the stagnation pressure is constant only along the streamline.

4. APPROACHING BOUNDARY LAYER ACCELERATION ESTIMATED BY STREAMTUBE APPROXIMATION

The measured pitot pressure profiles are analyzed based on the isentropic streamtube approximation, which assumes that total pressure is conserved along each streamtube, i.e.,

$$P_{ox}(ij) = P_{ox}(oj) \quad (29)$$

where i denotes the i^{th} station and j denotes the j^{th} streamtube. The notations are illustrated in Figure 15. $P_{ox}(oj)$ is the stagnation pressure of the j^{th} streamtube at the beginning of acceleration, which is computed from the measured pitot pressure under the boundary layer assumption.

The height of the j^{th} streamtube from the wall at i station is computed by

$$y(ij) = \sum_{j=0}^j \Delta(ij) \quad (30)$$

and $\Delta(ij)$ is related to $\Delta(oj)$ by the following one-dimensional isentropic streamtube-area relation [41].

$$y(ij) = \sum_{j=0}^j \Delta(ij)$$

$$P_{Ox}(oj) = P_{Ox}(ij) = P_{Ox}[y(ij)]$$

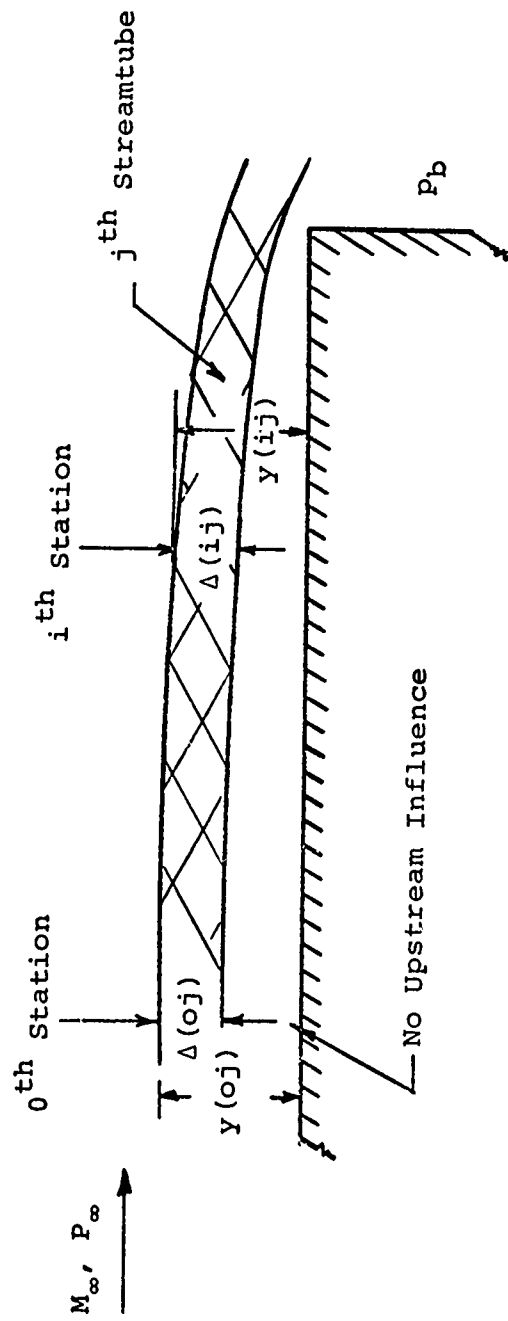


Figure 15. Isentropic Streamtube Approximation.

$$\frac{\Delta(ij)}{\Delta(oj)} = \frac{M(oj)}{M(ij)} \left[\frac{1 + \frac{\gamma-1}{2} M^2(ij)}{1 + \frac{\gamma-1}{2} M^2(oj)} \right]^{\frac{\gamma+1}{2(\gamma-1)}} \quad (31)$$

where $\Delta(oj)$ is the initial thickness of the j th streamtube.

The Mach number $M(ij)$ is related to the measured pitot pressure $p_{oy}(ij)$ by the normal shock equation [41].

$$\frac{p_{oy}(ij)}{p_{ox}(ij)} = \frac{\left[\frac{\frac{\gamma+1}{2} M^2(ij)}{1 + \frac{\gamma-1}{2} M^2(ij)} \right]^{\frac{\gamma}{\gamma-1}}}{\left[\frac{2\gamma}{\gamma+1} M^2(ij) - \frac{\gamma-1}{\gamma+1} \right]^{\frac{1}{\gamma-1}}} \quad (32)$$

Since the total pressure is constant along each streamtube, the loci of constant pitot measurements in the subsonic portion of the boundary layer are streamlines (the measured pitot pressure is equal to the stagnation pressure). The physical location of the first streamline $y(io)$ is identified somewhere in the subsonic portion of the boundary layer from the pitot pressure measurements.

Equations (29) through (32) can be combined to solve for $y(ij)$, $\Delta(ij)$ and $M(ij)$. The normal pressure gradient within the subsonic portion of the boundary layer was assumed to be negligibly small.

The Mach number profiles, streamlines and normal static pressure distribution at stations very close to the separation corner were calculated. The results are shown in Figure 16. Note that the major acceleration takes place at the lower half portion of the approaching boundary layer. The pressure gradient normal to the wall becomes significant in the supersonic portion of the boundary layer as the corner is approached. The static pressure variation in the supersonic portion of the boundary layer is found to be approximately linear.

The static pressure does not reach the free stream value at the outer edge of the approaching boundary layer, which indicates that the upstream influence was not confined to the boundary layer but appreciably alters the external flow as well.

It is interesting to observe that the streamwise and normal pressure gradients near the corner are about the same magnitudes. In other words, $(\partial p / \partial y) / (\partial p / \partial x)$ is approximately unity. It does not indicate, however, that the fluid element initially close to the surface will accelerate to the sonic speed at the corner, nor does it show any large curvature of the streamlines as predicted from the surface pressure measurements. This inconsistency may be attributed to the wall effects and the local probe disturbance. Also, very near the corner the upstream influence to the probe may be significant.

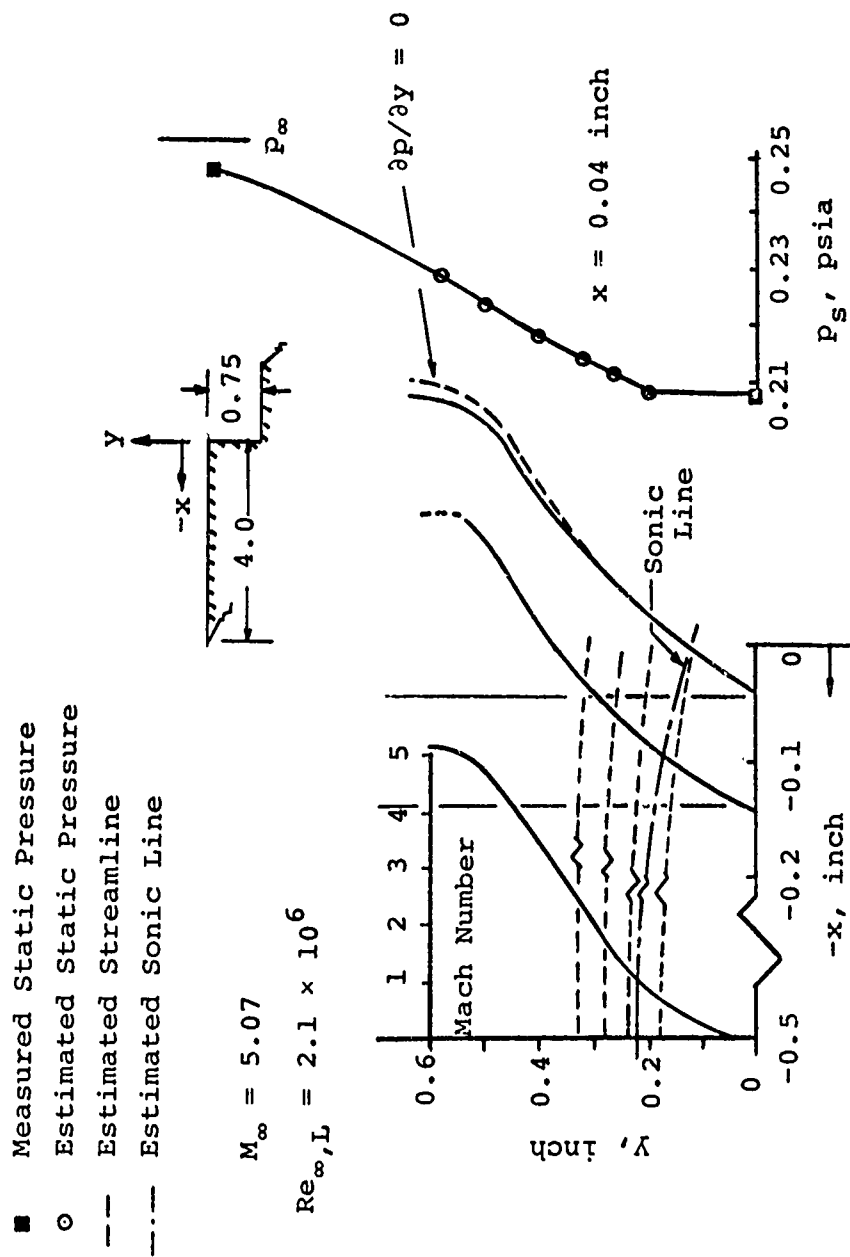


Figure 16. Estimated Mach Number and Static Pressure Distribution at $M_\infty = 5.07$.

The estimation (as shown in Figure 16) not only gave some indications about the flow field near the corner, but it also provides the initial conditions for the calculation by method of rotational characteristic which is discussed in the following chapter.

The difference in Mach number profile, reduced with and without static pressure gradient, is greater at the outer edge of the boundary layer. Also, without the static pressure correction, the reduced total pressure at the outer edge of the boundary layer is greater than the free stream total pressure. Similar estimation for $M_\infty = 3.5$, $Re_{\infty,L} = 1.0 \times 10^6$ is presented in Figure 17.

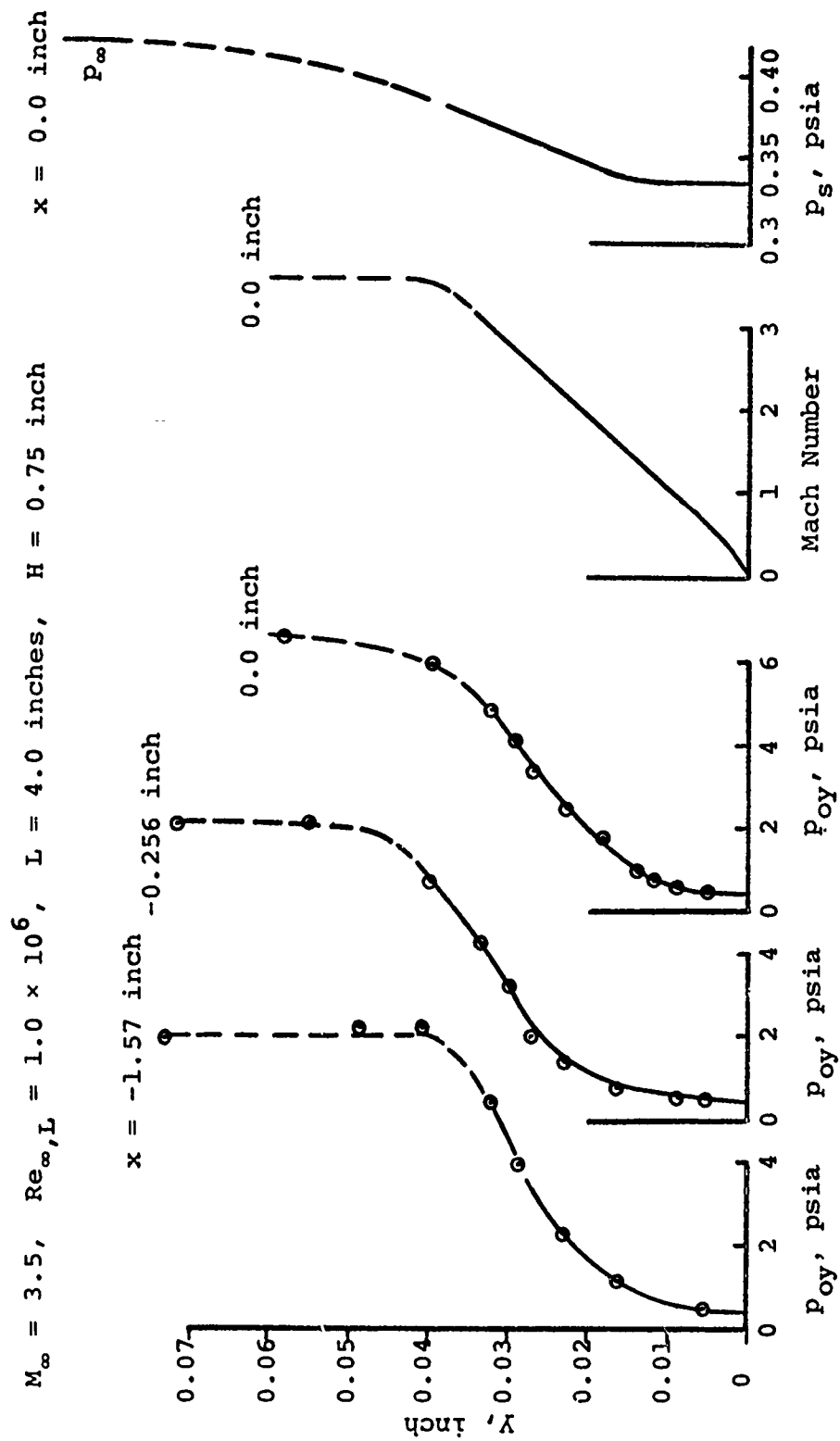


Figure 17. Estimated Mach Number and Static Pressure Distribution at $M_\infty = 3.5$.

CHAPTER V

FLOW DOWNSTREAM OF SEPARATION

1. PITOT PRESSURE MEASUREMENTS

The basic features of the entire wake of a back step are illustrated in Figure 18 by the pitot pressure survey for $M_\infty = 3.5$, $Re_{\infty,L} = 1.0 \times 10^6$, and $H = 0.75$ inch. The lip shock, wake shock and slip line can be clearly seen, and, their locations agree very well with the shadow-graph picture.

The pitot profiles in the lower edge of the free shear layer and recirculating region are shown in Figure 19. Note, the existence of the low pressure which dies away downstream along a line which is suspected to be the dividing streamline from hot-wire resistance measurements.* This may be the result of viscous effect on the pitot probe at very low Reynolds number; and it is not likely that this low pressure is due to the probe interference or the difference in flow direction with respect to the probe.

The pitot pressure distributions in the immediate neighborhood of the separation corner are presented in Figure 20, where the lip shock and the initial development of the free shear layer are evident. Since the

*This point is discussed further in Chapter IX.

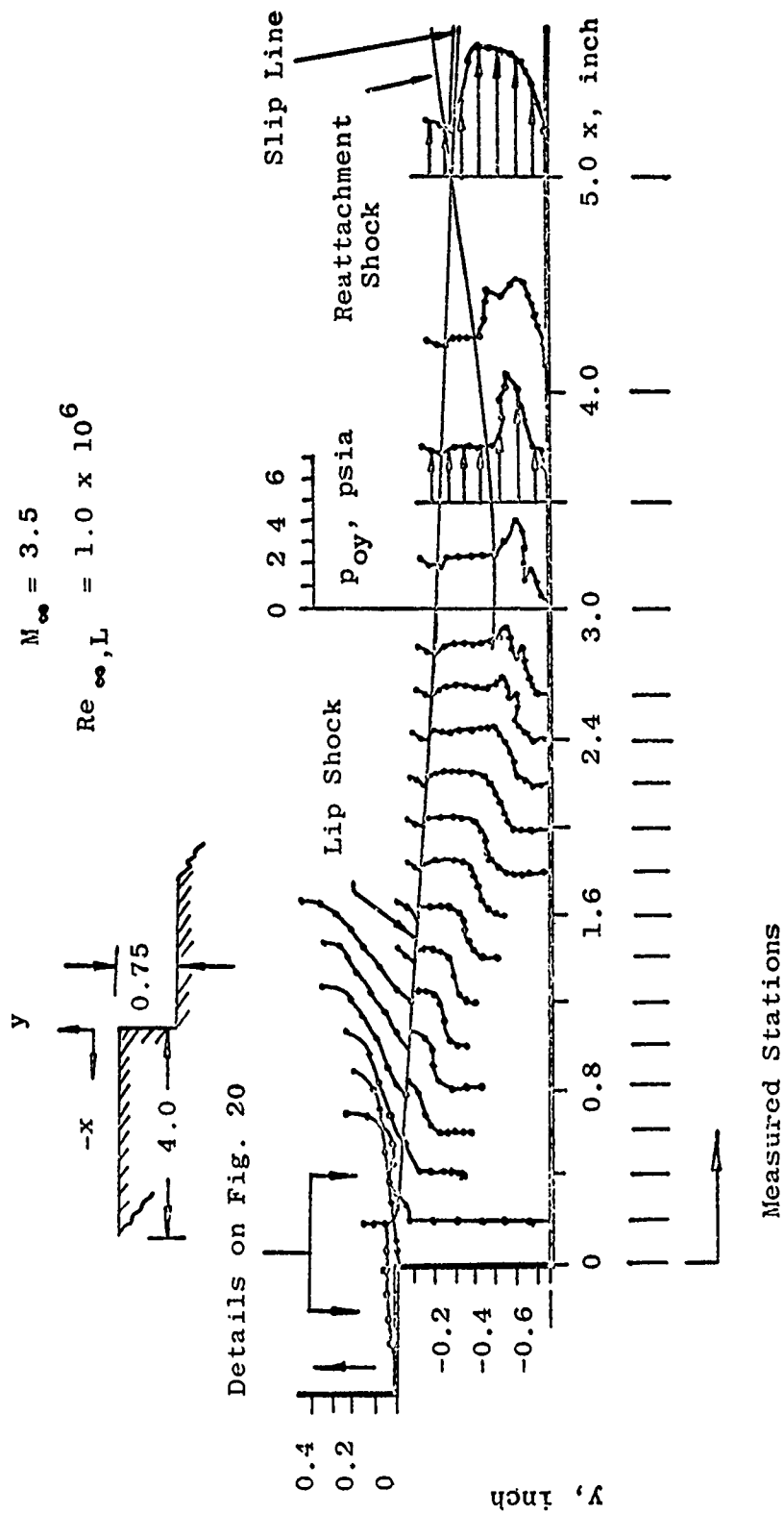


Figure 18. Typical Pitot Measurements in the Wake of a Backstep at $M_\infty = 3.5$

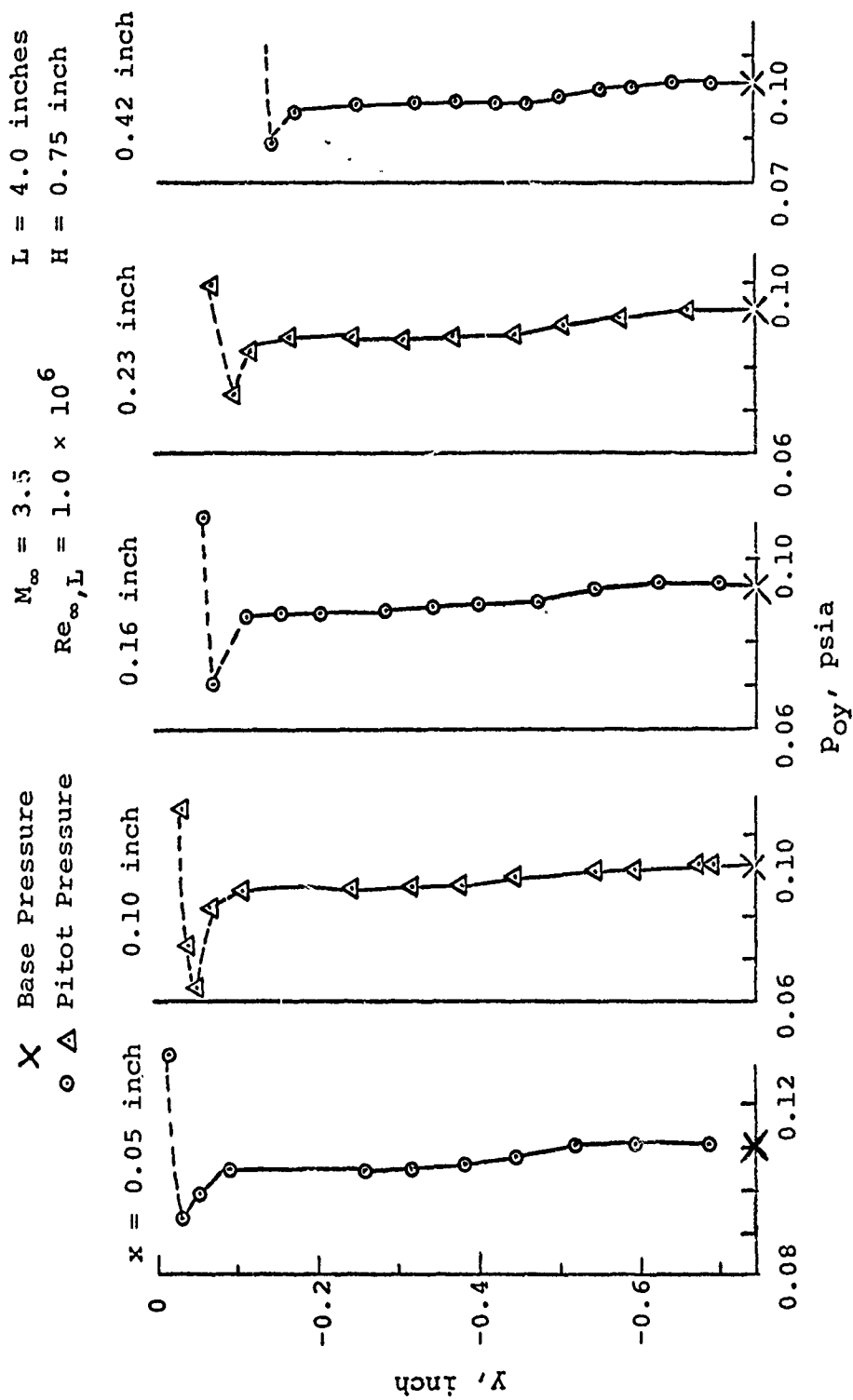


Figure 19. Pitot Pressure Profiles in and above Recirculating Region.

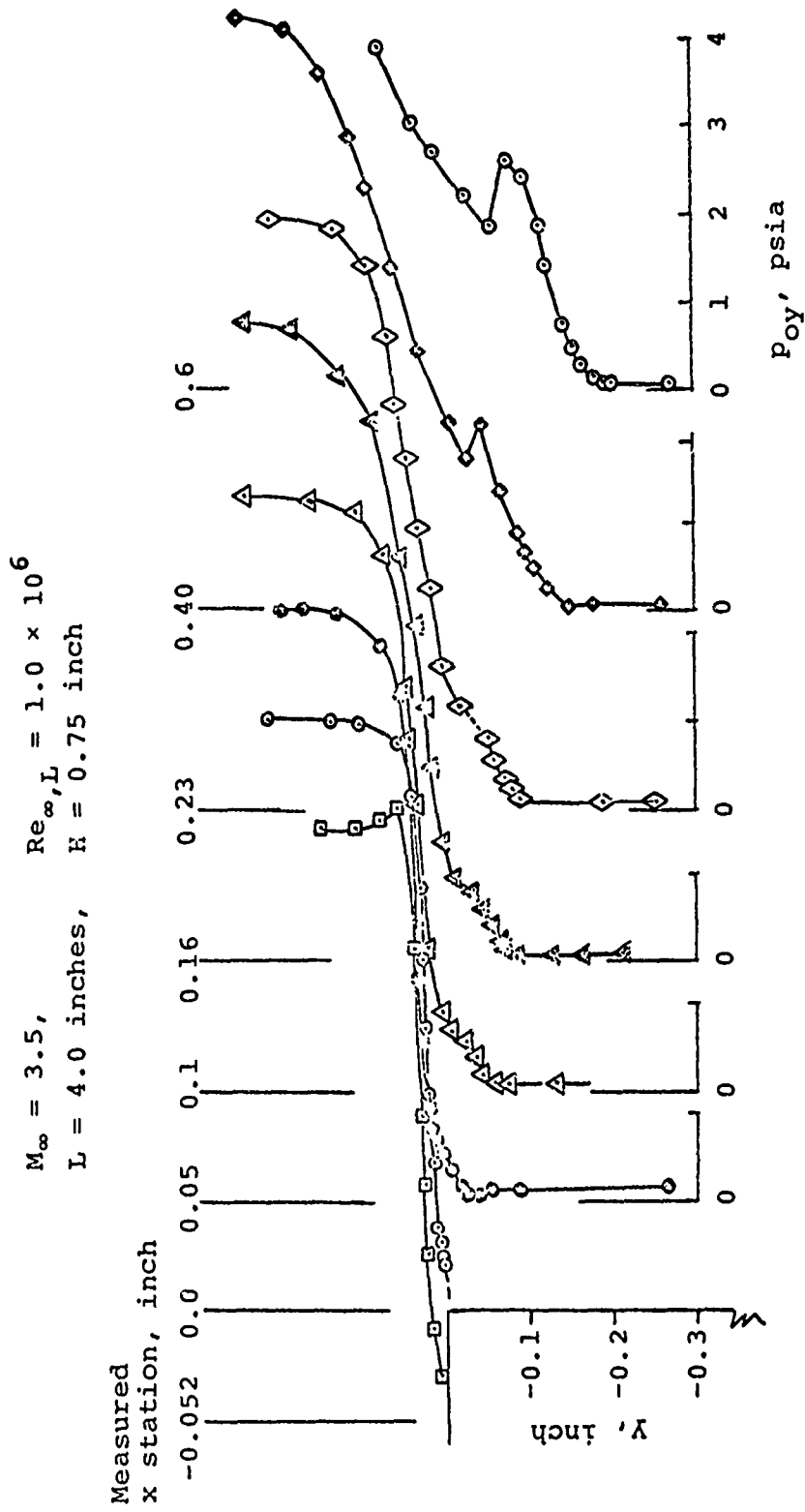


Figure 20. Pitot Pressure Profiles around Separation Corner.

stagnation pressure is relatively lower in the shear layer expanded from the lower portion of the boundary layer at the corner, the measured pitot pressure variation across the lip shock will be very small if the lip shock originates at the corner and passes through this region. Therefore, it is rather difficult to detect the beginning of the lip shock by pitot pressure surveys. A very dense pitot pressure measurement about one boundary layer thickness downstream of the corner appears to support this reasoning (as shown in Figure 21).

Since there are entropy gradients and streamwise and lateral pressure gradients in the expanding boundary layer, the pitot measurement in this region does not provide sufficient information for quantitative analysis. To supplement the pitot measurement, hot-wire measurements were attempted in this region. Unfortunately, in the regions of higher velocity near the corner and at reattachment, severe wire breakage was encountered. For this reason, no hot wire results were obtained in these regions, and only the cavity flow region was explored in this way. These results are discussed in Chapter VIII. However, comparisons of the measured pitot profiles with the results of theoretical calculations may provide some valuable information.

2. COMPARISONS WITH RESULTS OF PRANDTL-MEYER EXPANSION

The pitot pressure measurements have been compared with calculations from the Prandtl-Meyer equation for the

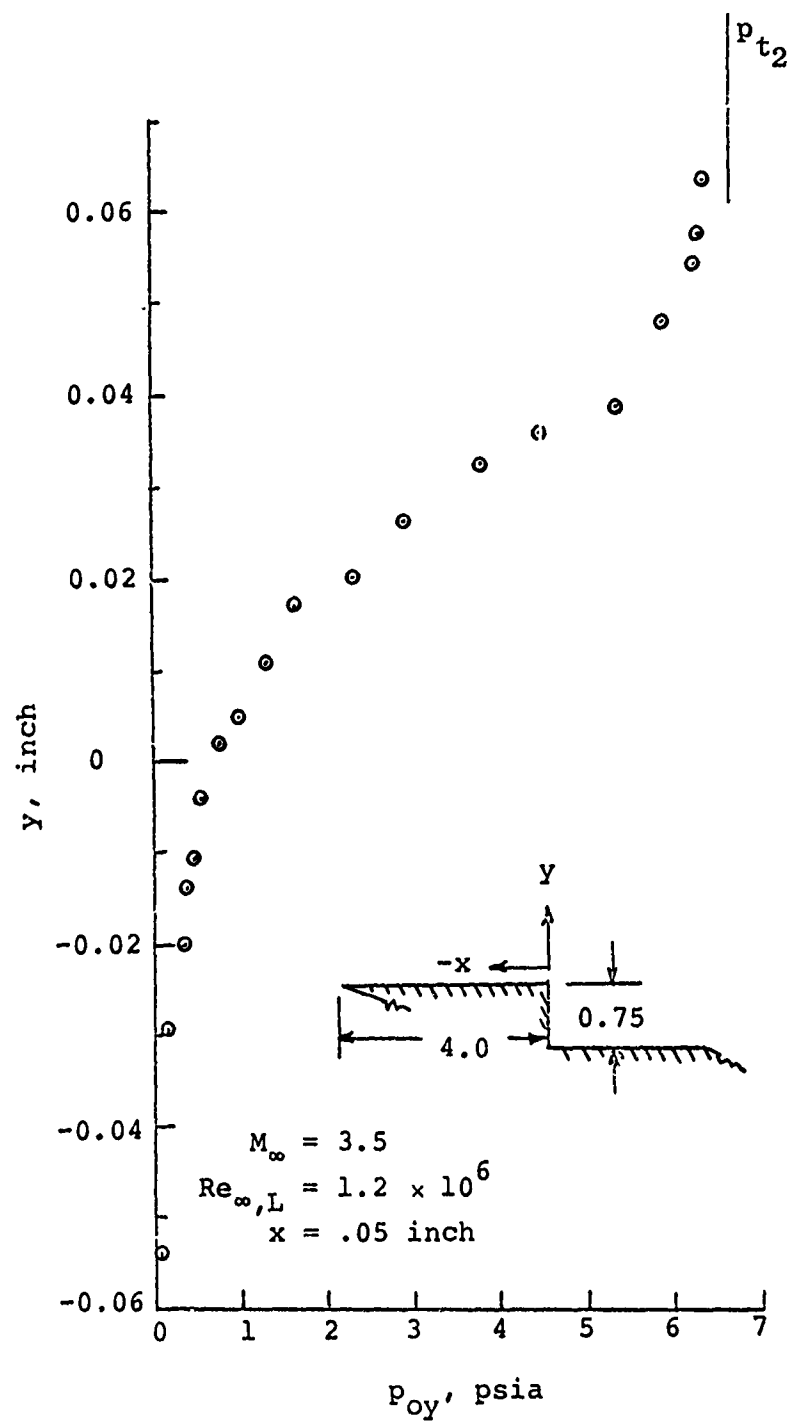


Figure 21. Pitot Pressure Profile Immediately Downstream of Separation.

following cases:

M_∞	$Re_{\infty,L}$
2.5	1.06×10^6
3.5	1.06×10^6
5.07	1.9×10^6

Since the Prandtl-Meyer theory is restricted to irrotational supersonic flow, it is expected that the existence of the boundary-layer will cause departures from the simple theory. The comparisons are shown in Figs. 22, 23, 24, respectively.

Scherberg and Smith [18, 25] and Hama [8] observed the phenomenon of an upstream influence of the lower base pressure on the approaching boundary-layer before the expansion corner. This point has been confirmed by this study, which reports in greater detail the pressure measurements in this region. A correlation of the surface pressure distribution upstream of the expansion corner has been discussed in the previous chapter. In addition, the over-expansion of the external inviscid stream ahead of the lip shock has been clearly demonstrated.

The lip shock is embedded in the expanded boundary-layer close to the corner and penetrates into the region of vanishing vorticity. The pitot pressures at the end of the expansion do not achieve the values predicted by the Prandtl-Meyer theory, but rather approach it after about 10 to 15 boundary-layer thickness downstream. Also beyond this station (see Figs. 22-24) there is a region of nearly

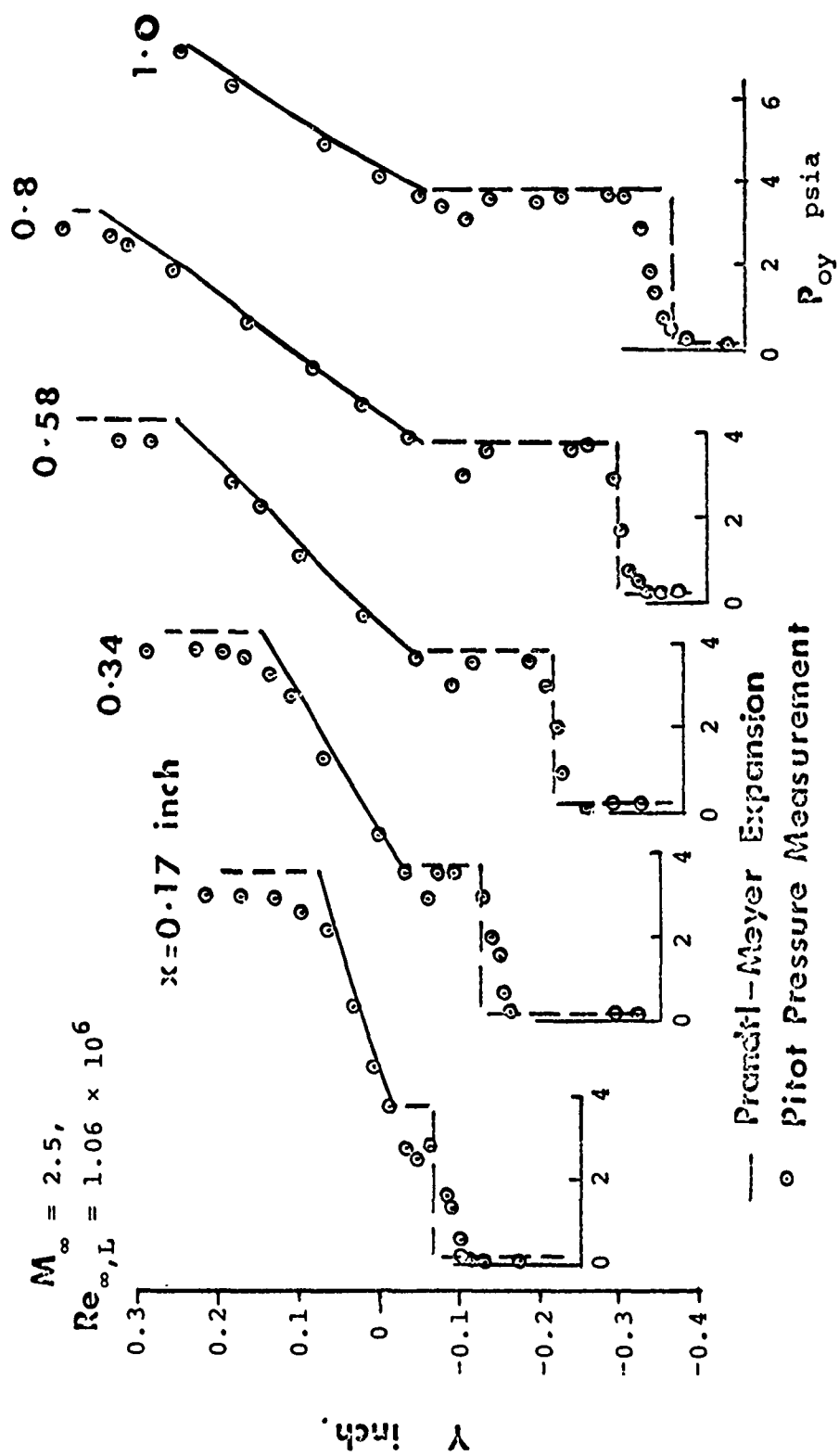


Figure 22. Comparison of Measured Pitot Profiles with Prandtl-Meyer Expansion at $M_\infty = 2.5$.

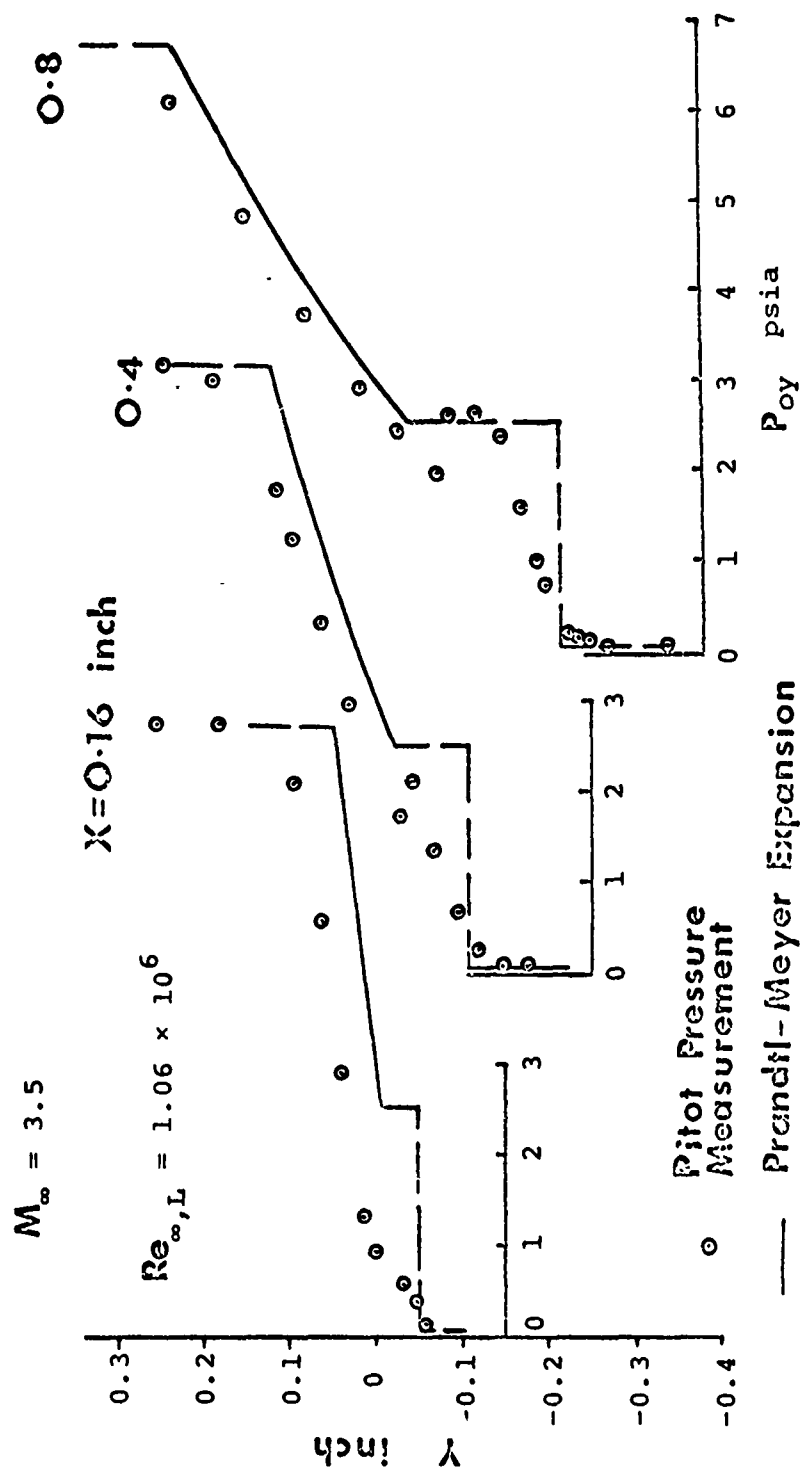


Fig. 23. Comparison with Prandtl-Meyer Expansion at $M_\infty = 3.5$.

$$M_{\infty} = 5.07,$$

$$Re_{\infty,L} = 1.9 \times 10^6$$

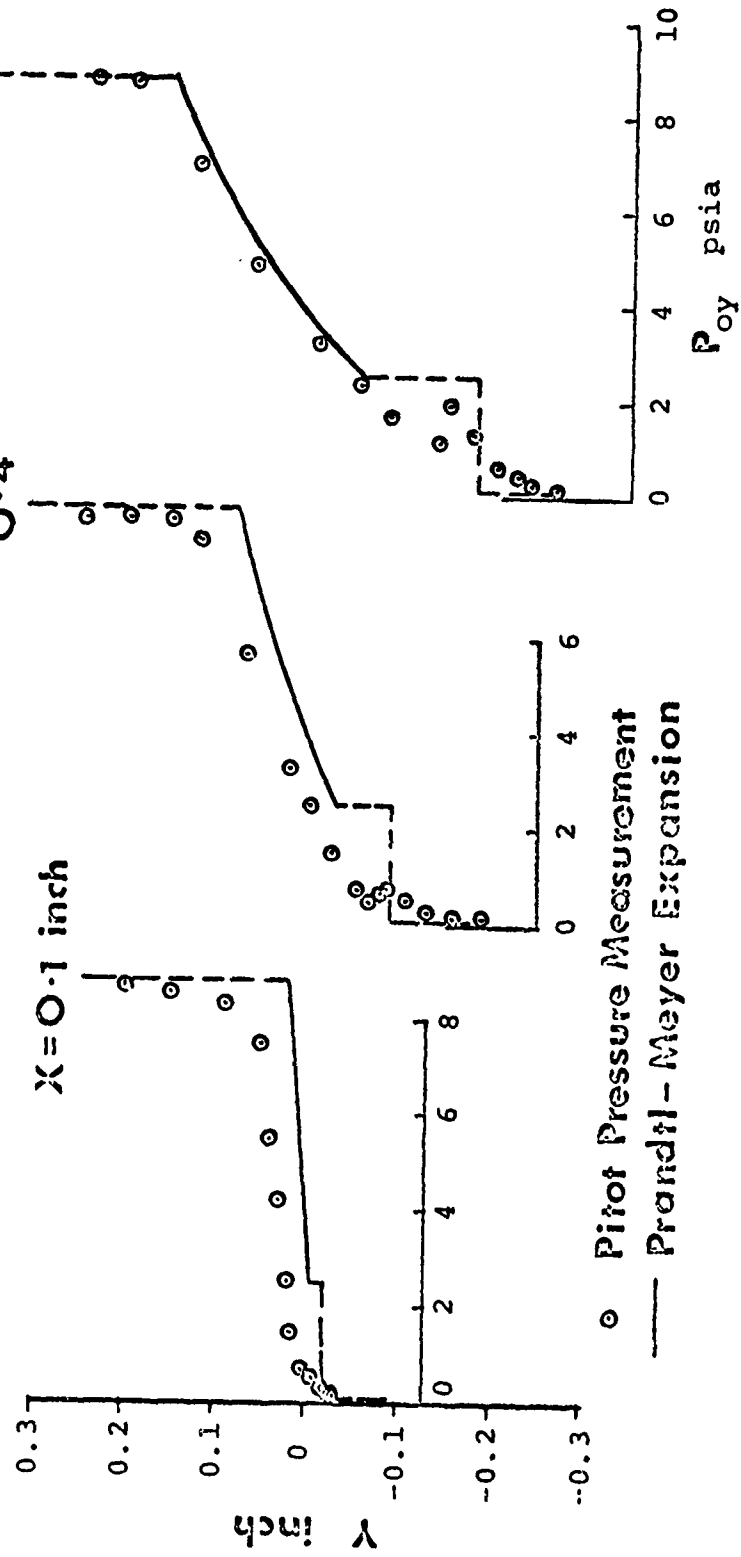


Fig. 24. Comparison with Prandtl-Meyer Expansion at $M_{\infty} = 5.07$.

uniform inviscid flow immediately downstream of the lip shock as indicated by the constant pitot pressures, which are nearly equal to the Prandtl-Meyer value. Scherberg and Smith [18] have pointed out in their paper that a constant pitot pressure reading does not necessarily indicate a uniform flow. Thus, they indicate that a sensibly constant total head reading ahead of an oblique shock can admit changes in the component velocity and static pressures such that the shock strength need not be constant. Therefore, a careful check was made by examining a series of shadow graphs with Hama's method. Within the accuracy of Hama's method, the Mach number behind the lip shock is found to be very nearly a constant value at different stations for a given free stream Mach number and Reynolds number (but the flow direction need not be constant [18]). This is more noticable for the lower free stream Mach number cases than for the higher free stream Mach number case (such as $M_\infty = 5.0$). Since the static pressure in this region is very close to the base pressure, it is clear that the external inviscid flow, upstream of the lip shock, overexpands to a pressure lower than the base pressure. Except close to the corner, the lip shock is at a considerable distance above the outer edge of the free shear layer.

It is obvious and expected that the Prandtl-Meyer theory fails to describe the flow field properly in such cases because of the boundary-layer shed from the body

surface. To accurately describe the flow field, the incoming boundary-layer cannot be neglected in the expansion-separation process (more examples will be given later). Furthermore, a similar phenomenon, i.e., a dip in the surface pressure before a sharp corner in a high subsonic flow was reported by Rubin [43].

The expansion of the supersonic boundary-layer around a separation corner has been treated with inviscid rotational theory; and the cause of lip shock formation was described as the relatively slow coalescence of the reflected wavelets [42]. It is of interest to compare the pitot measurements with the results of an inviscid rotational method of characteristics calculation; and this motivated the following investigation.

3. COMPARISONS WITH RESULTS OF ROTATIONAL CHARACTERISTICS CALCULATION

The pitot pressures computed by the method of rotational characteristics were provided by Matz [44] and are shown in Figs. 25 and 26 for $M_\infty = 3.5$ and $M_\infty = 5.07$ respectively. The initial conditions for the computation at the separation corner were estimated [26, 45] based on the measurement of the approaching boundary-layer before the corner. The supersonic portion of the boundary-layer at the corner was expanded to the base pressure (either a measured value or an estimated one), while the expansion of the inner boundary-layer at subsonic speed is neglected. The base pressure has been studied in detail, as outlined in Chapter VI, and

permits us to estimate the base pressure fairly accurately.

Very good agreement was found in the expanding boundary layer^{*} for both cases. As shown in Fig. 25, the pitot pressure profiles, the computed lip shock positions and the pitot pressure changes across the lip shock agree remarkably well with the measurements. This appears to support the contention that the formation of the lip shock is an inviscid rotational field phenomena-as originally proposed by Charwat and Yakura [24] and investigated by Weinbaum [42]. The effect of viscosity appears to be negligibly small compared to the change in pressure during the rapid expansion of the supersonic boundary-layer downstream of a separation corner.

Typical profiles of Mach number, static, total and pitot pressures obtained from the rotational characteristic calculations for two stations are shown in Fig. 27 for $M_\infty = 3.5$, $Re_{\infty,L} = 1.0 \times 10^6$ and $H = 0.75$ inch. The reduced Mach number from hot-wire measurements are also included for comparison. Note the lower static pressures and the corresponding overexpansion (compared to the Prandtl-Meyer expansion to the same base pressure) just before the lip shock. At $x = 0.8$ inch (roughly a step-height distance downstream of the corner), the higher total pressure at the lip shock makes the jump in pitot pressure across the lip shock larger and much more observable than that at $x = 0.4$ inch station; even though the Mach numbers and static pressures before and after the lip shock are about the same for both stations.

*It is defined herein that the "shear-layer" is the "expanded boundary layer" downstream of the corner.

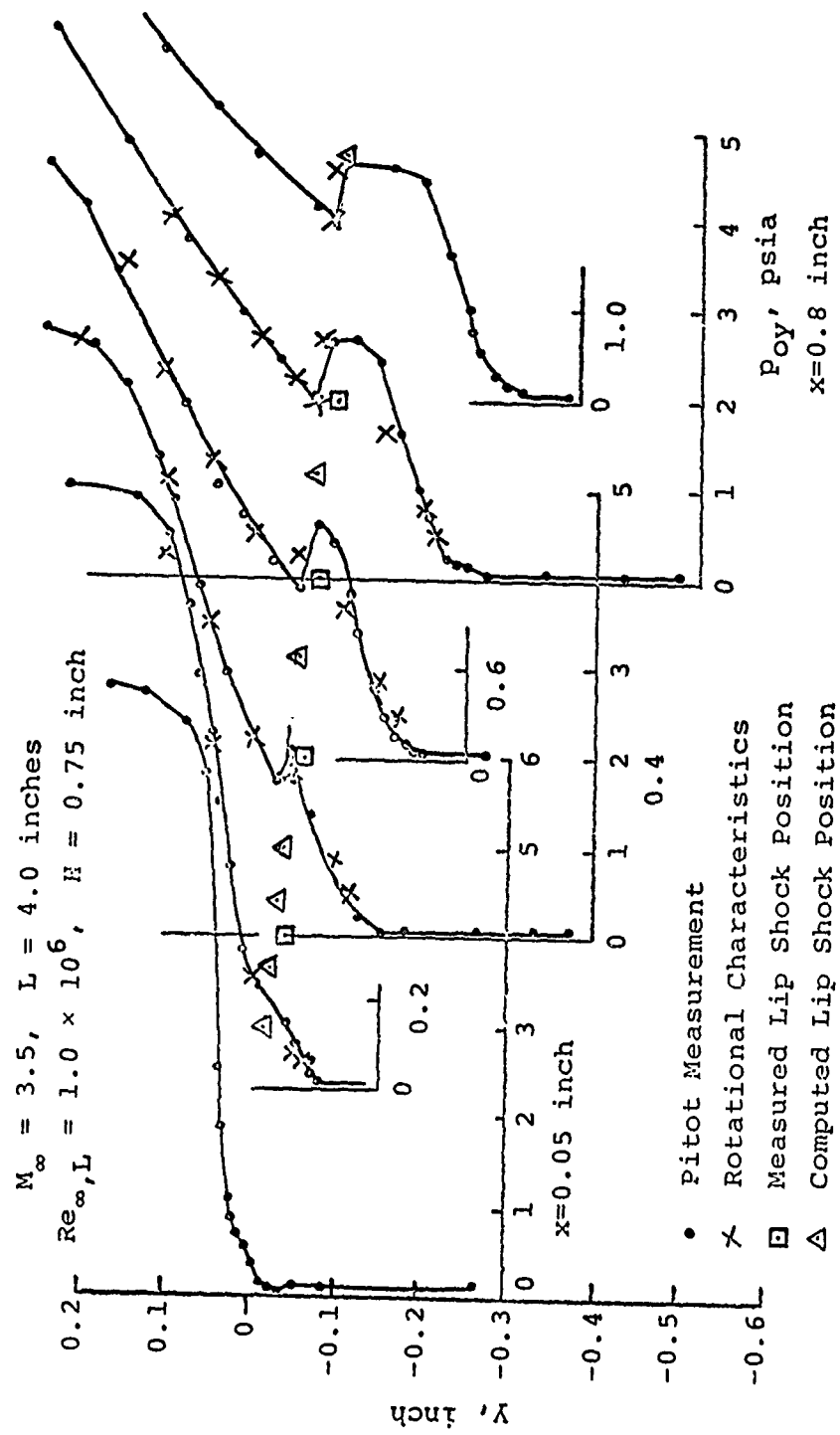


Fig. 25. Comparison of Measured and Computed Pitot Pressures at $M_\infty = 3.5$.

$M_\infty = 5.07$
 $Re_{\infty, L} = 1.9 \times 10^6$
 $L = 4.0$ inches
 $H = 0.75$ inch

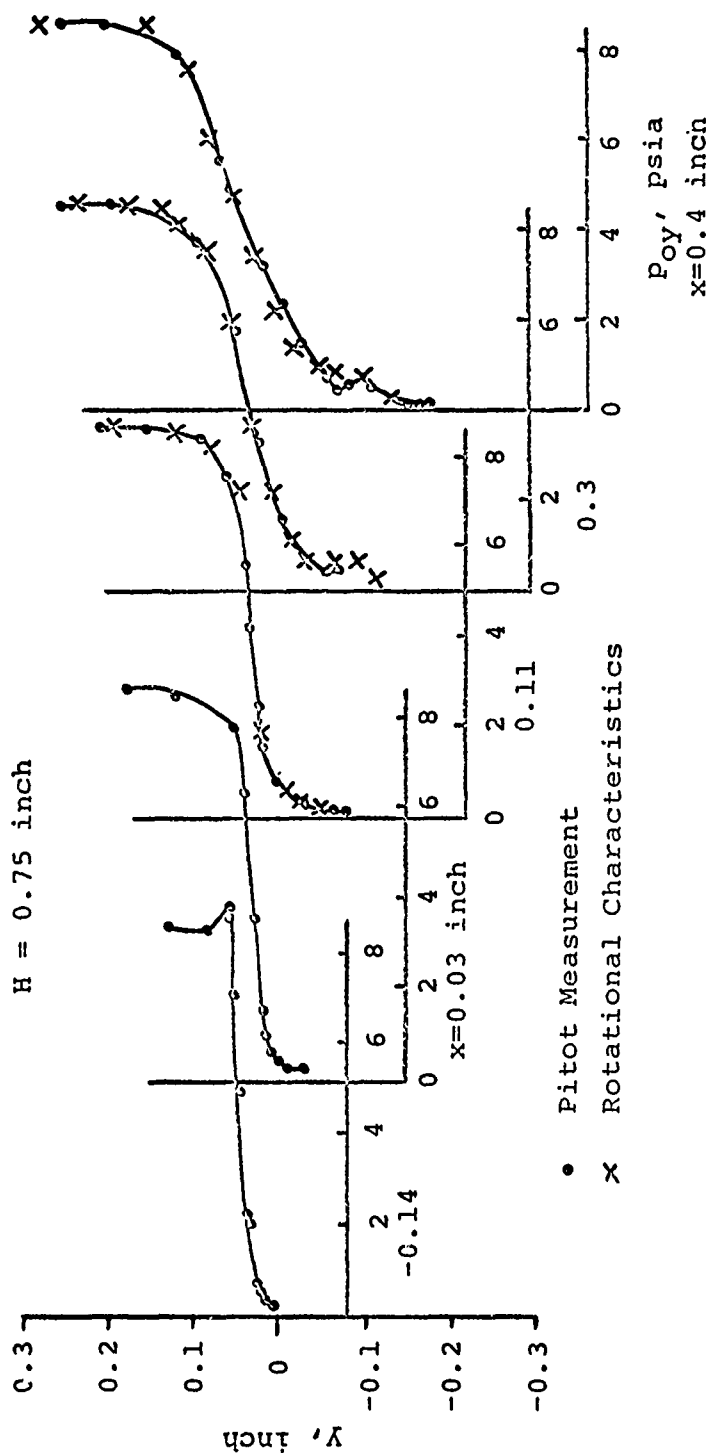


Fig. 26. Comparison of Measured and Computed Pitot Pressures at $M_\infty = 5.07$.

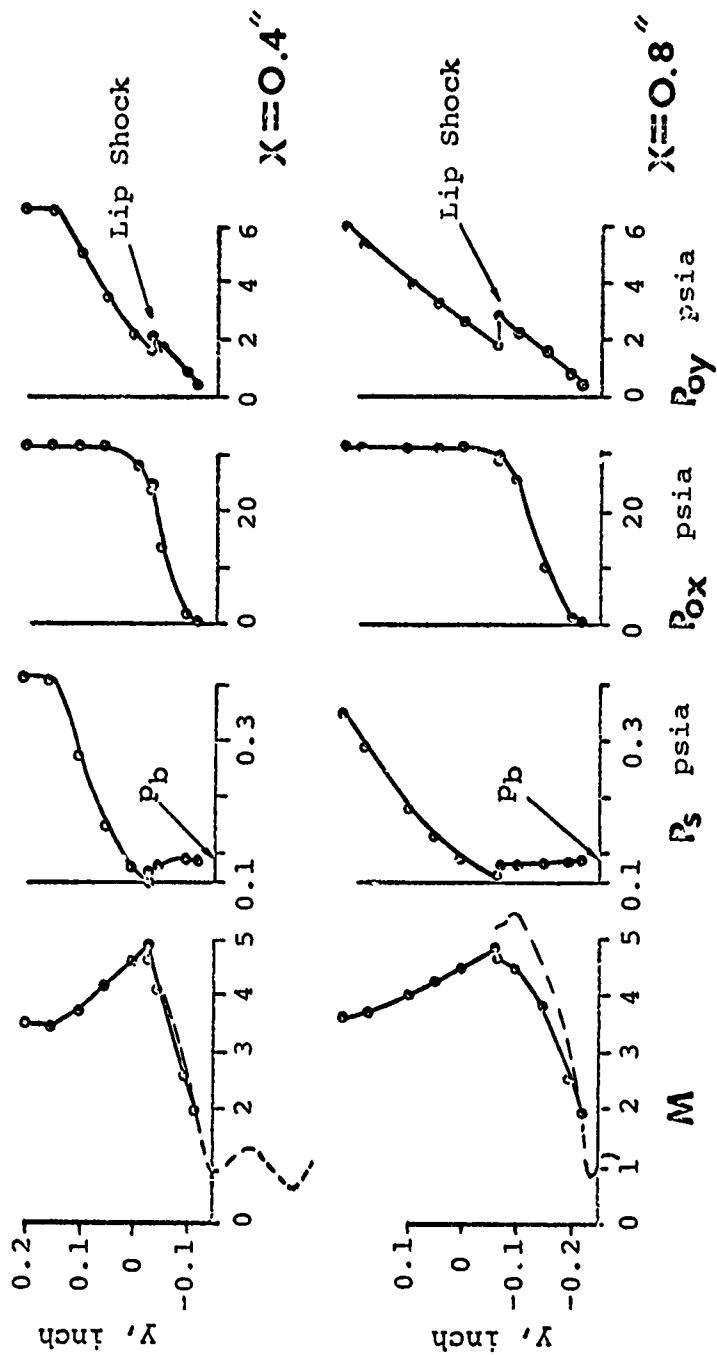


Fig. 27. Typical Results of Inviscid Rotational Characteristics.

The calculated pitot pressure normalized with the total pressure P_{ox}/P_t , and the Mach number immediately upstream (denoted by sub x) of the lip shock, M_x , are shown in Fig. 28 and indicate that within a distance of one step height, the lip shock is embedded in the vorticity layer originated from the expanded boundary-layer, and that the Mach number variation along the lip shock is small. The static pressure jump P_{sy}/P_{sx} , across the lip shock is also shown (subscript y indicates conditions downstream of the shock).

4. COMPARISON OF MEASURED PITOT PROFILES AT DIFFERENT FLOW CONDITIONS

The pitot pressure measurements at $M_\infty = 3.5$ and $Re_{\infty,L} = 1.0 \times 10^6$ and 1.72×10^6 are shown in Fig. 29, where the boundary-layers are laminar before separation in both cases. The pitot pressure is again normalized by its corresponding free stream total pressure. The flows expanding from the external inviscid streams under these two conditions are very nearly the same (see $x = 0.1$ inch station in Fig. 29) and they approach asymptotically to the flow field predicted by the Prandtl-Meyer theory. However, the flow turns through an angle that is consistent with its corresponding base pressure, the direction and profile of the free shear layers are very different downstream. As a reference and a comparison, the value calculated by Prandtl-Meyer expansion to the base pressure corresponding to that of $Re_{\infty,L} = 1.0 \times 10^6$ is included in Fig. 29.

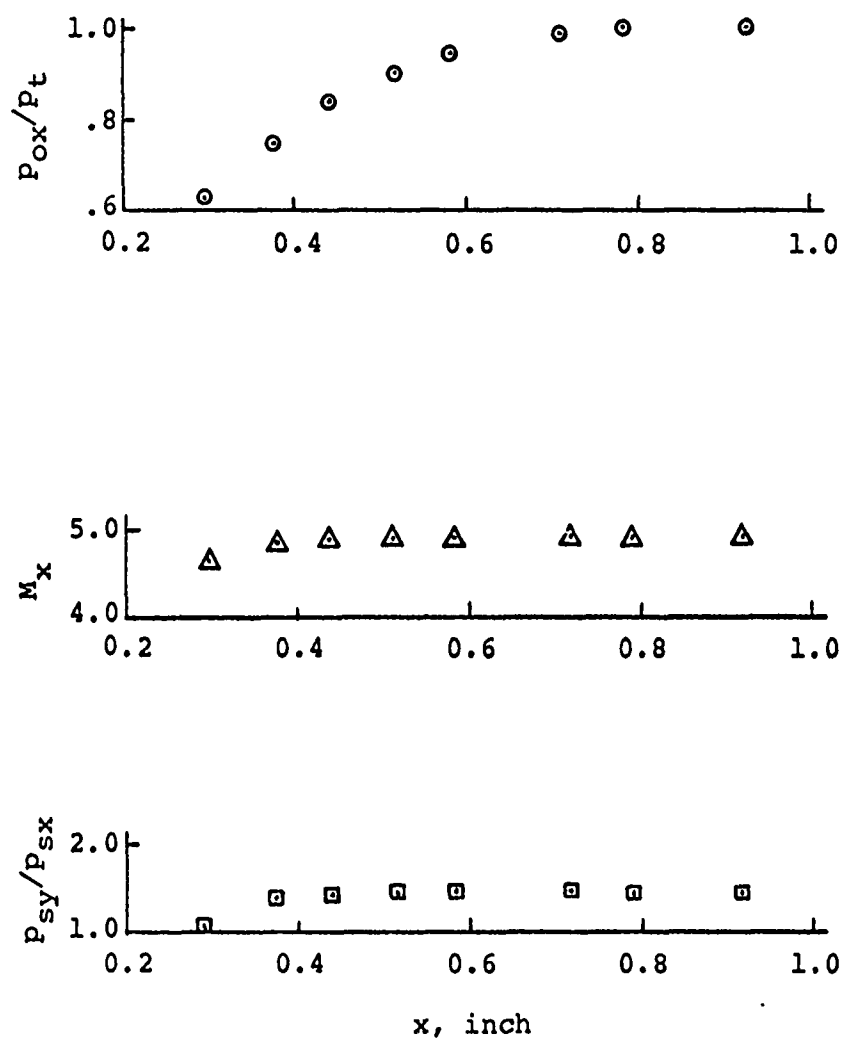


Fig. 28. Calculated Flow Properties along Lip Shock By Inviscid Rotational Characteristics.

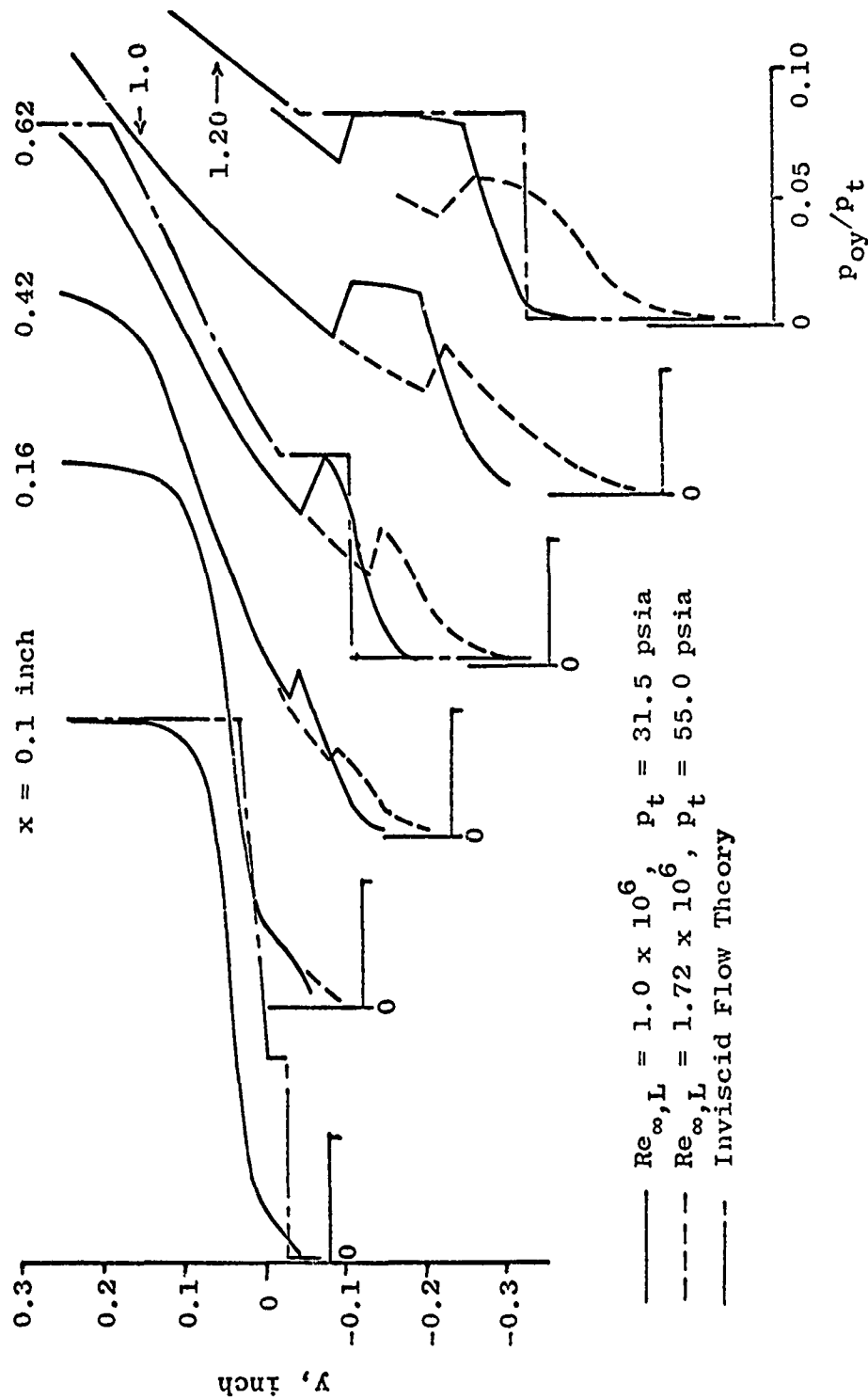


Fig. 29. Comparisons of Pitot Pressure Profiles for Different Reynolds Numbers and Inviscid Flow Theory at $M_\infty = 3.5$.

Fig. 30 shows the measurements for the $M_\infty = 2.5$, $Re_{\infty,L} = 1.0 \times 10^6$ and 1.82×10^6 flows. The considerable deviation in the expanding inviscid streams are probably due to the fact that for $Re_{\infty,L} = 1.82 \times 10^6$, the boundary-layer is transitional near the corner, and the boundary layer thickness increases as the Reynolds number increases. For a given free stream Mach number, the lip shock is directed downward at the high Reynolds number but turns upward and decreases in strength as the Reynolds number decreases. The reduced Mach number profiles, corresponding to the flow conditions of Fig. 30, is shown in Fig. 31. The calculation was based upon the assumptions that: (i) above the expanded boundary-layer the total pressure is equal to the free stream total pressure, (ii) underneath the lip shock the static pressure is equal to the base pressure.

It is quite evident from these observations that the post-expansion flow field is strongly dependent upon the nature of approaching boundary-layer at the corner and upon the base pressure, and, both are a function of $Re_{\infty,L}$ and other factors.

5. ON FREE STREAM MACH NUMBER EFFECT

The measured pitot pressure profiles, one inch downstream of the step, are shown in Fig. 32 for $Re_{\infty,L} = 1.0 \times 10^6$ and free stream Mach number of 2.5, 3.5 and 5.0 respectively. The measurements are normalized by the free stream stagnation pressure. These profiles are presented in different scales. The upstream influence in the outer inviscid expansion and the departure of the separated profiles from the Prandtl-Meyer

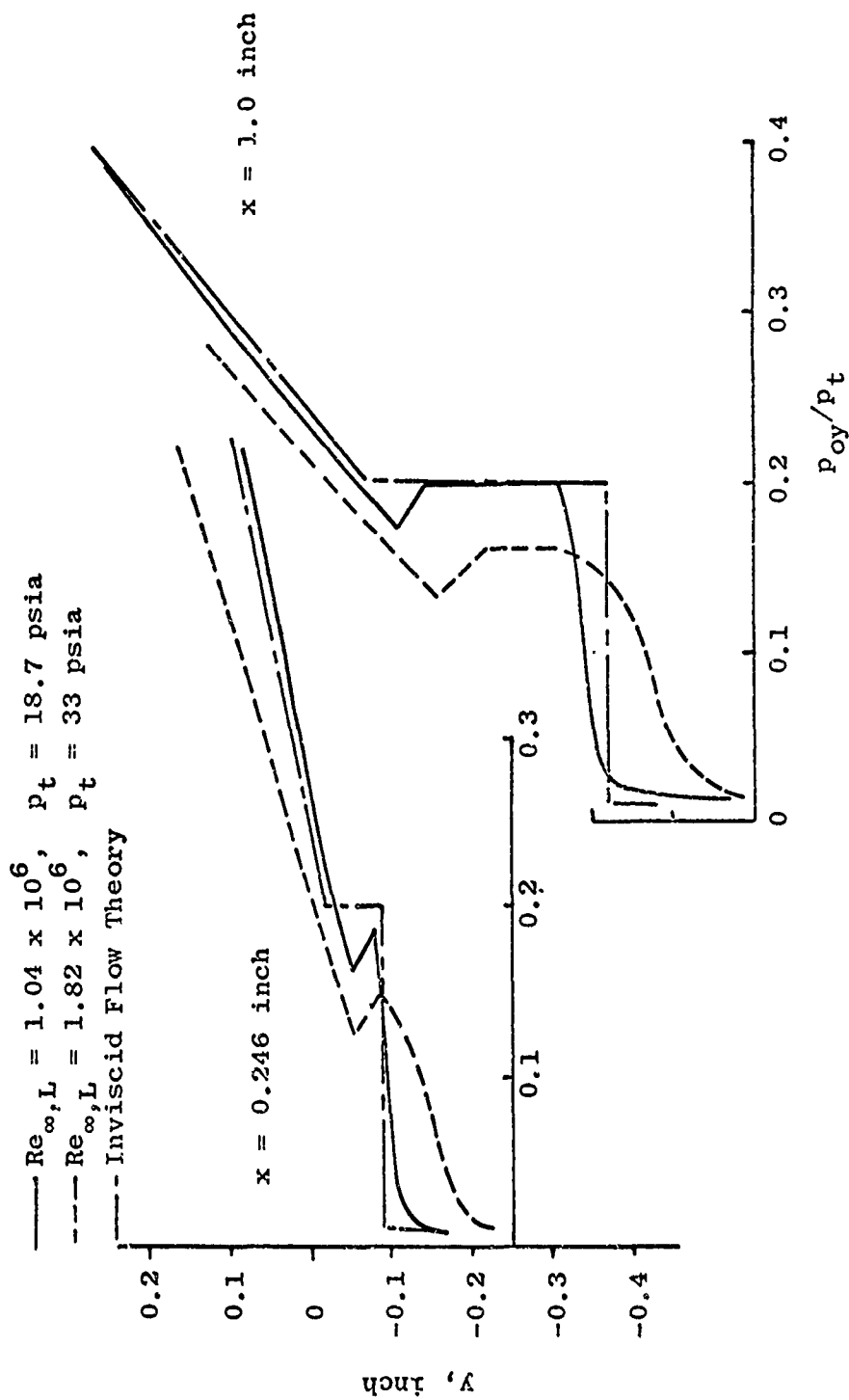


Fig. 30. Pitot Measurements of Different Reynolds Number Flow at $M = 2.5$.

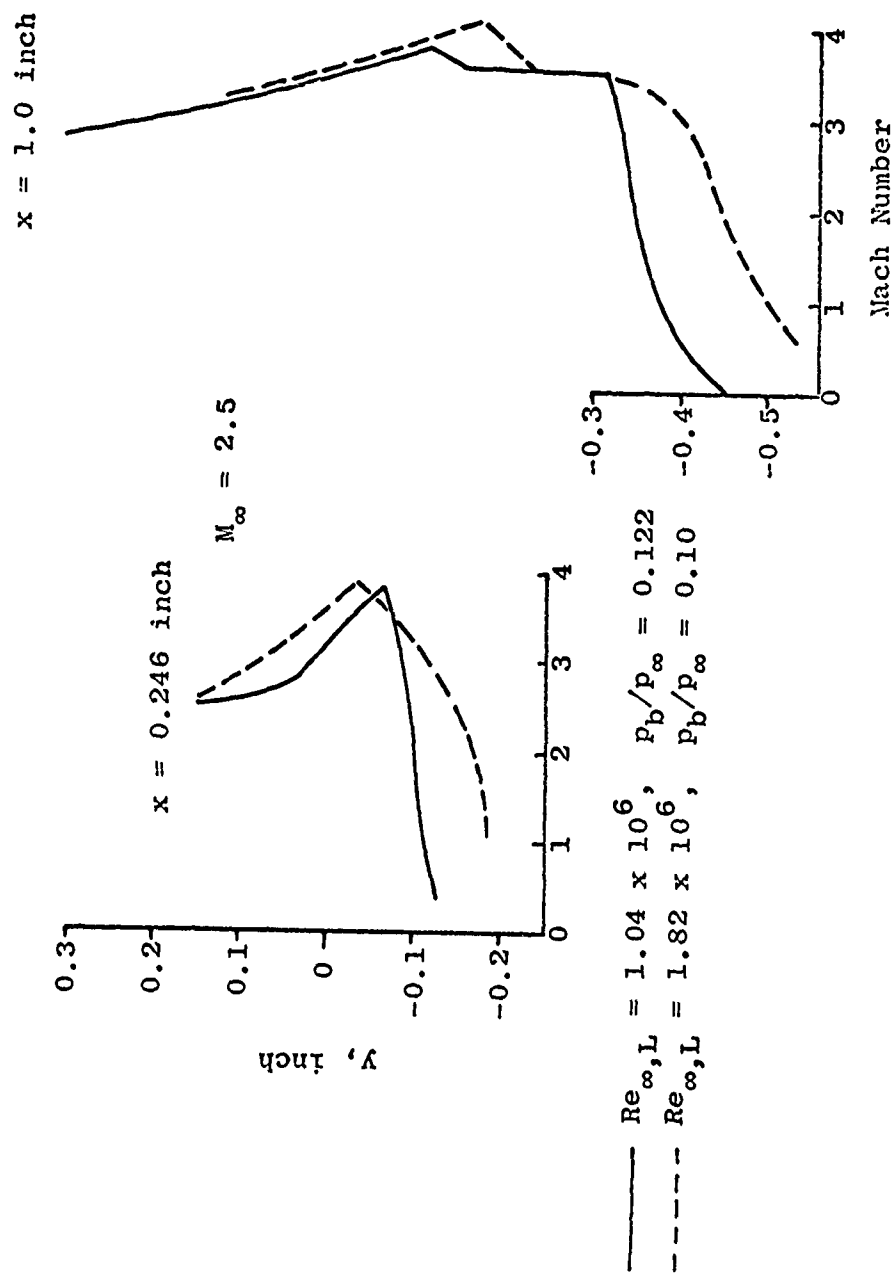


Fig. 31. Shear Layer Mach Number Profiles for Different Reynolds Number Flows at $M_\infty = 2.5$.

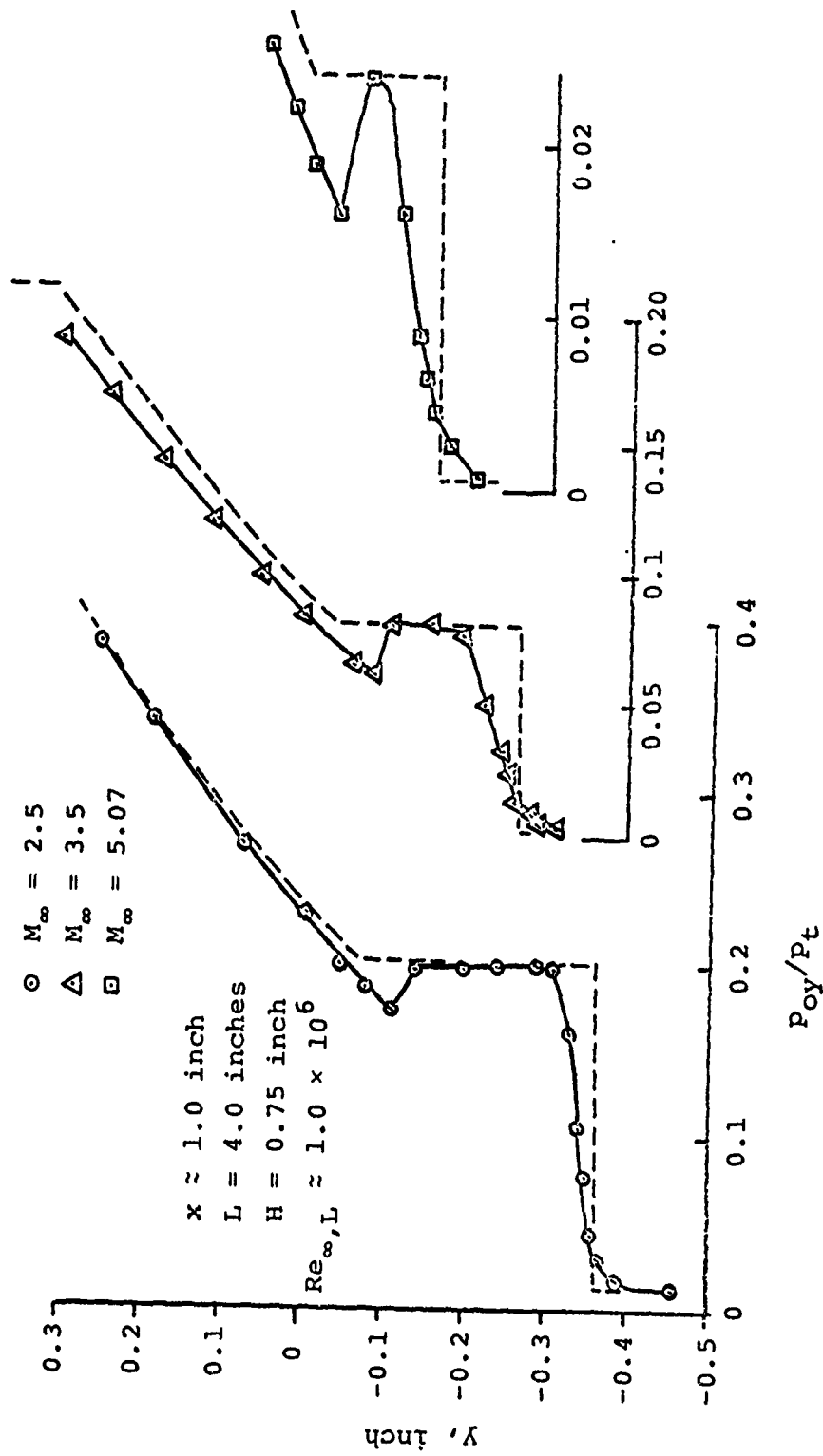


Fig. 32. Comparison of Free Stream Mach Number Effects at a Fixed Reynolds Number.

prediction are more severe at the high free stream Mach number flow as can be seen. The lip shock also turns outward as the free stream Mach number increases. Note also that the thickness of the free shear-layer increase as the Mach number increases while the region of the uniform inviscid flow downstream of the lip shock decreases (Fig. 33 and also see Fig. 22, 23, 24). At $M_\infty = 5.0$, within a distance of one step height downstream, there is no evidence of the existence of a uniform-flow region between the shear-layer and the lip shock. The lip shock is embedded in the shear-layer for a greater distance.

6. INFLUENCE OF STEP HEIGHTS

The effects of step height on the expanded and separated flow field are shown in Fig. 33 for $M_\infty = 3.5$, $Re_{\infty,L} = 1.05 \times 10^6$. The step heights are 0.75 inch and 0.44 inch respectively. It seems that the upstream influence due to different step heights is negligible in that the expanded profiles above the lip shock are very similar initially. The location of the lip shocks are strongly related to the base pressures. The differences in the separated boundary-layer are mainly due to the degree of expansion. Also, the results of rotational characteristics calculation are included, the initial conditions at the separation corner are assumed identical to that of Fig. 26. This provides further evidence that the rotational characteristics are adequate to predict the expanded flow field.

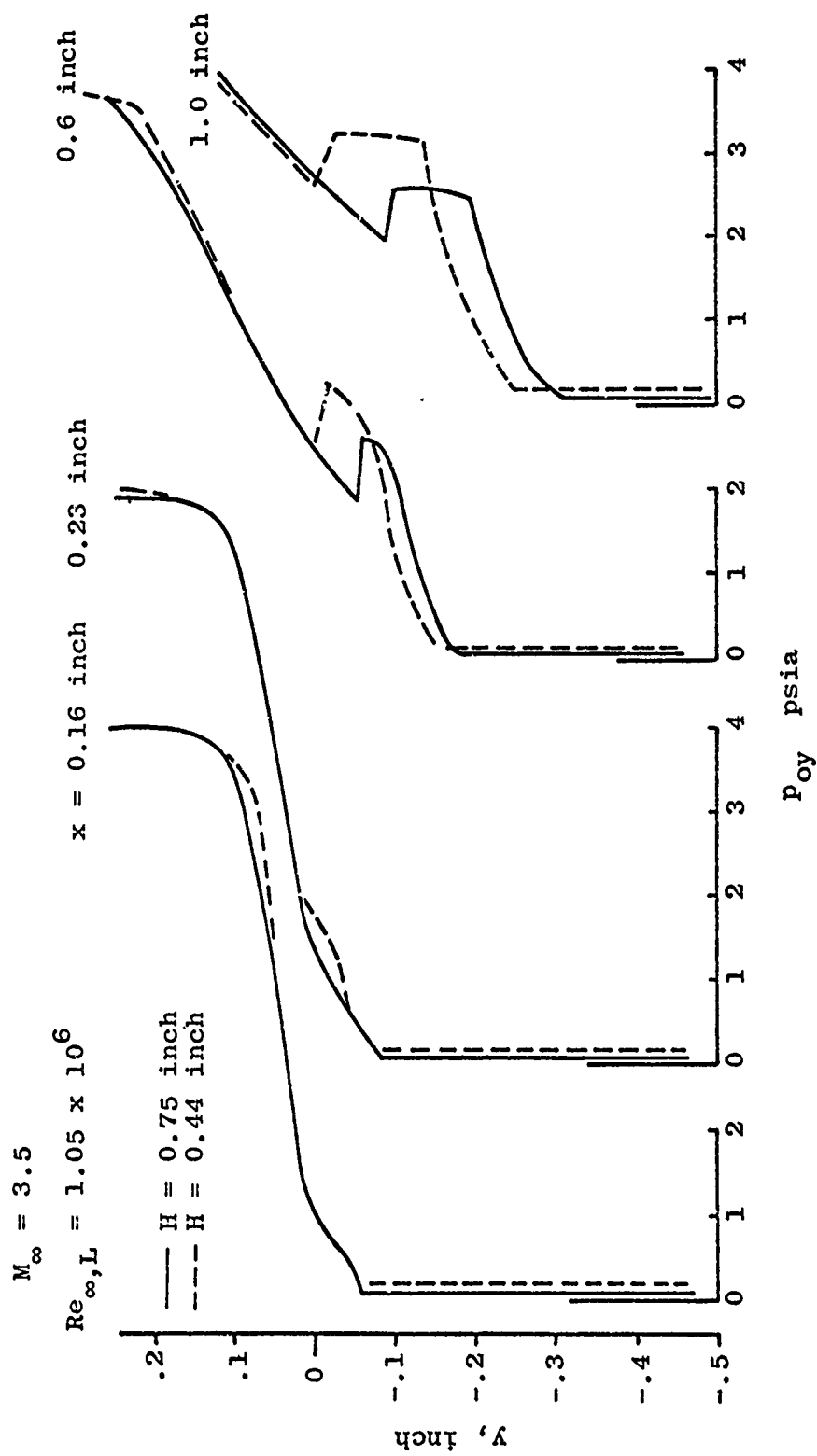


Fig. 33. Influence of Step Heights on Pitot Pressure Profiles.

CHAPTER VI

A NEW BASE PRESSURE CORRELATION

As outlined in Chapter II, detailed pressure distributions on the step were measured. This base pressure (measured on the reattachment wall close to the base of the step) is a function of Mach number and Reynolds number. A correlation of this data has been attempted as outlined below.

In a local separation region, a Reynolds number based on the characteristic length of the body is not necessarily related to the physical aspects of the local conditions. For a base flow, it is easily sensed that the characteristic lengths are the shear length ℓ_m and the mixing width Δ_m in the recompression region (see Fig. 34). An attempt has been made to correlate the base pressure with these two lengths, and a very encouraging correlation was obtained. The only difficulty is that the lengths ℓ_m and the Δ_m are not known a priori. Therefore, these two lengths must be related to the known body lengths; namely, the model length upstream of a two dimensional rearward facing step L and the step height H . Physically, the length L is related to the boundary layer thickness δ prior to separation, and this parameter will influence the mixing width Δ_m . The step height H is related to the shear layer length ℓ_m , when the other flow parameters are held constant.

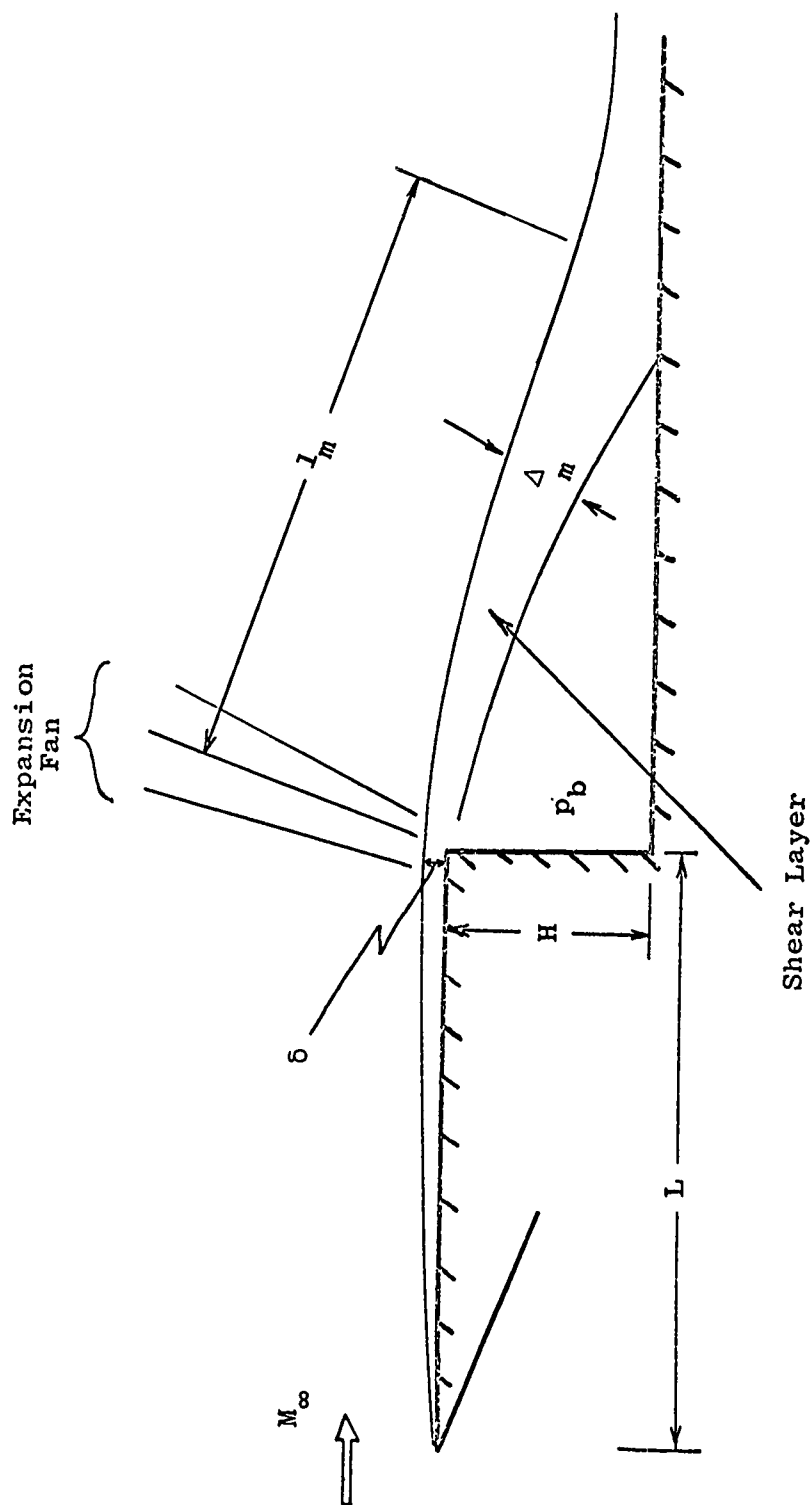


Figure 34. Parameters pertinent to the base pressure correlation. Shock-waves are omitted from this diagram for clarity.

The ratio of inertia to viscous forces in the shear layer, or the physically correct reduced Reynolds number Re_c in this region, may be expressed as:

$$Re_c = \frac{\rho_\infty U_\infty (U_\infty / \ell_m)}{\mu_\infty (U_\infty / \Delta_m)^2} = \frac{\rho_\infty U_\infty \ell_m}{\mu_\infty} \left(\frac{\Delta_m}{\ell_m} \right)^2 \quad (33)$$

where ℓ_m and Δ_m are taken as the characteristic dimensions of the mixing region as indicated above. The estimation of ℓ_m and Δ_m is often difficult. If one assumes that

$$\ell_m \sim H \quad (34)$$

$$\frac{\Delta_m}{\delta} \sim \left(\frac{\ell_m}{\delta} \right)^n \sim \left(\frac{H}{\delta} \right)^n (Re_{\infty, L}, M_\infty) \quad (35)$$

where the exponent n is a function of free stream Reynolds number based on L and the free stream Mach number M_∞ . The exponent n may depend strongly on whether the shear layer is laminar, transitional or turbulent. Based on equations (34) and (35), the reduced Reynolds number Re_c of Equation (33) becomes,

$$Re_c = \frac{\rho_\infty U_\infty H}{\mu_\infty} \left(\frac{H}{\delta} \right)^{2n - 2} \quad (36)$$

If one also neglects the dependence of δ on Mach number, then,

$$\frac{\rho_{\infty} U_{\infty} H}{\mu_{\infty}} = \left(\frac{\rho_{\infty} U_{\infty} L}{\mu_{\infty}} \right) \left(\frac{H}{L} \right) \sim \left(\frac{H}{\delta} \right)^m \left(\frac{L}{H} \right)^m \left(\frac{L}{H} \right)^{-1} \quad (37)$$

and

$$Re_c = \left(\frac{H}{\delta} \right)^{m + 2n - 2} \left(\frac{L}{H} \right)^{m - 1} \quad (38)$$

where for very small pressure gradient flow, m is (approximately) 2 or 5 depending on whether the boundary layer on the body is laminar or turbulent respectively. The reduced Reynolds number is thus related to δ , H and L , which are the important parameters of the base flow. This reduced Reynolds number is very likely to be a correlation parameter for the base pressure.

Based on their mixing theory, Crocco and Lees [4] were able to show the important trends in the variation of base pressure with Reynolds number, L/H and the nature of the boundary layer. They argued that the base pressure is a function of the mixing rate and of δ . The mixing rate and δ depend not only on Reynolds number but also on the location of transition (whether this be on the body or in the separated region). For an intermediate wake transition region, the

rate of upstream movement of transition in the wake with increasing Reynolds number is governed largely by the parameter L/H . For fully laminar or turbulent flow, where L/H is not as important, the base pressure ratio then depends mainly on the ratio δ/H ; as correlated by Chapman [45]. For transitional wake flow, $m = 2$ is appropriate, and if it is assumed that $n = 0.9$, the correlation parameter reads

$$Re_c \sim \left(\frac{H}{\delta} \right)^{1.8} \left(\frac{L}{H} \right) \sim Re_{\infty, H}^{0.9} \left(\frac{L}{H} \right)^{0.1} \quad (39)$$

Because of the contrast in dependence of the base pressure on the mixing rate and on the boundary layer thickness (as pointed out by Crocco and Lees [4]), it is proposed to normalize the base pressure ratio with the correlation parameter. The correlation is shown in Fig. 35 for the data the range of the data is as follows (see Table 1):

$$0.05 \times 10^6 < Re_{\infty, L} < 1.8 \times 10^6$$

$$2.0 < M_{\infty} < 3.55$$

$$5.33 < L/H < 31.4$$

$$0.0072 \text{ inch} < H < 0.75 \text{ inch}$$

The proposed base pressure correlation for a two dimensional rearward facing step is,

*This value has been found empirically.

Table 1. Base Pressure Correlation.

Symbol	M_∞	H, inch	L/H	Investigators
○	2.50	0.7500	5.33	Present
△	3.50	0.7500	5.33	Present
◦	2.50	0.4400	9.03	Smith
△	3.50	0.4400	9.03	Smith
◇	2.00	0.0100	20.00	Chapman
○	2.00	0.1000	20.00	Chapman
X	2.25	0.0072	31.40	Rom
⊗	3.55	0.0072	31.40	Rom
○	2.25	0.0165	13.20	Rom
◇	3.55	0.0165	13.20	Rom
◇	2.25	0.0256	13.00	Rom
◇	3.55	0.0256	13.00	Rom
◻	2.25	0.0335	7.40	Rom
◻	3.55	0.0335	7.40	Rom
◻	2.25	0.0790	8.00	Rom
◻	3.50	0.0790	8.00	Rom
◻	2.25	0.0790	15.00	Rom
◻	3.50	0.0790	15.00	Rom
◻	5.00	0.7500	5.00	Present

Source: H. E. Smith, "The Flow Field and Heat Transfer Downstream of a Rearward Facing Step in Supersonic Flow," Aerospace Research Laboratory Report No. 67-0056 (Wright-Patterson Air Force Base, Ohio, March, 1967).

Source: D. R. Chapman, D. M. Kuehn, and H. K. Larson, "Investigation of Separated Flows in Supersonic and Subsonic Streams with Emphasis on the Effect of Transition," National Advisory Committee for Aeronautics Report No. 1356 (Washington, D. C., June, 1958).

Source: J. Rom, "Supersonic Flow over Two-Dimensional and Axially Symmetric Backward Facing Steps," TAE Report No. 33 (Department of Aeronautical Engineering, Technion-Israel Institute of Technology, Haifa, Israel, March, 1964).

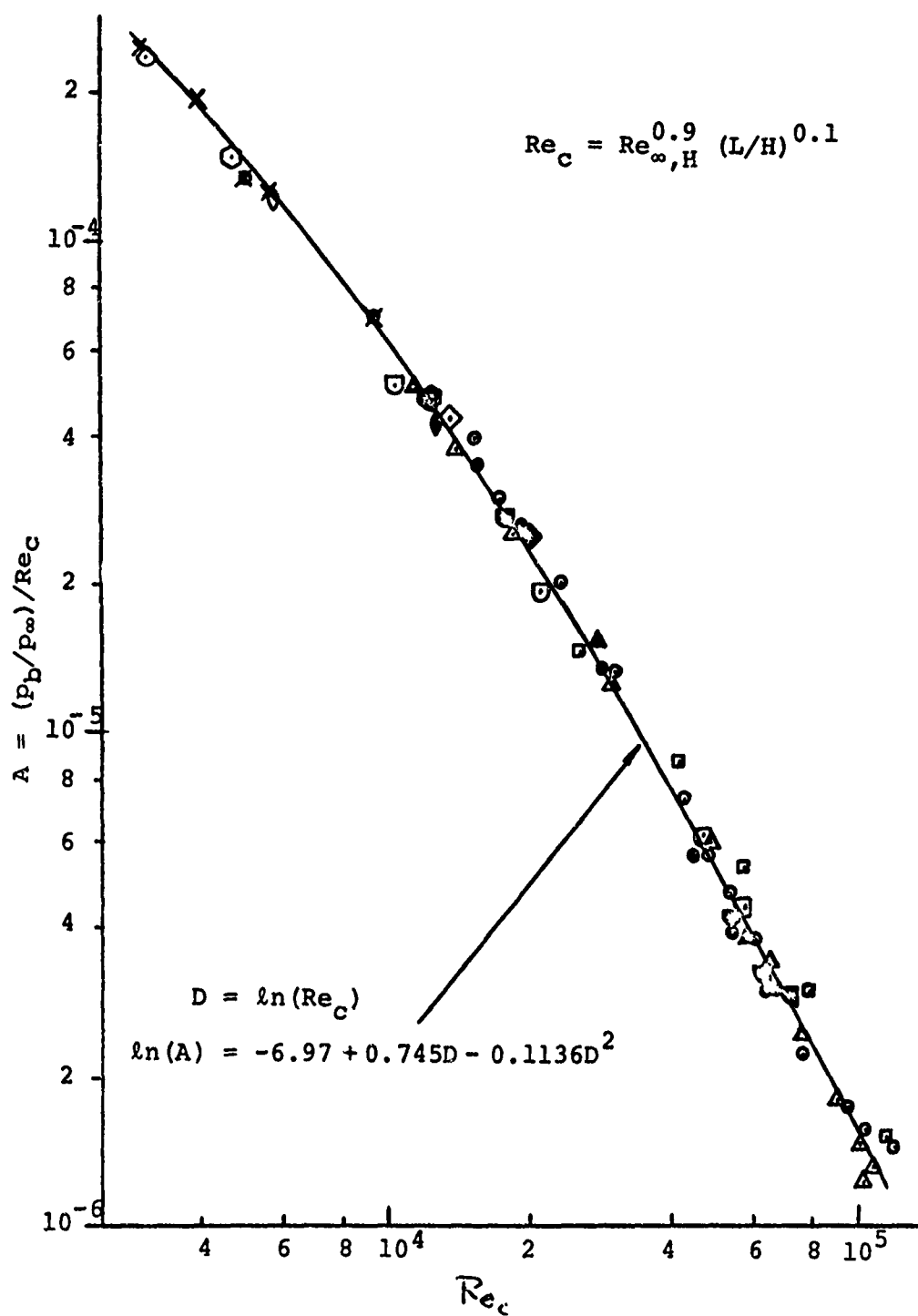


Figure 35. Base Pressure Correlation.

$$\frac{P_b}{P_\infty} = Re_c \exp(-6.97 + 0.745D - 0.1136D^2) \quad (40)$$

where $D = \ln(Re_c)$

The comparison of measured base pressure ratio and the base pressure ratio computed by Equation (40) is shown in Fig. 36, which indicates that the correlation is indeed a reasonable one.

Similar correlation for a 6 degree wedge [8] is shown in Fig. 37. Note that in both Figs. 35 and 37, the body boundary layer is laminar before separation, and that this correlation parameter applies to fully laminar flow as well.

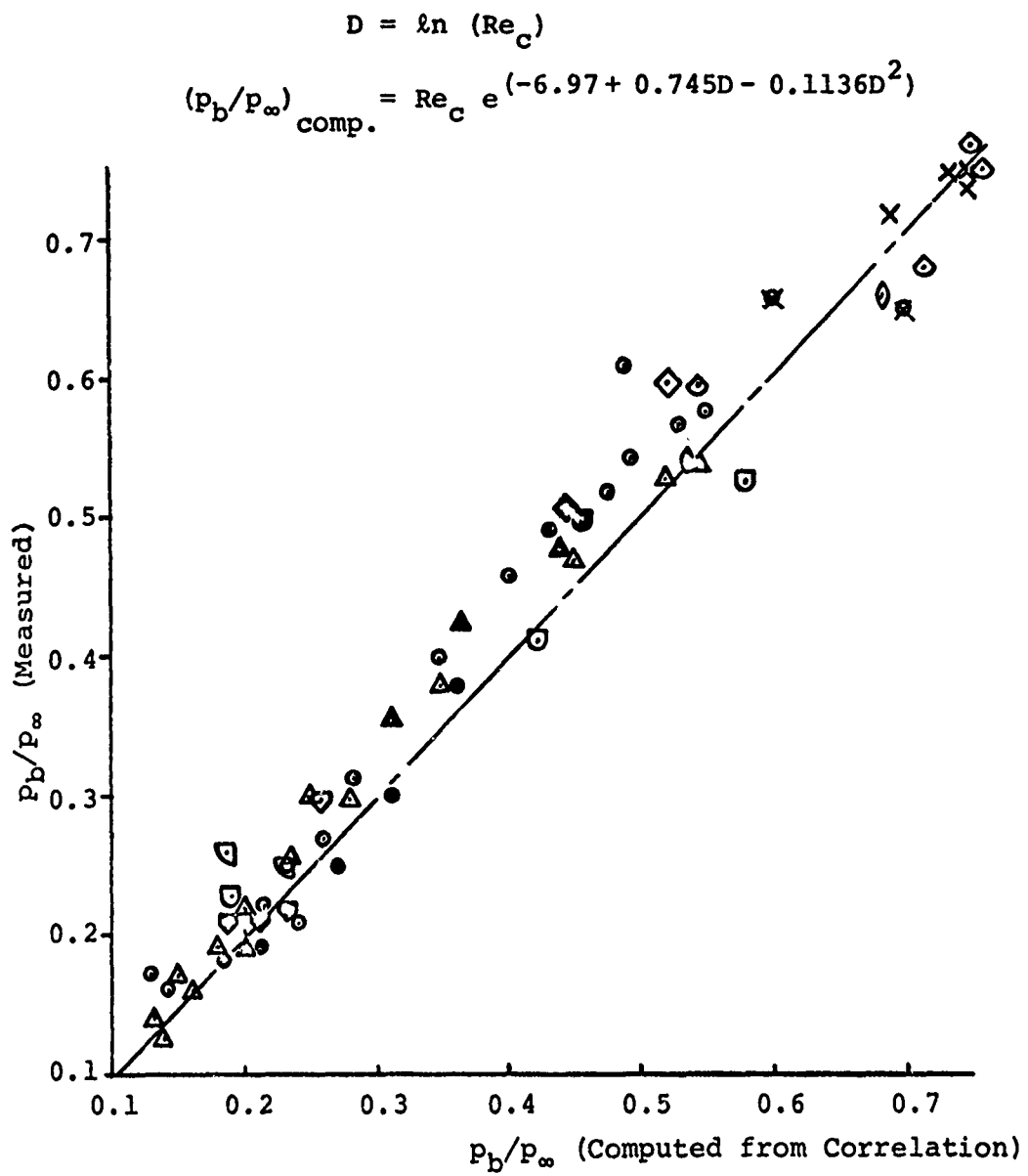


Figure 36. Comparison of Measured Base Pressure and Base Pressure Computed from Correlation.

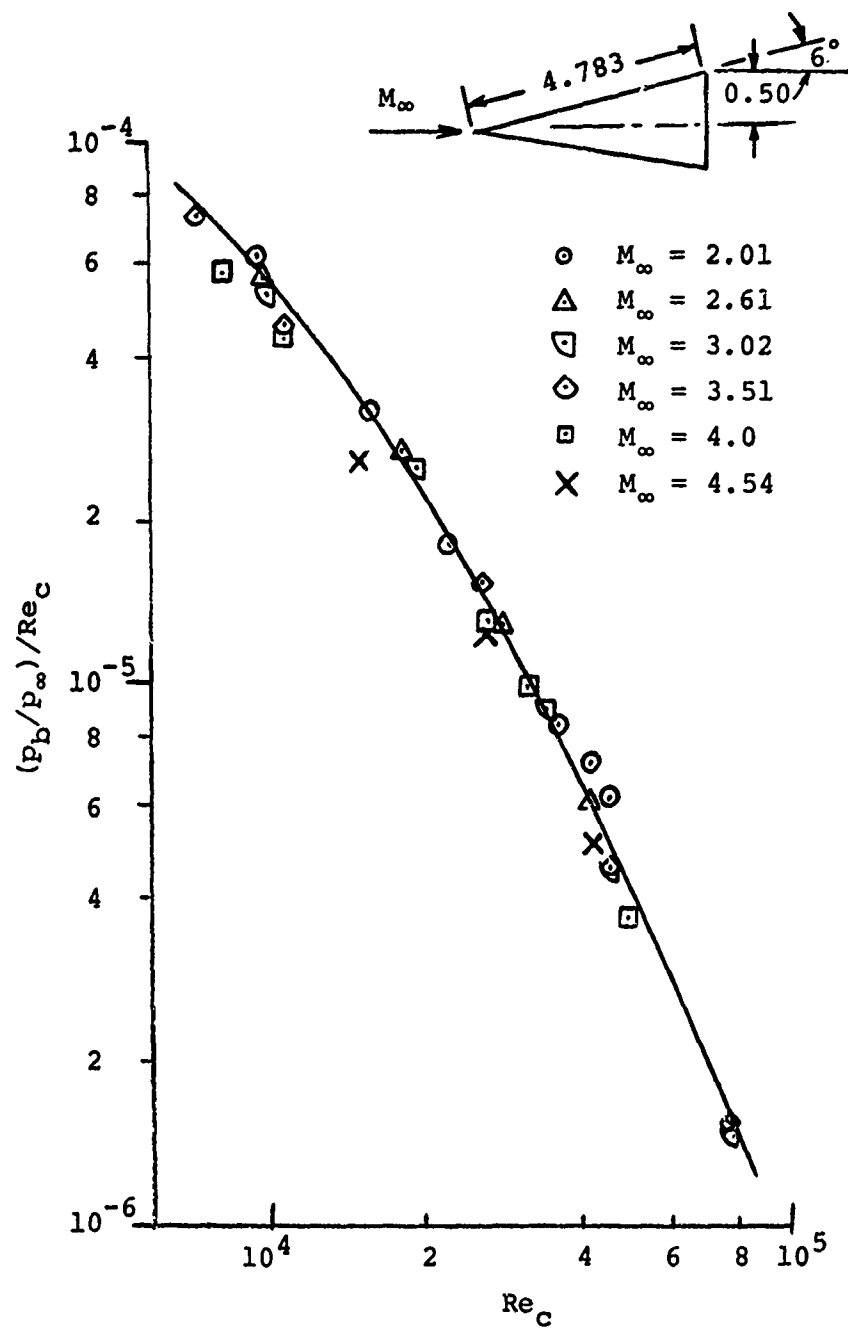


Figure 37. Base Pressure Correlation for Six Degree Wedge.

CHAPTER VII

THE INFLUENCE OF AN OVERHANG MOUNTED AT THE SEPARATION CORNER

It has been postulated that the dividing streamline actually turns sharply around the separation corner and then separates from the surface of the step [8, 57, 58]. Whatever the mechanism of the separation, it is possible to change the conditions at separation by changing the step geometry in this region. In order to determine the effect of different conditions at separation, a thin (0.02 inch) overhang of various lengths was added to the basic model. The inset on Fig. 39 shows the overhang attachment.

A theoretical model that assumes a 'dead-air' region downstream of the step would not differentiate between the plain step and the step with overhang. Indeed, for low supersonic flow Nash et al [55] reported no measurable effect on base pressure by the introduction of an overhang configuration. The same comment was not true in subsonic flow; but a discussion of that flow is not the subject of the present work. If there are any differences between the two flows it must result from changes in the geometry of the streamlines in the "dead-air" region near the separation point. This could have some effect on the mixing

$$M_{\infty} = 3.5$$

x measured from
expansion corner

	L_{oh}	L_c	$Re_{\infty, L}$
●	0.0	0.0	1.18×10^6
▲	0.188	0.688	1.38×10^6
▽	0.375	0.875	1.44×10^6
□	0.750	1.250	1.55×10^6

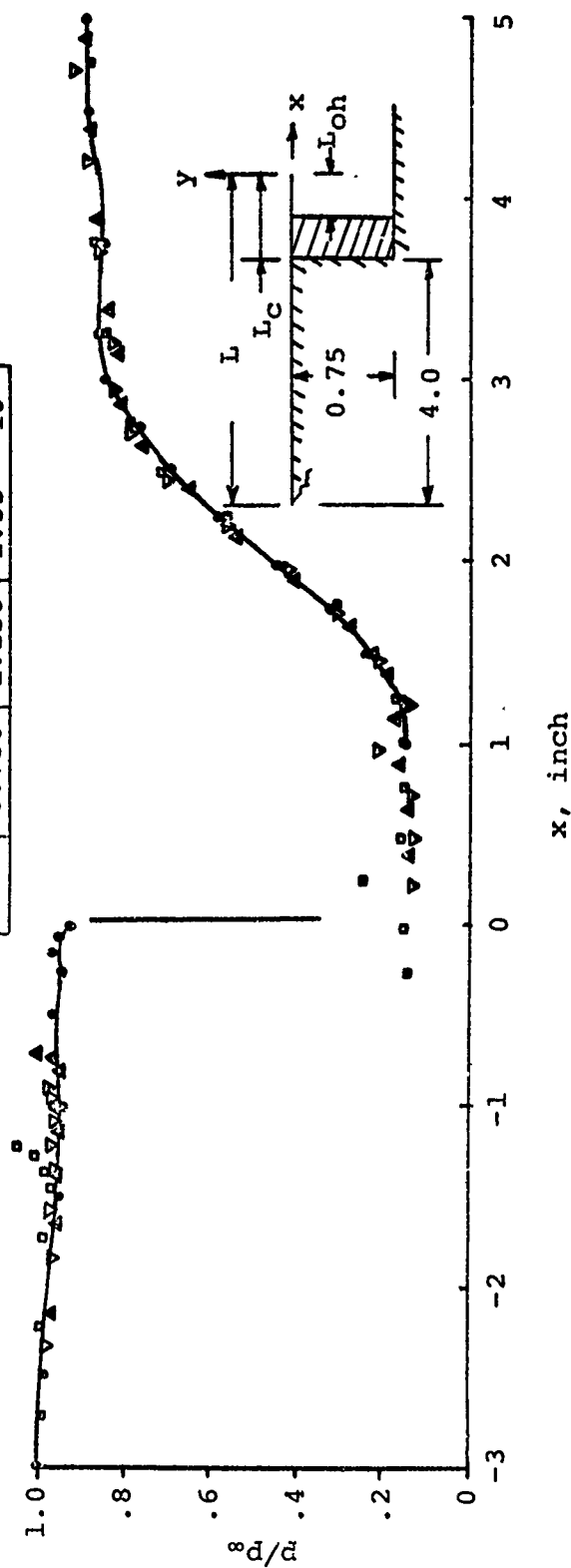


Figure 38. Surface Pressure Distributions with and without Overhang at $M_{\infty} = 3.5$.

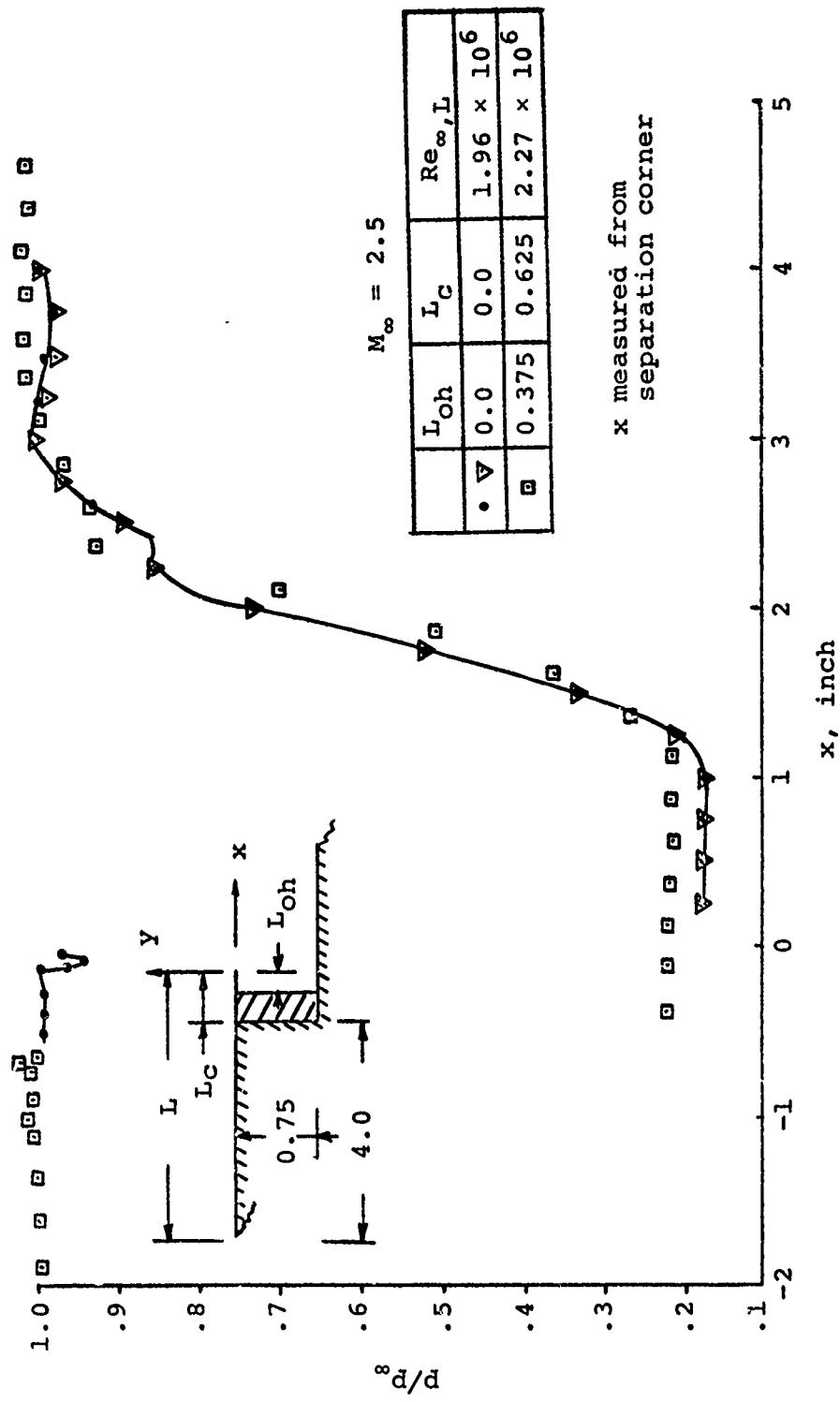


Figure 39. Surface Pressure Distributions with and without Overhang at $M_\infty = 2.5$.

in the shear layer due to modifications of the velocity profiles.

It is considered that this effect will not be too large [59].

The results shown in Figures 38 and 39 are not immediately interpretable. Thus at a Mach number of 3.5 (Figure 38), there is no noticeable change in base pressure with configuration. The base pressure correlation (equation 40) shows a very small change in base pressure over the Reynolds number of the test data. For a Mach number of 2.5 (Figure 39), the data shows an increase of base pressure with the introduction of an overhang; which is opposite to the effect anticipated from the change of Reynolds number. This inconsistency of the data with change in Mach number suggests that further studies should be made.

CHAPTER VIII

HOT-WIRE MEASUREMENTS IN RECIRCULATING REGION AND FREE SHEAR LAYER

1. GENERAL DISCUSSION

Hot-wire anemometer probes were used to explore the basic structure of the recirculating region*. The major difficulties encountered in these measurements were:

1. The Reynolds number based on the wire diameter was very low (about 0.2 to 9).
2. Abrupt velocity and total temperature gradients were present in the free shear layer.

Considerable effort has been expended in developing a satisfactory data reduction technique, which was presented in Chapter III.

The continuous hot-wire resistance traces at constant current (7×10^{-3} amp) are presented in Figure 41. The striking changes in resistance are due to the combined effects of changes in heat transfer rate and the adiabatic wire temperature as indicated by Equation (12). However, calculation based on Equation (13) shows that at small current the wire measures essentially the adiabatic wire temperature, which is the product of recovery factor η and the local total temperature T_o , i.e., $T_{aw} = \eta T_o$.

*Analytical work was performed by Scherberg (15) who found the core streamline structure with essentially zero pressure gradients in the y direction.

- Dividing Streamline
 - Zero "u" Velocity Line
- $M_\infty = 3.5, \quad Re_{\infty, L} = 1.2 \times 10^6,$
 $I = 7 \times 10^{-3} \text{ amps}$

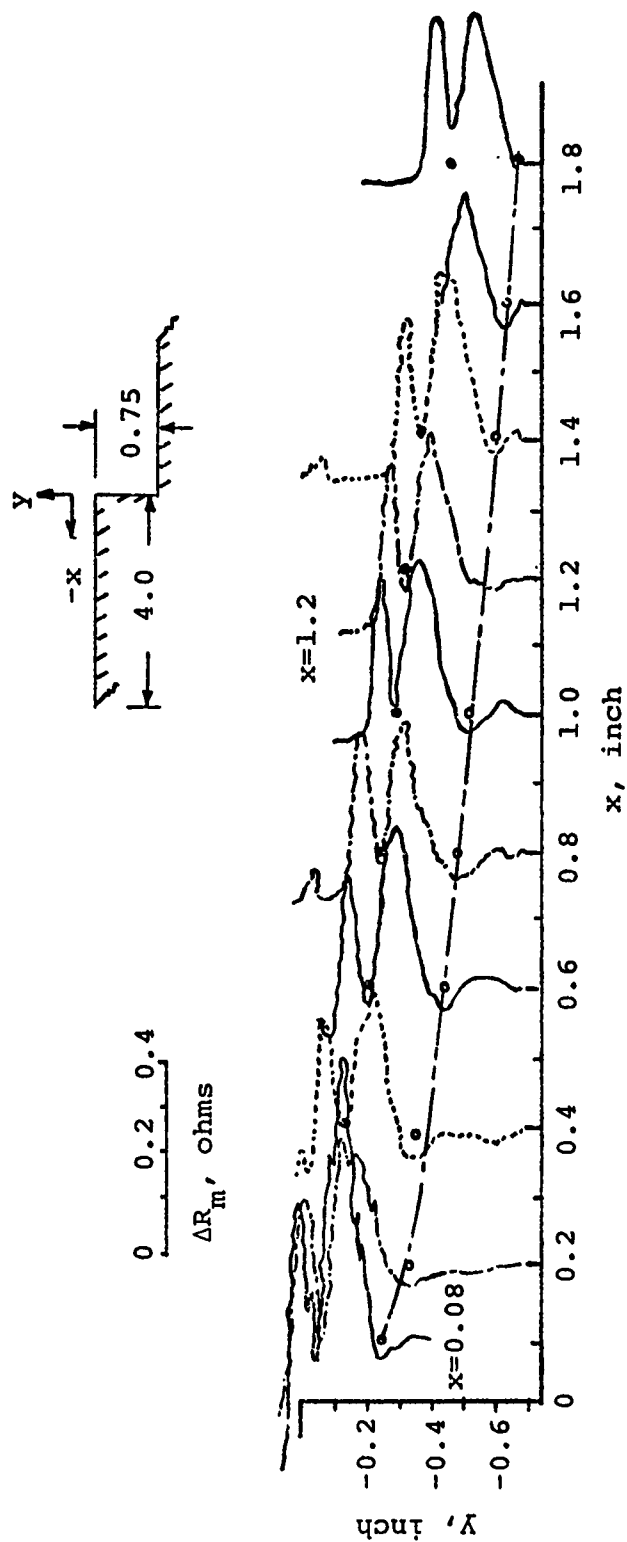


Figure 40. Continuous Hot-Wire Resistance Mapping.

In the region of the measurements, the recovery factor of the wire varies from 1.0 to about 1.08, depending on the local Mach number and Knudsen number. The local total temperature in the free shear layer and recirculating region is not uniform. Therefore, the measured relative minimum resistances (minimum T_{aw}) are primarily due to either low total temperature or lower recovery factor. The minimum resistance further away from the wall, as shown in Figure 40, is due to the lower T_o along the dividing streamline. This point will be discussed in greater detail later. While the other minimum resistance is due to the lower recovery factor at the lower Mach number (or minimum velocity), the recovery factor decreases to unity regardless of Knudsen number in the range investigated as the Mach number approaches zero (Figure 59, Appendix F).

Figure 41 reports the typical static pressure, pitot pressure and hot-wire resistance measured at $x/H = 1.14$. The comparison shows the necessity of employing hot-wire techniques for measurements in the lower portion of the free shear layer and in the recirculating region.

There is some doubt as to the effect of turbulence on the wire resistance measurements, since part of the free shear layer is transitional. However, estimations indicate that this is negligible, and this is discussed further in Appendix F.

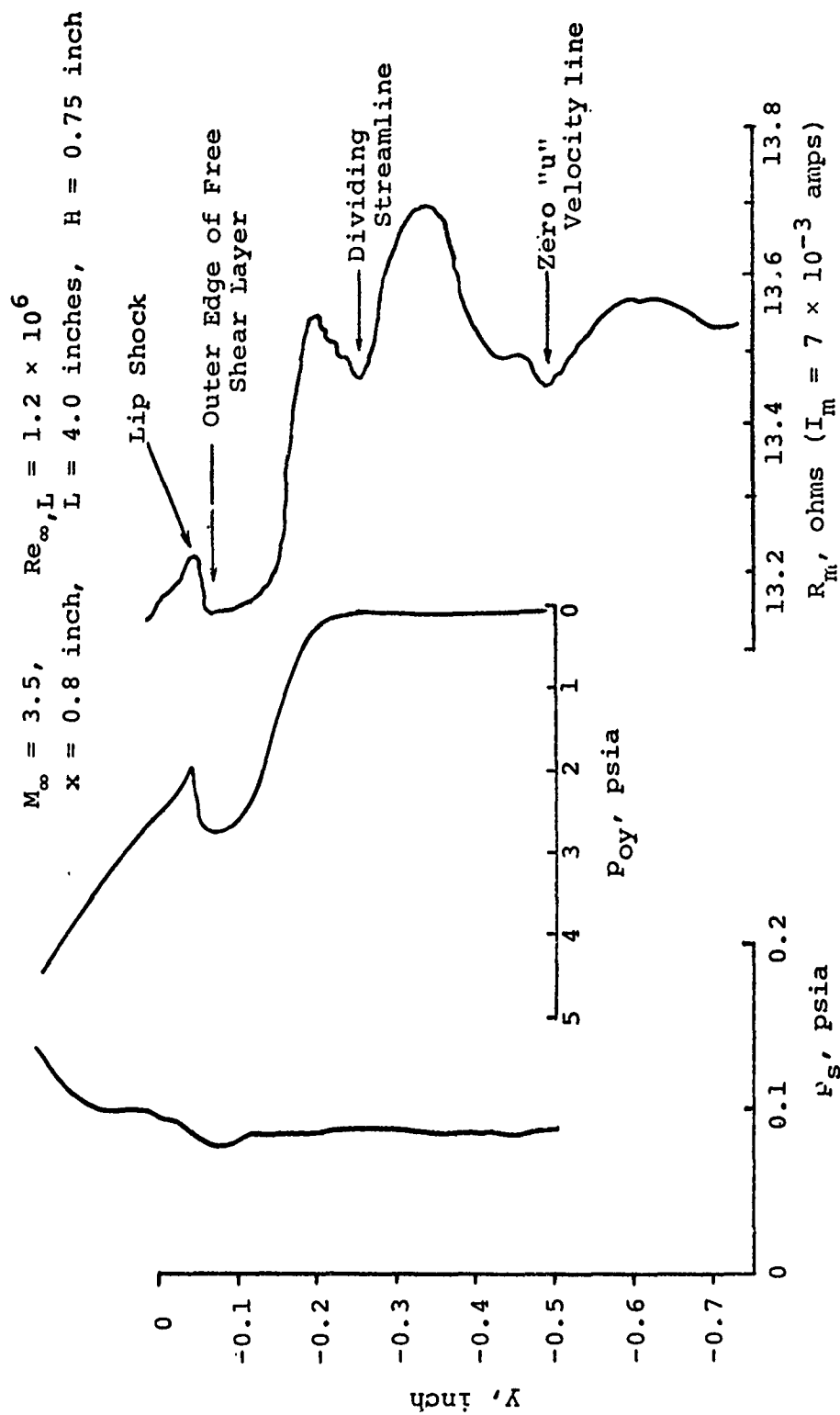


Figure 41. Comparison among Measured Hot-Wire, Pitot and Static Pressure Profiles.

2. REDUCED RESULTS

The variation of various flow properties in the free shear layer and the recirculating region are shown in Figure 42. h and T_{aw} are directly reduced from hot-wire measurements. The broken line represents values reduced from continuous resistance traces which are not as accurate as the discrete measurements. By combining h , T_{aw} and p_s , the other flow parameters such as Mach number and total temperature are then determined by the method described in Chapter III. The Nusselt number decreases very sharply in the free shear layer and it varies also in the recirculating region. The Knudsen number increases from 0.2 at the outer edge of the free shear layer to 1.8 in the recirculating region indicating that the hot-wire was in the transitional (slip flow) regime. The distribution of Reynolds number based on wire diameter ($Re_{wd} \lesssim O(1)$), which is essentially the mass flux distribution, is also shown in Fig. 42.

The wire recovery temperature and convective heat transfer rate for various stations in the recirculating region and shear layer are shown in Figures 43 and 44 respectively. The basic features of the recirculating region can be seen more clearly from the following reduced results.

The Mach number mapping is presented in Fig. 45 with the dividing streamline and an approximate indication of the zero "u" component of velocity shown. Although the Mach number is positive below the latter line, the

$\bullet \Delta$ Point by Point Measurements
 --- Continuous Traces
 $M_\infty = 3.5,$
 $x = 0.8$ inch,
 $H = 0.75$ inch
 $Re_{\infty,L} = 1.2 \times 10^6,$
 $L = 4.0$ inches,

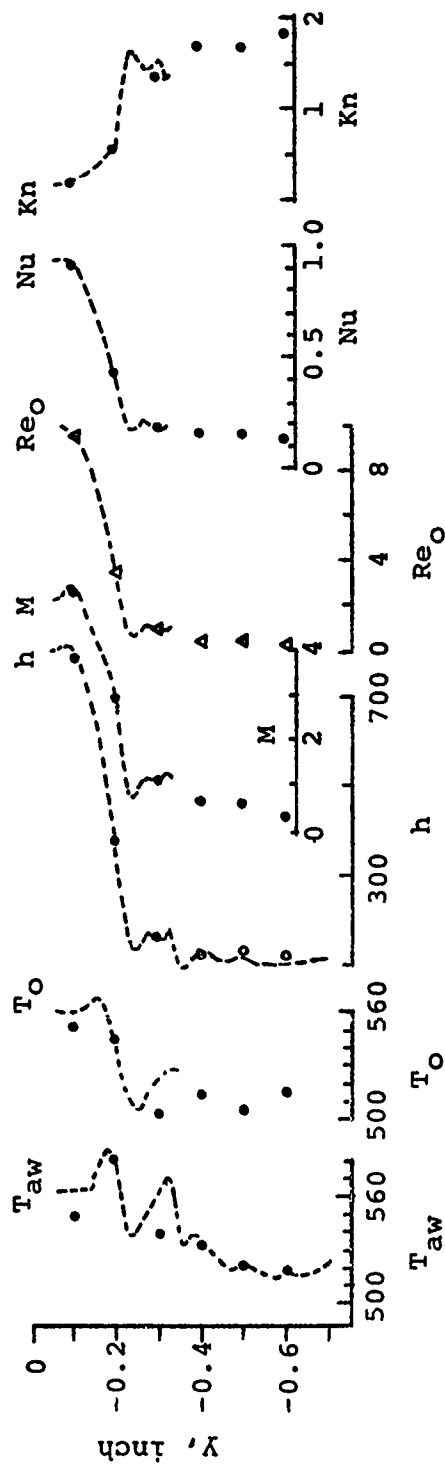


Figure 42. Typical Reduced Results from Hot-Wire Measurements.

$M_\infty = 3.5,$ $Re_\infty, L = 1.2 \times 10^6,$ --- Continuous Traces
 $L = 4.0$ inches, $H = 0.75$ inch

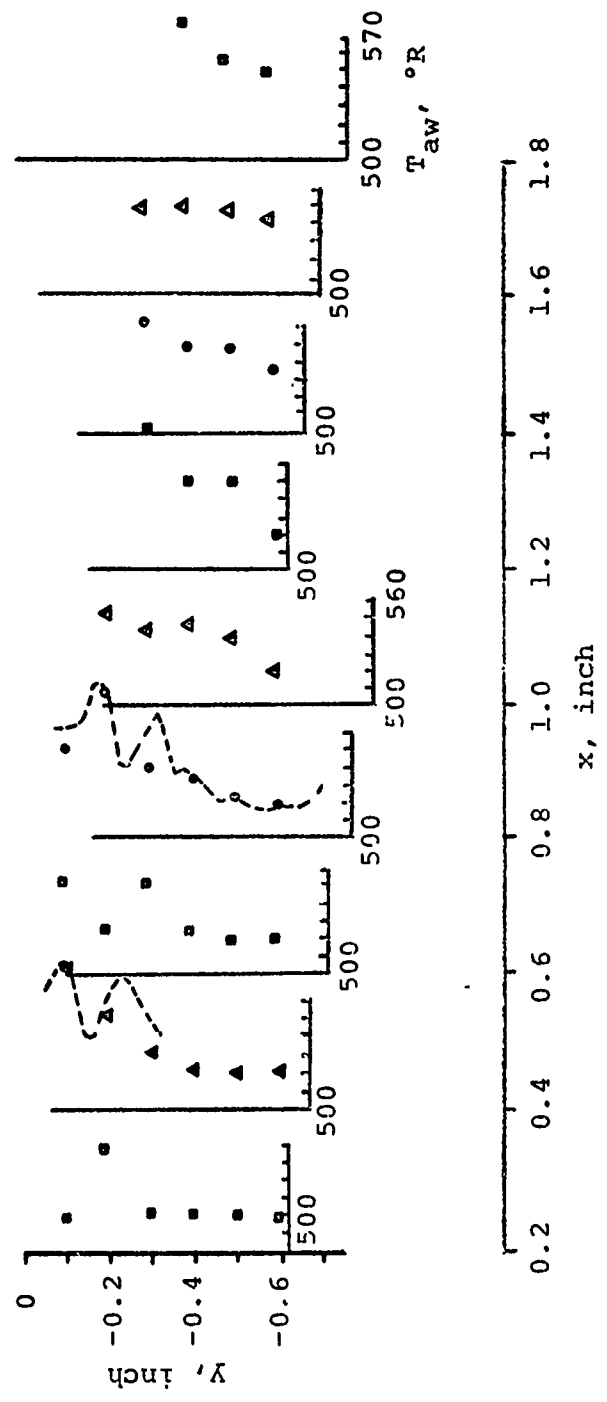


Figure 43. Hot-Wire Recovery Temperature in Recirculating Region and Shear Layer.

$M_\infty = 3.5,$ $Re_{\infty,L} = 1.2 \times 10^6,$ --- Continuous Traces
 $L = 4.0$ inches, $H = 0.75$ inch

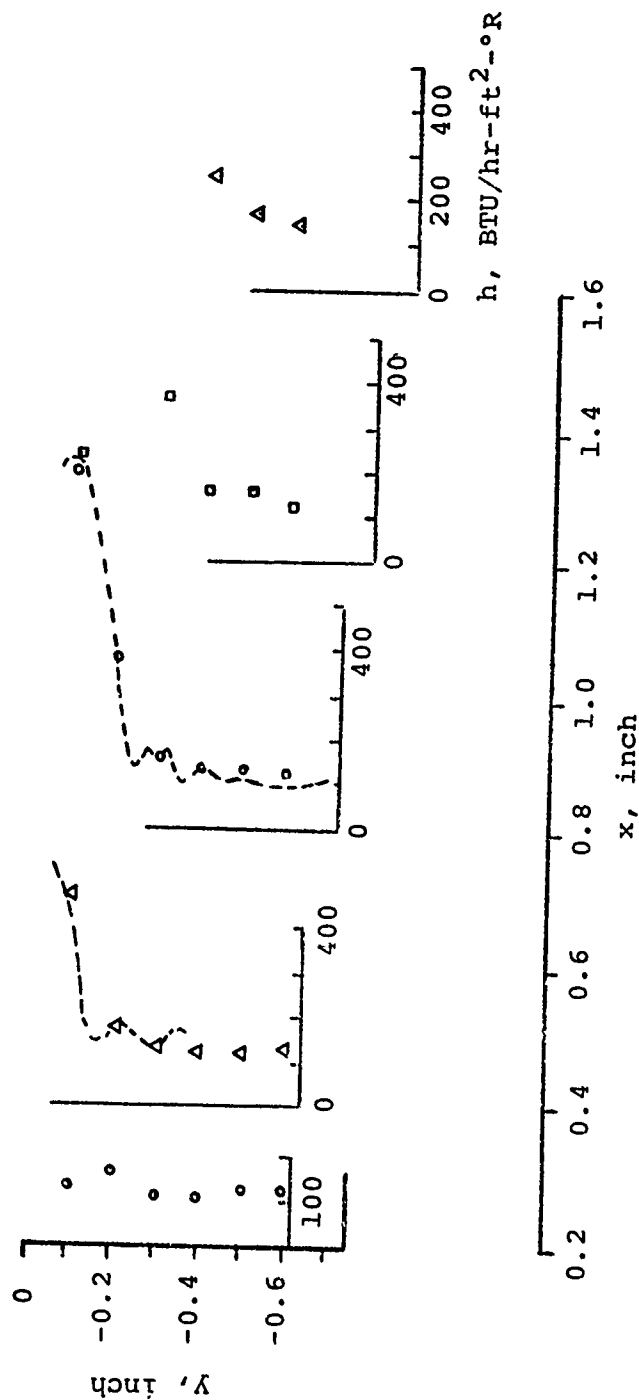


Figure 44 Hot-Wire Heat Transfer Coefficient in Recirculating Region and Shear Layer.

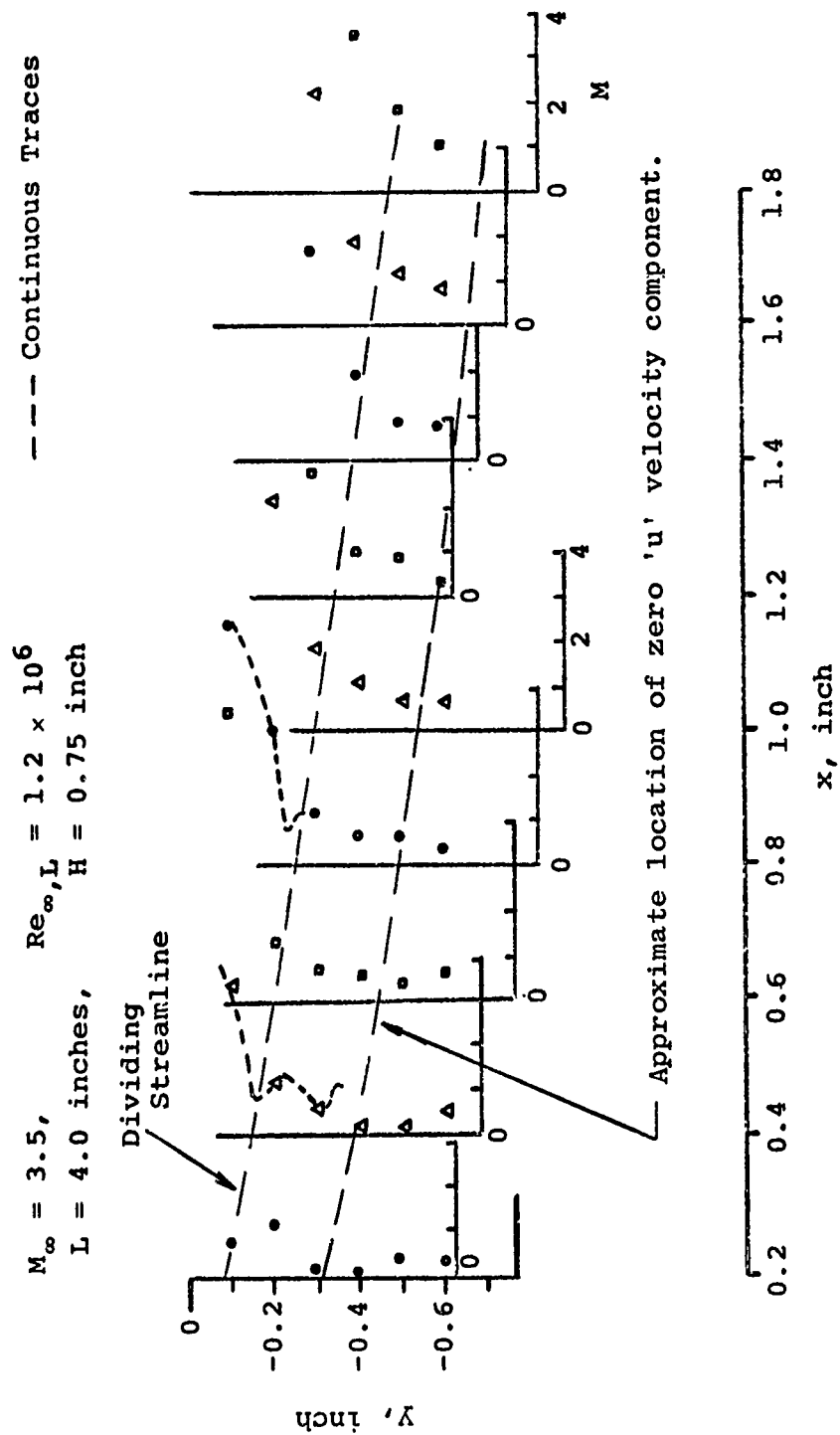


Figure 45. Mach Number in Recirculating Region and Shear Layer.

flow direction is reversed. Note, the acceleration of the flow along the dividing streamline. Since the recirculating flow is of finite velocity (but the Mach number can be as high as 0.8), the interaction between the separated boundary layer and the recirculating flow could be important.

The total temperature mapping is shown in Figure 46. The total temperature increases rather rapidly from 440°R close to the wall to 500°R within one step height distance downstream, while the rest of the recirculating region is at a nearly constant total temperature of 500°R (free stream total temperature is 560°R).

The development of the temperature profile will be discussed further in Chapter IX from a theoretical standpoint, and further deliberations will be delayed until that time.

$M_\infty = 3.5,$ $Re_{\infty,L} = 1.2 \times 10^6,$ $---$ Continuous Traces
 $L = 4.0$ inches, $H = 0.75$ inch

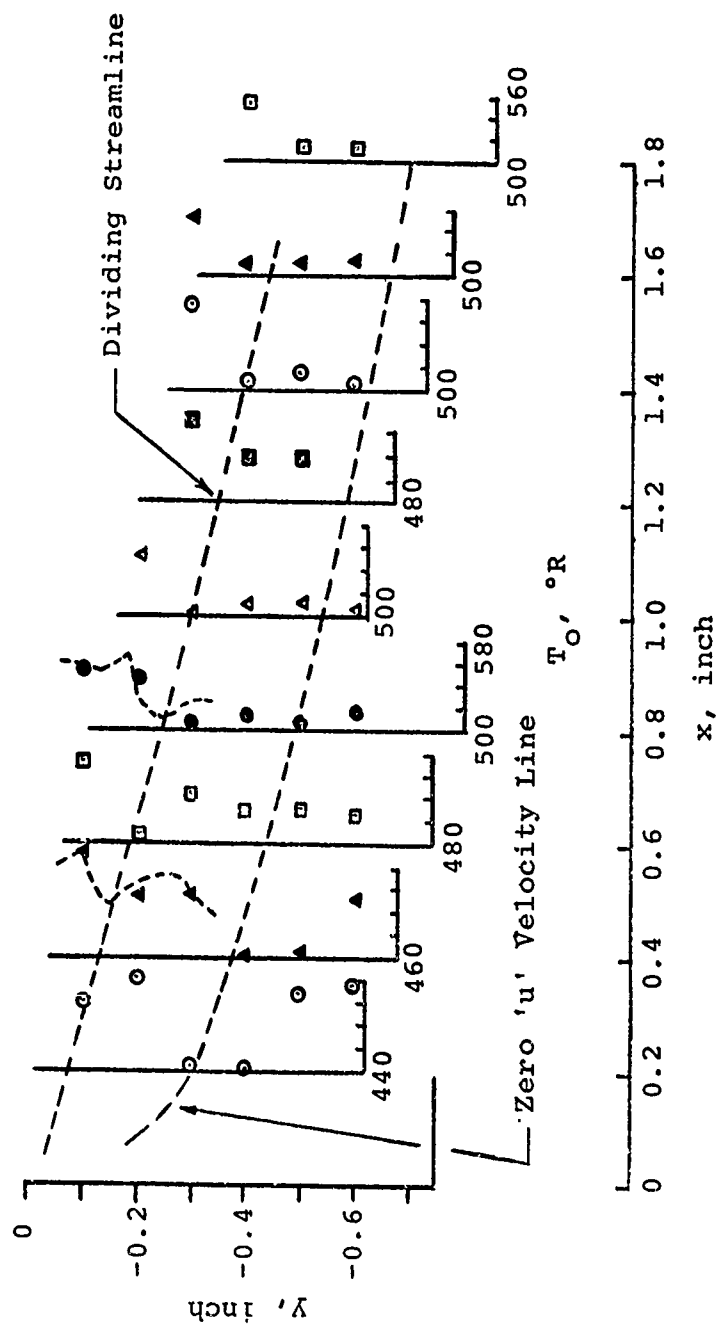


Figure 46. Stagnation Temperature in Recirculating Region and Shear Layer.

CHAPTER IX

AN ESTIMATION OF THE SHEAR-LAYER TEMPERATURE DISTRIBUTION

If the shear layer is 'thin' compared to its length, it can be assumed that the boundary-layer equations hold in a coordinate system aligned with the shear-layer (see Fig. 47), then:

$$\frac{\partial}{\partial x} (\rho u) + \frac{\partial}{\partial y} (\rho v) = 0 \quad (41)$$

$$\rho \frac{Du}{Dt} + \frac{dp}{dx} = \frac{\partial}{\partial y} \left(\mu \frac{\partial u}{\partial y} \right) \quad (42)$$

$$\rho \frac{D(TC_p)}{Dt} = \frac{\partial}{\partial y} \left(k \frac{\partial T}{\partial y} \right) + \mu \left(\frac{\partial u}{\partial y} \right)^2 + u \frac{dp}{dx} \quad (43)$$

Introducing the total temperature:

$$T_o = T + u^2/2 C_p \quad (44)$$

The energy equation then becomes:

$$\begin{aligned} \rho \frac{D}{Dt} (T_o C_p) &= \frac{\partial}{\partial y} \left(k \frac{\partial T_o}{\partial y} \right) + u \frac{\partial}{\partial y} \left[\mu \left(1 - \frac{1}{Pr} \right) \frac{\partial u}{\partial y} \right] \\ &+ \mu \left(1 - \frac{1}{Pr} \right) \left(\frac{\partial u}{\partial y} \right)^2 + \frac{\partial}{\partial y} \left[\frac{ku^2}{2C_p} \frac{\partial C_p}{\partial y} \right] \end{aligned} \quad (43a)$$

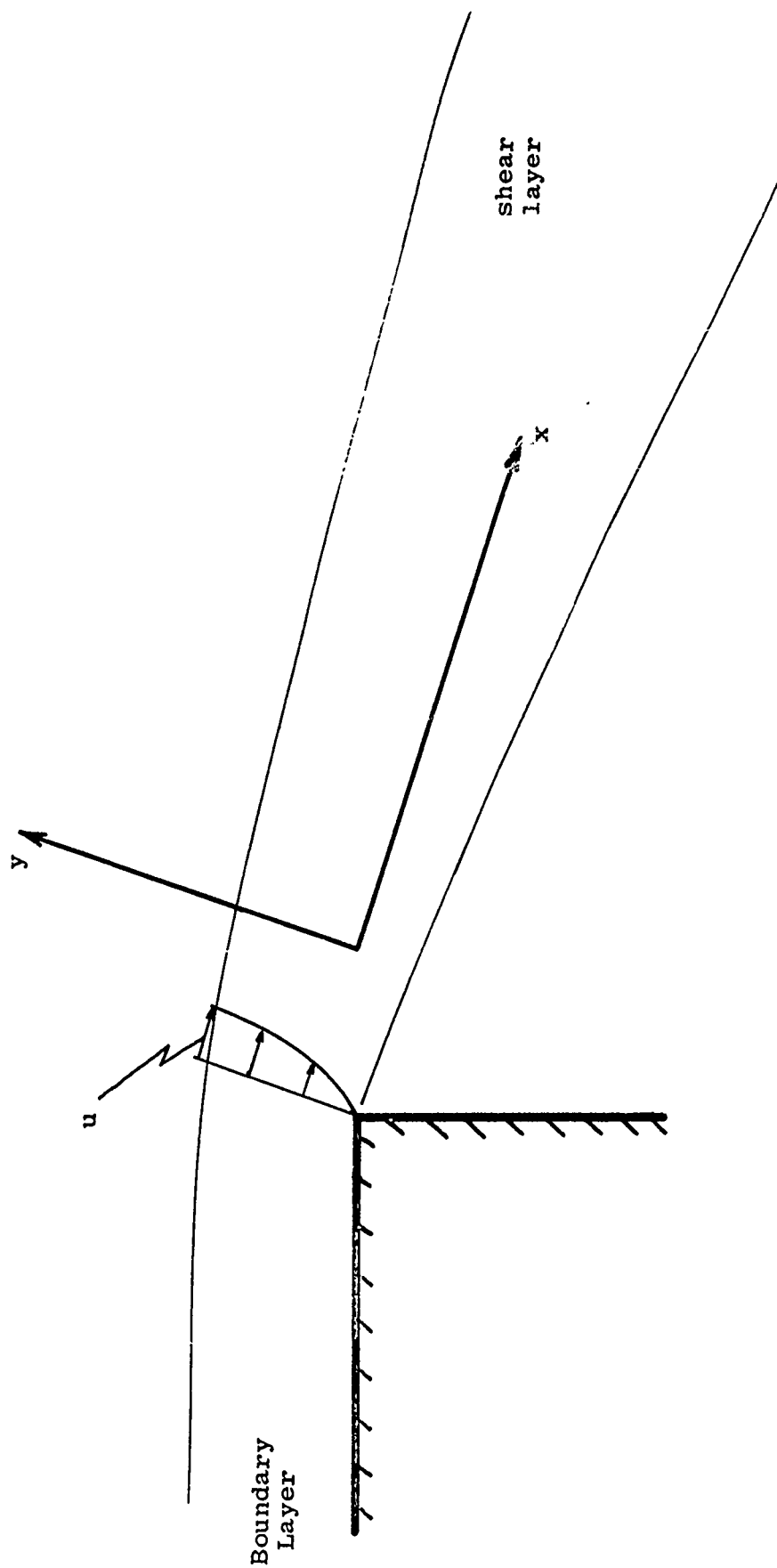


Figure 47. Coordinate System for Shear Layer Calculations.

where: $p_r = \frac{\mu C_p}{k}$ is the Prandlt Number.

Restricting attention to flows for which $p_r = 1$ and assuming variations of the specific heat at constant pressure are small, it follows that:

$$\rho C_p \frac{DT_o}{Dt} = \frac{\partial}{\partial y} \left(k \frac{\partial T_o}{\partial y} \right) \quad (45)$$

Introducing a Kirchhoff transformation with new dependent variable $\tau_o (T_o)$, i.e.:

$$\frac{d\tau_o}{dT_o} = \frac{k}{\mu} \quad (46)$$

Then, equation 45 becomes:

$$\rho C_p \frac{D\tau_o}{Dt} = \frac{k}{\mu} \frac{\partial}{\partial y} \left(\mu \frac{\partial \tau_o}{\partial y} \right)$$

or

$$\rho \frac{D\tau_o}{Dt} = \frac{\partial}{\partial y} \left(\mu \frac{\partial \tau_o}{\partial y} \right) \quad (47)$$

for unit Prandtl Number.

Note that for zero pressure gradient; the momentum equation reduces to:

$$\rho \frac{Du}{Dt} = \frac{\partial}{\partial y} \left(\mu \frac{\partial u}{\partial y} \right) \quad (42a)$$

so that:

$$\tau_o = A + B u \quad (48)$$

where A and B are constant. This result is only valid if $C_p = \text{const.}$, $P_r = 1$ and $\frac{dp}{dx} = 0$. In general, this result can only be applied to the asymptotic shear layer; since the initial velocity and temperature profiles will not be related in this way. In the developing shear layer it is necessary to specify both initial velocity and temperature profiles and solve the equations 45 and 42a separately. Since both equations are of the same form (assuming $P_r = 1$ in the energy equation), the solution for only one need be discussed.

1. APPROXIMATE SOLUTION OF THE EQUATION (42a)

For steady flow the equation reads:

$$\rho u \frac{\partial u}{\partial x} + \rho v \frac{\partial u}{\partial y} = \frac{\partial}{\partial y} \left(\mu \frac{\partial u}{\partial y} \right)$$

Introducing the new variables (after Stewartson [56]):

$$Y = \frac{1}{\sqrt{\gamma_\infty}} \int_0^y \frac{\rho}{\rho_\infty} dy \quad (49)$$

$$X = x$$

Then if the stream function ψ is given by:

$$\rho u = \rho_{\infty} \sqrt{\gamma_{\infty}} \frac{\partial \psi}{\partial y}$$

$$\rho v = -\rho_{\infty} \sqrt{\gamma_{\infty}} \frac{\partial \psi}{\partial x}$$

as suggested by the continuity equation, then it follows (with the additional assumption that the viscosity coefficient is proportional to the temperature) that:

$$\gamma \frac{\partial \gamma}{\partial X} - \frac{\partial \psi}{\partial X} \frac{\partial \gamma}{\partial Y} = \frac{\partial^2 \gamma}{\partial Y^2} \quad (50)$$

where:

$$\gamma = \frac{\partial \psi}{\partial Y}$$

Neglecting the second term in equation (50) (which is equivalent to the assumption $(\rho v \frac{\partial u}{\partial y}) / (\rho u \frac{\partial u}{\partial x}) \ll 1$) and replacing the coefficient ' γ ' in the first term by a constant mean value $\bar{\gamma}$, there results a diffusion equation:

$$\bar{\gamma} \frac{\partial \gamma}{\partial X} = \frac{\partial^2 \gamma}{\partial Y^2} \quad (51)$$

in the variables X, Y.

Equation (51) solves to give:

$$\mathfrak{I}(X, Y) = \frac{1}{\sqrt{\pi}} \int_{-\infty}^{\infty} \mathfrak{I}(0, \eta) \exp(-\beta^2) d\beta \quad (52)$$

where:

$$\eta = Y - 2\beta\sqrt{\frac{X}{\mathfrak{I}}}$$

In this study, \mathfrak{I} has been taken to be the value in the free stream, and the development of the profile is given in terms of the initial profile $\mathfrak{I}(0, y)$ and the distance downstream. In the case of a mild pressure gradient (so long as the assumption $\frac{v \frac{\partial u}{\partial y}}{u \frac{\partial u}{\partial x}} \ll 1$

is still tenable) the solution for \mathfrak{I} must satisfy the non-homogeneous diffusion equation:

$$\frac{\partial \mathfrak{I}}{\partial x} + F(x, y) = k \frac{\partial^2 \mathfrak{I}}{\partial y^2}$$

with appropriate boundary conditions.

2. INITIAL PROFILES

The initial profiles, $T_0(0, \eta)$ and $u(0, \eta)$, required in equation (12) for evaluating the development of the velocity and total temperature distributions were obtained as follows. It was assumed that the approaching boundary-

layer (in the X, Y plane) satisfies the conditions for Blasius flow. Hence, the velocity distribution satisfies:

$$f \frac{d^2 f}{d\eta^2} + 2 \frac{d^3 f}{d\eta^3} = 0$$

where: f is the Blasius stream function, and $\eta = y \sqrt{\frac{U_\infty}{\gamma_\infty X}}$.

The energy equation (3) then gives

$$\frac{d^2 T}{d\eta^2} + \frac{p_r}{2} f \frac{dT}{d\eta} = -p_r \frac{U_\infty^2}{C_p T_\infty} \left[\frac{d^2 f}{d\eta^2} \right]^2$$

for the non-dimensional static temperature. This equation solves to give:

$$T(\eta) = T_w + \int_0^\eta \left\{ \frac{1}{I(\eta)} \left(\frac{dT}{d\eta} \right)_w - \frac{U_\infty^2 p_r}{C_p T_\infty} \int_0^\eta \left[\frac{d^2 f(\xi)}{d\eta^2} \right]^2 I(\xi) d\xi \right\} d\eta \quad (53)$$

where:

$$I(\eta) = \exp \left[\frac{p_r}{2} \int_0^\eta f(\xi) d\xi \right]$$

T_∞ is the (dimensional) free-stream static temperature.

The initial profiles used in the present study are shown in Fig. (48) for the values $T_w = 2.058^*$ and zero

*This corresponds to an Eckert number, $E = U^2 / C_p T_\infty (T_w - 1)$, of 2.36.

heat flux to the wall, these being used as representative conditions. As noted in Chapter V, hot wire measurements were unattainable in the separation corner region due to wire breakage, and the experimental conditions for the initial profile cannot be modeled exactly. The initial profile was calculated for a Prandtl number of 0.72.

No allowance was made for the distortion of the profiles through the expansion process at the corner, nor was the presence of the lip shock considered. These approximations are justified as the present aim is only to study the shear layer development in a qualitative manner. The results should be evaluated in this context.

3. NUMERICAL RESULTS AND DISCUSSION

The initial velocity and temperature profiles used in the study are exhibited in Fig. (48). The static temperature gradient at the wall is zero since zero heat flux was assumed. For a tunnel total temperature of 560°R, this could be representative of conditions after the tunnel has been running for some time.

As suggested by the result shown in Fig. (49), the static temperature distribution changes very slowly along the shear-layer. It should be noted that this result is for laminar flow and if transition takes place in the shear layer the mixing rate would be somewhat higher. The transitional case has not been calculated due to lack of data concerning an acceptable shear stress model for such flows.

The same slow variation with distance along the shear layer is also a property of the velocity distribution

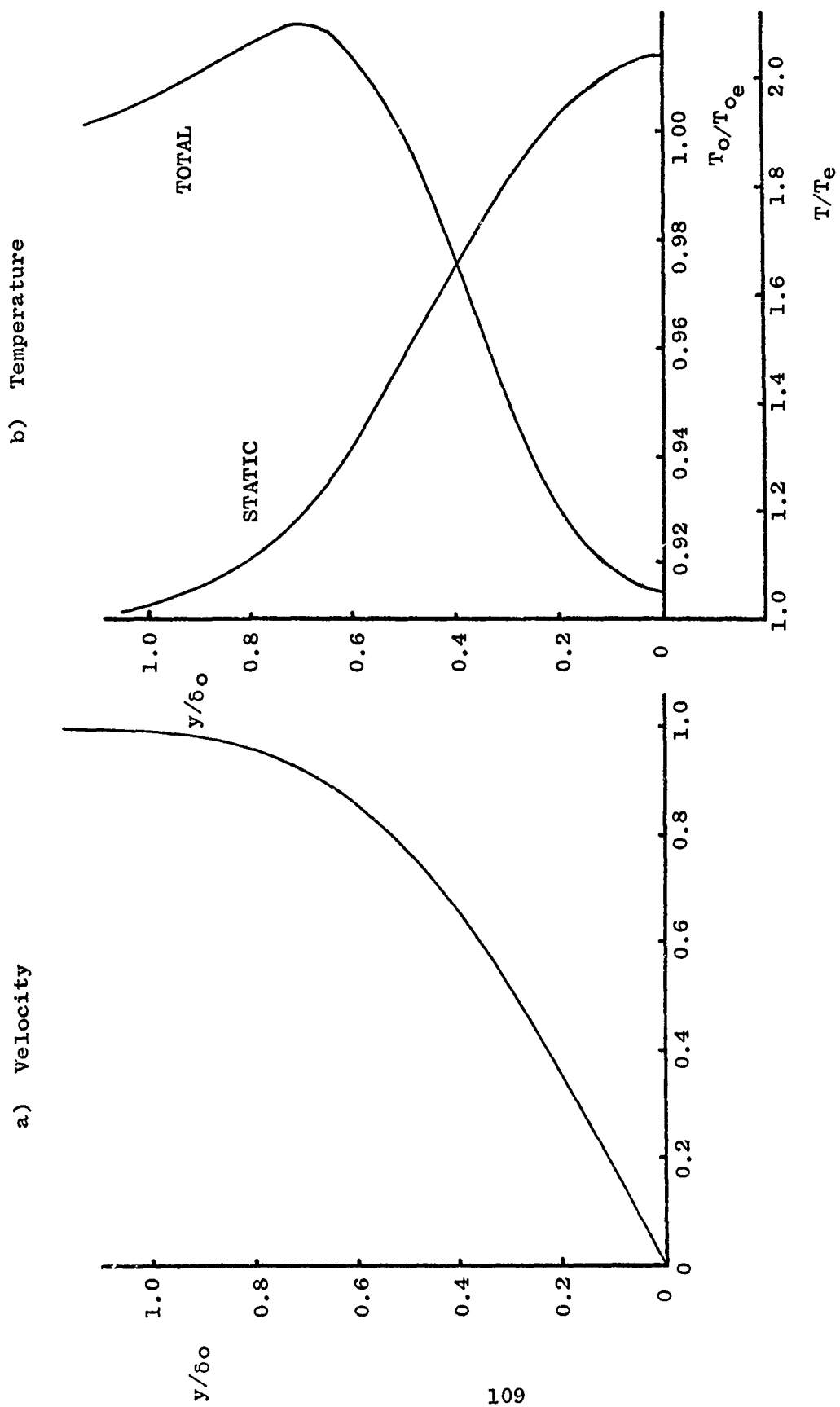


Fig. 48. Initial Profiles for shear layer calculations. Adiabatic wall conditions.
 $P_r = 0.72$.

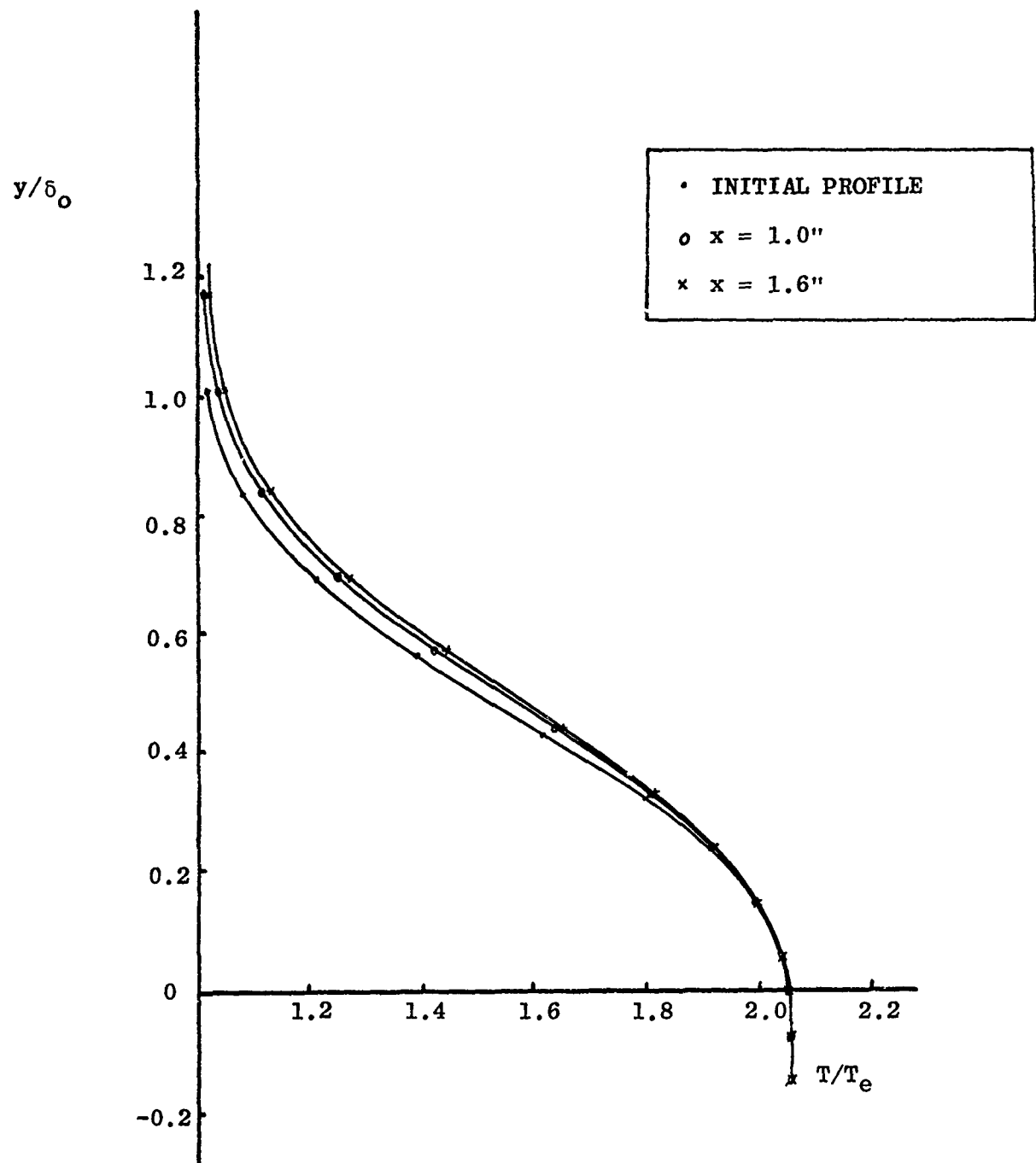


Fig. 49. Development of shear-layer static temperature distribution (Equation 52).

and hence of the total temperature distribution.

The shear layer total temperature distributions are shown in Fig. 50. The experimental data from Fig. 46 is also included on Fig. 50. The comparison shown here should be treated with some caution since the exact location of the dividing streamline is not known in the experimental case. In Fig. 50, the dividing streamline location indicated in Fig. 46 was used. Since it is to be expected that the initial profile has its minimum total temperature at the wall (i.e. in the absence of extreme heat transfer rates from the wall), and as the (albeit simple) theory just presented indicates very small rates of change of temperature along the shear layer, it can be expected that the dividing streamline lies close to the minimum total temperature condition. While it is true that the theory has neglected the flow in the cavity, with its associated heat transfers, there seems to be no evidence suggesting that large temperature gradients along the shear layer will exist for laminar flow. For this reason, it is felt that the comparison shown in Fig. 50 is qualitatively correct.

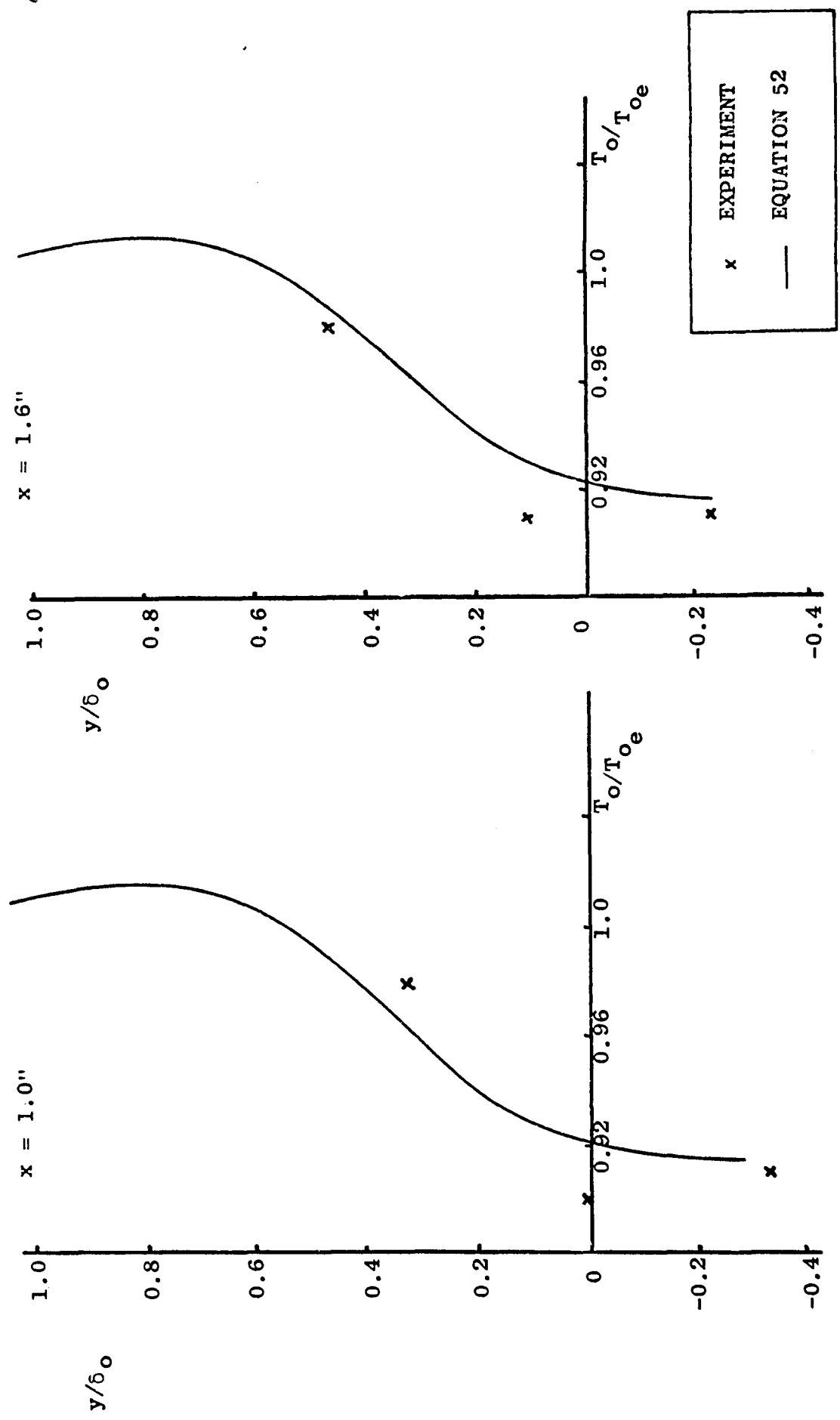


Fig. 50. Comparison with experimental data (from Fig. 46)
 (Tentative only since origin is unknown for the
 experimental data).

CHAPTER X

THE WAKE SHOCK

The separated flow region is closed by the reattachment of the flow to the downstream surface. Since this reattachment process involves a compressive turning of the flow into the free-stream direction, a shock wave (the wake shock) is generated at reattachment. The strength and inclination of this shock wave is dependent upon its upstream conditions and the extent of the turning that is required. One characteristic of a supersonic base flow is that the length of the free shear layer decreases as the unit Reynolds number increases.* Hence, it follows that the Mach number along the shear layer (M_{shear}) will increase with increasing Reynolds number - and the flow conditions ahead of the wake shock are dependent upon the Reynolds number.

Experimental data [26] has indicated a very slight sensitivity of the wake shock angle to changes in Reynolds number, which would appear contradictory to the above remarks. The summarized experimental data [26] is shown in Fig. 51 for a Reynolds number range of $0.5 - 2.0 \times 10^6$.

In this chapter a simple flow model is put forward which demonstrates - in regions where the viscous forces are not significant - the pertinent features of such base flows. It is of interest to know both the reattachment

*or, equivalently, the free stream static pressure for constant total temperature.

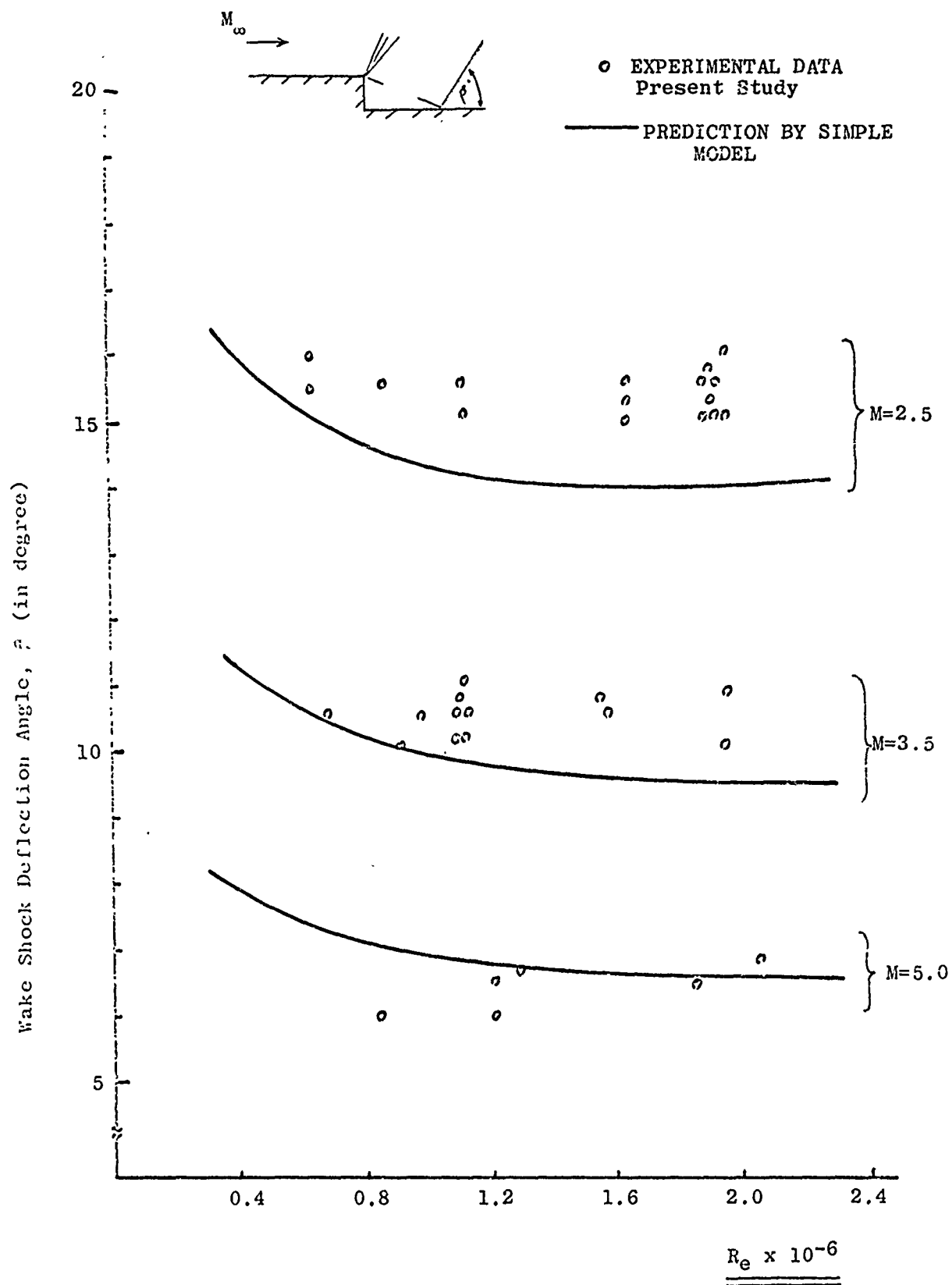


Fig. 51. Wake Shock Data.

point location and the wake shock inclination so that the associated heat transfer rates and the far field shock interaction phenomena can be designed for.

2. FLOW MODEL

The development of the flow model is the following. Firstly, the complex flow in the vicinity of the corner (see Refs. 42, 48) is replaced by an equivalent simple expansion process. The magnitude of this expansion being such as to expand the flow to the experimentally determined base pressure. In the present work, the base pressure was determined from the empirical correlation presented by Su and Wu [46] and is outlined in Chapter VI. Such a simple flow-model omits the details of the viscous transonic flow close to the corner and also ignores the presence of the lip shock (which is, of course, a product of the corner flow).

The comparison data shown in Fig. 52 indicates, however, that the flow model predicts adequately the turning angle and hence the length of the shear layer. This is important since the peak heat transfer rate occurs just downstream of the reattachment point [25] and so its location can be predicted. The flow properties ahead of the wake-shock are then known.

Conitions downstream of the wake shock can be specified in one of two ways; either in terms of the overall pressure ratio, or as a function of the downstream flow direction.

In either case, the downstream condition is not known, and some empirical data must be used. Herein it has been assumed that the flow is directed along the wall downstream of the wake shock.

3. DISCUSSIONS

The flow model can now be discussed to determine the reason for the apparent invariance of the wake-shock angle with change of Reynolds number*, over the range $0.5 - 2.0 \times 10^6$ of the latter variable. Fig. 53 indicates that the rate of change of base pressure decreases with increase of Reynolds number over the Reynolds number range of interest, and this base pressure variation produces the resultant shear layer Mach number (M_{shear}) shown in Fig. 53. The variation of the shear layer inclination was implied in Fig. 52. It is clear from Figs. 52 and 53 that the rate of change of upstream wake-shock variables is still too rapid to account for the constancy of the wake-shock inclination (Fig. 51), and some additional phenomenon must preside.

It is noted that the inclination of the shock-wave to the free-stream direction has two components. One of these is the inclination of the shock-wave to the shock-upstream flow direction (θ), the other is the inclination of the shear layer to the free stream direction (ν). The notation

*Reynolds number (Re) is based on length to the corner.

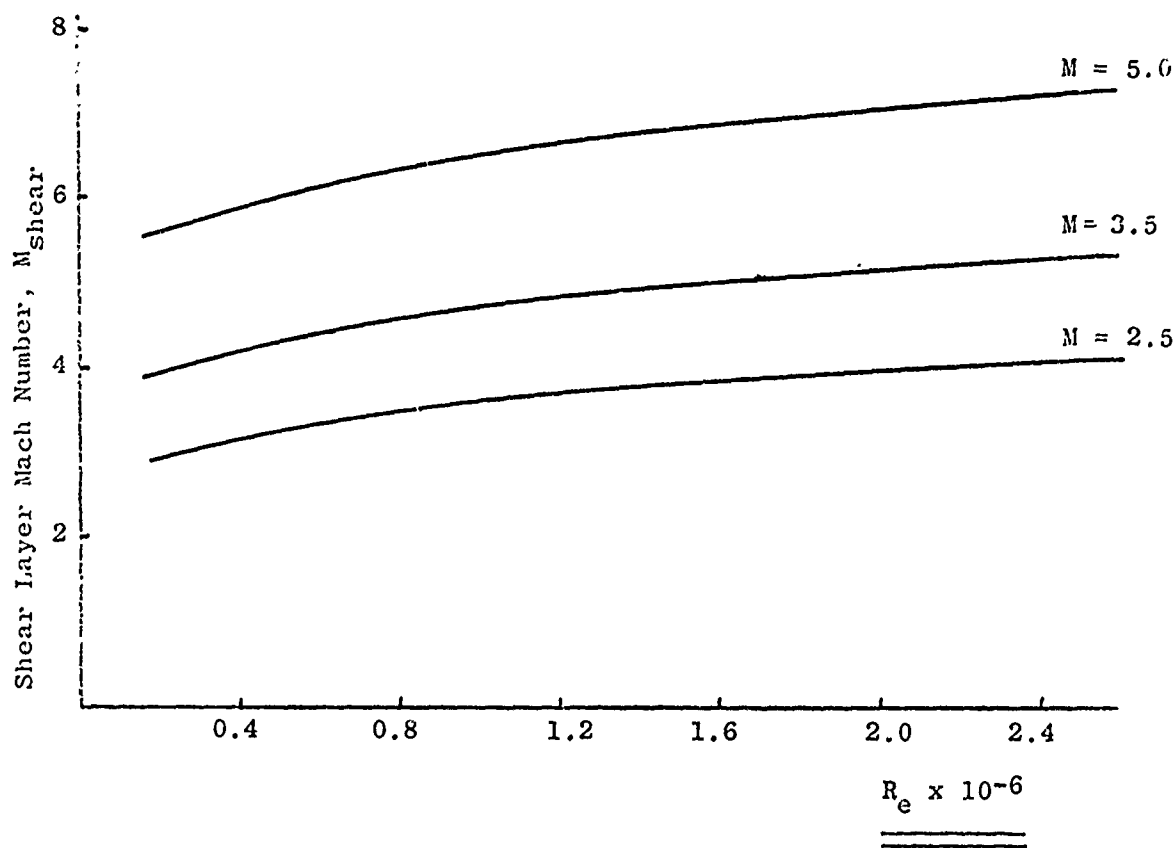
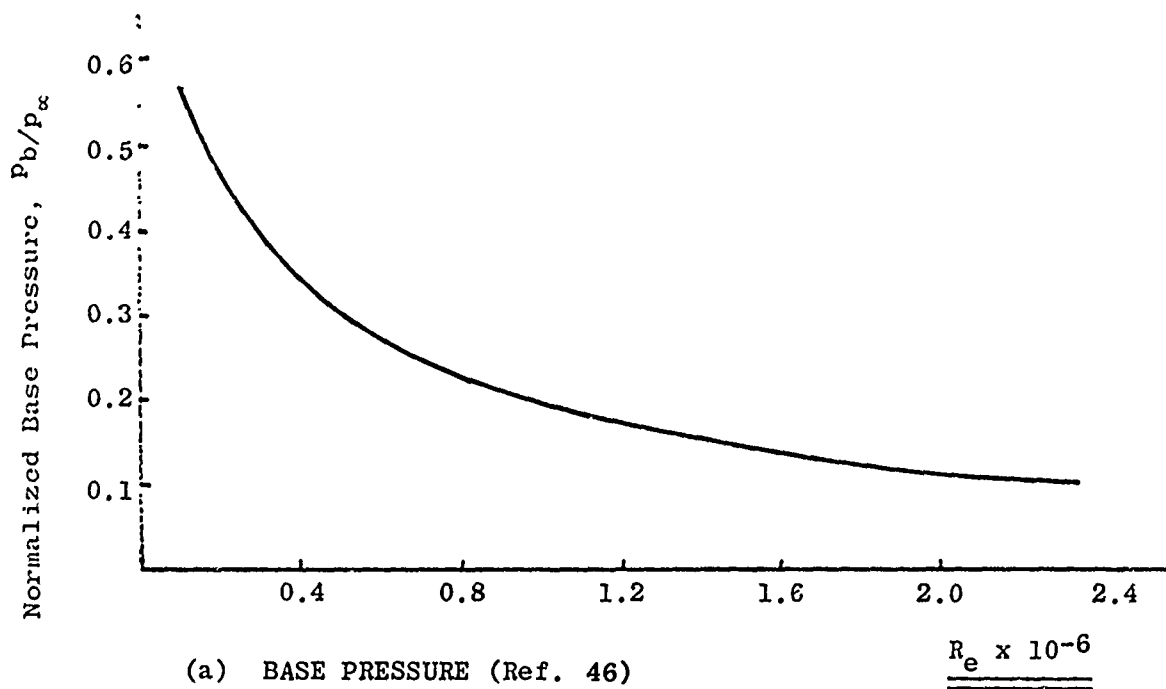


Fig. 53. Properties of the flow model.

is shown in Fig. 54 . A plot of θ vs v from the flow model is presented in Fig. 54, and this clearly shows that in the Reynolds number range of interest, the rates of change of both θ and v are almost identical. They are identical on the lines marked β constant - which the model approaches at the higher Reynolds numbers. Thus, it is suggested that the constancy of the wake-shock inclination results from the fact that, for a certain Reynolds number range, the rate at which the wake shock rotates with respect to its upstream direction is almost the same as that at which the upstream flow is rotating with respect to the free stream direction. This contingency is the result of both the form of the base pressure variation shown in Fig. 53 and of the oblique shock-wave surface geometry.

The results can be extended to other configurations (e.g. wedge type flows discussed in Ref. 8) if an appropriate base pressure relation is introduced.

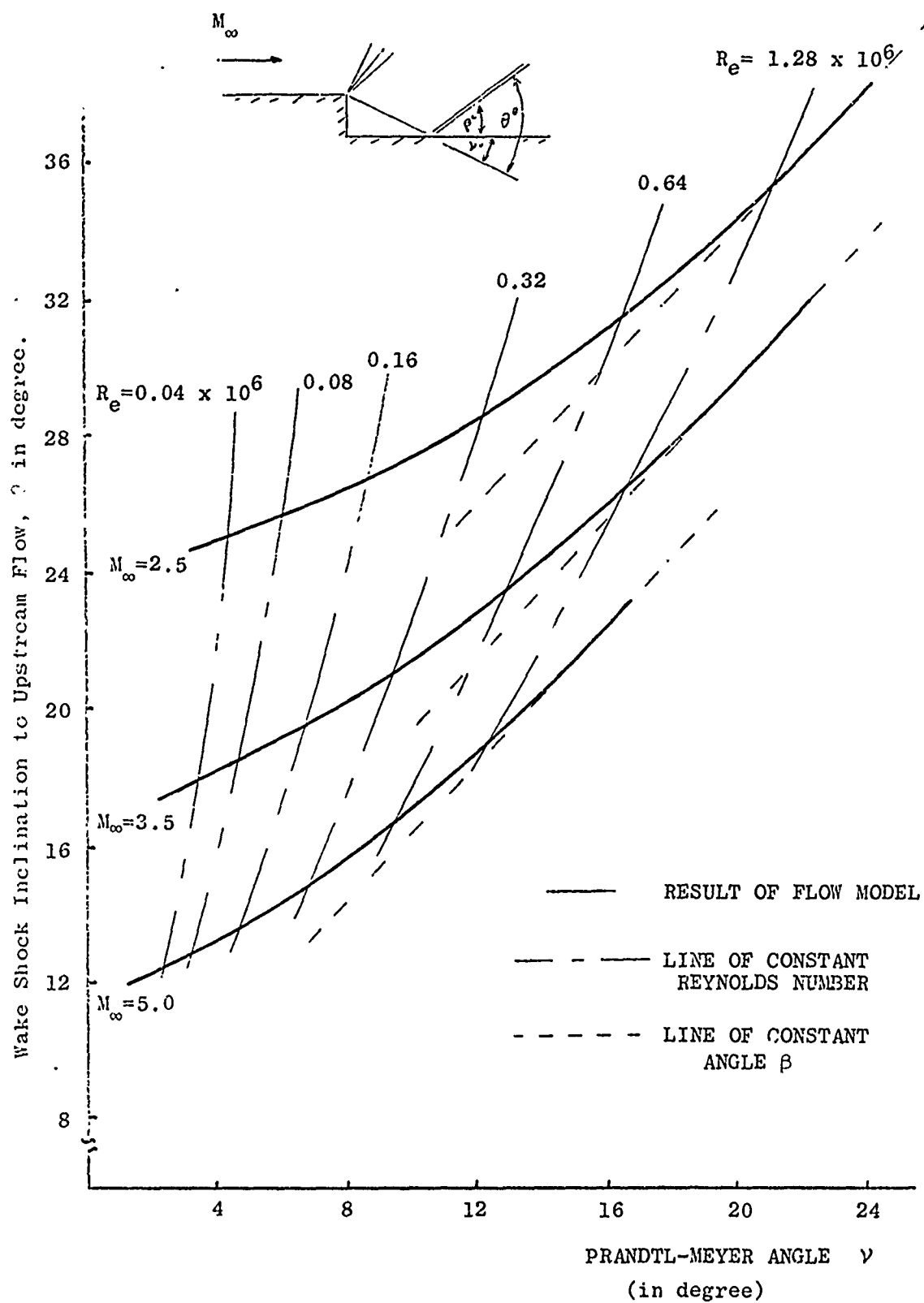


Fig. 54. Calculated wake shock orientation.

CHAPTER XI

CONCLUSIONS AND RECOMMENDATIONS

A detailed flow study has been conducted in the regions upstream and downstream from the separation corner of a rearward facing step at supersonic speeds. The important results and conclusions of this study are presented below.

A more direct, accurate and simple hot-wire data reduction method was developed. The convective heat transfer rate and the adiabatic wire temperature were directly determined from the measurements without introducing the end loss correction factors. This method makes possible successful hot-wire measurements in the free shear layer, and in the low Reynolds number, subsonic, recirculating flow.

The experimental information concerning the upstream influence of the lower base pressure is presented. A significant fraction of the surface pressure drop occurs immediately upstream of the separation corner. The magnitude of the upstream influence is a function of the thickness of the undisturbed boundary layer. Correlation of the measured surface pressure with the undisturbed boundary layer thickness indicates that the effect of the lower base pressure is propagated upstream to a distance of about five boundary layer thicknesses ahead of the corner and

that the sonic line is very close to the wall at the separation corner.

By a simple order of magnitude analysis, one finds that the acceleration and expansion of the major portion of the oncoming boundary layer over the step may be approximated as an inviscid process. An isentropic streamtube analysis of the measured pitot profiles in the approaching boundary layer shows that considerable acceleration takes place in the lower half portion of the approaching boundary layer; and that the normal and axial pressure gradients near the corner are of about the same magnitude. The static pressure variation in the supersonic portion of the boundary layer is roughly linear.

The measured pitot profiles of the initial free shear layer indicate that the rapid corner expansion cannot be described by the Prandtl-Meyer theory, when the boundary layer at separation is of finite thickness. It also indicates that the oncoming boundary layer has a significant effect in the development of the free shear layer. The interaction of the lip shock with the free shear layer may be more important at higher free stream Mach number and low Reynolds number.

Comparison of measured pitot profiles with the numerical results from the method of rotational characteristics appears to indicate that the inviscid rotational theory is adequate for predicting the expansion of the supersonic

boundary-layer at the separation corner; and also the lip shock formation. It was found that the pitot pressure probe was not sensitive enough to detect the origin of the lip shock. The actual location of the lip shock, and its region of formation, are a function of the Reynolds number and free-stream Mach number. In some instances the lip shock may form some distance downstream of the separation corner.

It was found that the parameter $Re_{\infty, H}^{0.9} (L/H)^{0.1}$ was satisfactory for correlating the base pressure when the shear layer flow was either laminar or transitional. The limited amount of testing carried out on the step with overhang was inclusive, but appears to indicate that the overhang has little effect. Further study should be carried out in this area.

Theoretical studies on the temperature distribution in the shear layer indicate that the detailed temperature distribution in the shear layer is most strongly influenced by the initial profile; the effects of mixing in the layer being small.

The basic features of the recirculating region are illustrated in terms of Mach number and total temperature mappings. The dividing streamline and minimum velocity lines are identified. The total temperature of the recirculating region may be as low as 0.8 of the free stream total temperature, while the Mach number in the recirculating flow may be as high as 0.8.

A simple model of the inviscid flow was put forward to study the observed fact that the wake shock angle was only a weak function of Reynolds number. It was shown that the model was quantitatively correct over the Reynolds number range of the test, but indicated a larger variation of wake shock angle outside this range.

Based on this study, the following recommendations are presented.

The newly developed hot-wire method is ideal for measuring h and T_{aw} in the flow field when the end loss corrections are required. This technique is recommended to check the existing heat transfer correlation formula and if necessary, to provide new heat transfer data.

A heat transfer correlation formula is needed for low Reynolds number and very low subsonic flow ($Re_0 < 0.20$, $M < 0.3$). Experimental information concerning natural convection in this range is also needed.

It is desirable to verify the estimation of turbulent effects on measured hot-wire resistance and to measure accurately the turbulent intensity in the free shear layer and the recirculating flow. Hot-wire measurements in the recirculating region with laminar free shear layer are needed for comparison with theoretical results.

Many free shear layer profiles are presented at different Mach numbers, Reynolds numbers and step heights. Sufficient experimental information is provided for theoretically analyzing the problems related to the free shear layer growth.

Both theoretical analysis and accurate and detailed measurements are needed to study the acceleration and expansion of the subsonic portion of the oncoming boundary layer, which hopefully will completely define the initial conditions of the mixing region.

At higher free stream Mach number, the shear layer is expanding and mixing with the recirculating flow; and the effects of pressure gradients on the mixing process deserve attention.

A comparison of the hot-wire results with numerical calculations of mixed supersonic/subsonic type flow in the near wake [17] may be helpful for interpretation of the hot-wire measurements. The successful numerical solution of the compressible Navier-Stokes equation is very difficult, however, successful measurements in part of the near wake (such as separation region and reattachment region) are also very difficult. One should not rule out the potential of the numerical method in solving the near wake.

The upstream influence was studied by Weiss and Nelson [5] with no static pressure gradient in the accelerating boundary layer. It may be interesting to follow their approach but with linear static pressure distribution in the supersonic portion of the boundary layer.

BIBLIOGRAPHY

1. Lees, L. "Hypersonic Wakes and Trails," AIAA Journal, 2:417-428, March, 1964.
2. Lykoudis, P. "A Review of Hypersonic Wake Studies," AIAA Journal, 4:577-590, April, 1966.
3. Chapman, D. R., D. M. Kuehn, and H. K. Larson. "Investigation of Separated Flows in Supersonic and Subsonic Streams with Emphasis on the Effect of Transition," National Advisory Committee for Aeronautics Report No. 1356, Washington, D. C., June, 1958.
4. Crocco, L., and L. Lees. "A Mixing Theory for the Interaction between Dissipative Flows and Nearly Isentropic Streams," Journal of the Aerospace Science, 19:649-676, October, 1952.
5. Baum, E. "An Interacting Model of a Supersonic Laminar Boundary Layer near a Sharp Backward Facing Step," TRW Systems Report No. 0-7854-6019-R000, Redondo Beach, California, December, 1966.
6. Olsson, G. R., and A. F. Messiter. "The Hypersonic Boundary Layer Approaching the Base of a Slender Body." AIAA Paper No. 68-67, presented at AIAA 6th Aerospace Sciences Meeting, New York, New York, January, 1968.
7. Weiss, R. F., and W. Nelson. "On the Upstream Influence of the Base Pressures," Avco-Everett Research Laboratory Research Report 67-264, Everett, Massachusetts, January, 1967.
8. Hama, F. R. "Experimental Investigations of Wedge Base Pressure and Lip Shock," Jet Propulsion Laboratory TR-32-1033, California Institute of Technology, Pasadena, California, December, 1966.
9. Weiss, R., and S. Weinbaum. "Hypersonic Boundary Layer Separation and the Base Flow Problem," AIAA Journal, 4:1321-1330, August, 1966.
10. Adamson, T. C. "Solution for Supersonic Rotational Flow around a Corner Using a New Coordinate System," Journal of Fluid Mechanics, 34:735-758, December, 1968.

11. Zakky, V. "Heat Transfer at a Corner," Journal of the Aerospace Science, 27:157-158, February, 1960.
12. Batchelor, G. K. "On Steady Laminar Flow with Closed Streamlines at Large Reynolds Numbers," Journal of Fluid Mechanics, 1:177-190, July, 1956.
13. Burggraf, O. R. "Analytical and Numerical Studies of the Structure of Steady Separated Flow," Journal of Fluid Mechanics, 24:113-151, January, 1966.
14. Weiss, R. F. "A New Theoretical Solution of the Laminar Hypersonic Near Wake," AIAA Journal, 5:2142-2149, December, 1967.
15. Scherberg, M. G. "Wake Recirculations Generated by Flows ($M > 1$) over Rearward Facing Steps," Aerospace Research Laboratory Report 69-0103, Wright-Patterson Air Force Base, Ohio, July, 1969.
16. Roache, P. J., and T. J. Mueller. "Numerical Solution of Compressible and Incompressible Laminar Separated Flows." AIAA Paper No. 68-741, presented at AIAA Fluid and Plasma Dynamics Conference, Los Angeles, California, June, 1968.
17. Erdos, J., and V. Zakky. "Numerical Solution of Several Steady Wake Flows of the Mixed Supersonic/Subsonic Type by a Time Dependent Method and Comparison with Experimental Data." AIAA Paper No. 69-649, presented at AIAA Second Fluid and Plasma Dynamics Conference, San Francisco, California, June, 1969.
18. Scherberg, M. G., and H. E. Smith. "An Experimental Study of Supersonic Flow over a Rearward Facing Step," AIAA Journal, 5:51-56, January, 1967.
19. Batt, R. G., and T. Kubata. "Experimental Investigation of Laminar Near Wakes behind 20° Wedges at $M = 6$," AIAA Journal, 6:2077-2083, November, 1968.
20. Roshko, A., and G. J. Thomke. "Effect of a Shoulder Modification on Turbulent Supersonic Base Flow," AIAA Journal, 5:827-829, April, 1967.
21. Lewis, J. E., and W. Behrens. "Fluctuation Measurements in the Near Wake of a Slender Wedge at Mach 4.0 with and without Base Injection," TRW Systems Report No. 0-6388-6030-R000, Redondo Beach, California, February, 1968.

22. Todisco, A., and A. J. Pallone. "Near Wake Flow Field Measurements." AIAA Paper No. 65-53, presented at AIAA Second Aerospace Sciences Meeting, New York, New York, January, 1965.
23. Rom, J., Y. Kronzon, and A. Seginer. "The Velocity, Pressure and Temperature Distributions in the Turbulent Supersonic Near Wake behind a Two-Dimensional Wedge Flat Plate Model," TAE Report No. 80, Department of Aeronautical Engineering, Technion-Israel Institute of Technology, Haifa, Israel, September, 1968.
24. Charwat, A. F., and J. K. Yakura. "An Investigation of Two-Dimensional Supersonic Base Pressures," Journal of the Aerospace Science, 25:122-128, February, 1958.
25. Smith, H. E. "The Flow Field and Heat Transfer Downstream of a Rearward Facing Step in Supersonic Flow," Aerospace Research Laboratory Report No. 67-0056, Wright-Patterson Air Force Base, Ohio, March, 1967.
26. Wu, J. M., M. W. Su, and M. G. Scherberg. "Experimental Investigation of Supersonic Flow Separation over a Rearward Facing Step." AIAA Paper No. 70-106, presented at AIAA Eighth Aerospace Sciences Meeting, New York, New York, January, 1970.
27. Test Facilities Handbook. Fifth edition. Vol. 4. Arnold Air Force Station, Tennessee: Arnold Engineering Development Center, 1963.
28. Donaldson, J. C. "An Experimental Study of the Region of Separated Flow Downstream of a 0.75-in. Rearward Facing Step at Mach Numbers 2.5, 3.5, and 5," Arnold Engineering Development Center TR-69-141, Arnold Air Force Station, Tennessee, July, 1969.
29. Donaldson, J. C., and A. W. Myers. "Investigation of the Separation and Reattachment of Flow Downstream of a Two-Dimensional, Rearward-Facing Step at Mach Numbers 2.5 and 3.5," Arnold Engineering Development Center TR-65-223, Arnold Air Force Station, Tennessee, November, 1965.

30. Donaldson, J. C., and A. W. Myers. "Investigation of the Separation and Reattachment of Flow Downstream of Two-Dimensional Rearward-Facing Steps at Mach Numbers 2.5, 3.5 and 5," Arnold Engineering Development Center TR-66-106, Arnold Air Force Station, Tennessee, May, 1966.
31. Dewey, C. F., Jr. "Hot-Wire Measurements in Low Reynolds Number Hypersonic Flows," Hypersonic Research Project Memo. No. 63, Guggenheim Aeronautical Laboratory, California Institute of Technology, Pasadena, California, September, 1961.
32. King, L. V. "On the Convection of Heat from Small Cylinders in a Stream of Fluid," Proceedings of the Philosophical Transactions of the Royal Society of London, 214 (Series A):373-432, December, 1914.
33. Grant, H. P., and R. E. Kronauer. "Fundamentals of Hot-Wire Anemometry," ASME Symposium on Measurement in Unsteady Flow, 44-53, May, 1962.
34. Dewey, C. F., Jr. "A Correlation of Convective Heat Transfer and Recovery Temperature Data for Cylinders in Compressible Flow," International Journal of Heat and Mass Transfer, 8:245-252, February, 1965.
35. Herzog, R. T. "Nitrogen Injection into the Base Region of a Hypersonic Wake," Hypersonic Research Project Memo. No. 71, Guggenheim Aeronautical Laboratory, California Institute of Technology, Pasadena, California, August, 1964.
36. Shahrokhi, F. (editor). AIAA Tennessee Section Week-End Work Shop Manual in Applied Measuring Techniques. Tullahoma, Tennessee: The University of Tennessee Space Institute, 1969.
37. Vrebalovich, T. "Heat Loss from Hot-Wires in Transonic Flow," Jet Propulsion Laboratory Research Summary No. 36-14, California Institute of Technology, Pasadena, California, May, 1962.
38. Kendall, J. M., Jr. "Experimental Investigation of Leading Edge Shock Wave-Boundary Layer Interaction at Hypersonic Speeds," Hypersonic Research Project Memo. No. 30, Guggenheim Aeronautical Laboratory, California Institute of Technology, Pasadena, California, January, 1956.

39. Bradfield, W. S., D. G. DeCoursin, and C. B. Blumez. "The Effect of Leading Edge Bluntness on a Laminar Supersonic Boundary Layer," Journal of the Aerospace Science, 21:373-389, June, 1954.
40. Morkovin, M. V., and W. S. Bradfield. "Probe Interference Measurements in Supersonic Laminar Boundary Layers," Journal of the Aerospace Science, 21:785-787, November, 1954.
41. AMES Research Staff. "Equations, Tables, and Charts for Compressible Flow," National Advisory Committee for Aeronautics Report No. 1135, Washington, D.C., June, 1953.
42. Weinbaum, S. "Rapid Expansion of Supersonic Boundary Layer and Its Application to the Near Wake," AIAA Journal, 4:217-226, February, 1966.
43. Rubin, D. V. "A transonic Investigation of Jet Plume Effects on Base and After Body Pressures of Boattail and Flare Bodies of Revolution," U. S. Army Missile Command Report No. RD-TR-70-10, Oct. 1970.
44. Matz, R. Private Communication, RTF, ARO, Inc., Arnold Engineering Development Center, Tullahoma, Tennessee, November 1969.
45. Su, M. W. "Investigation of Supersonic Flow Over a Rearward Facing Step". Ph.D. Thesis, The University of Tennessee, June 1970.
46. Su, M. W. and J. M. Wu. "Base Pressure Correlation in Supersonic Flow", AIAA J. Vol. 9, p. 1429, 1971.
47. Rom, J. "Supersonic flow over Two-Dimensional and Axially Symmetric Backward Facing Steps", TEA Report 33, March 1964.
48. Adamson, T. C. and B. D. Fishburn. "Transonic Rotational Flow Around a Convex Corner with Application to a Supersonic Boundary-Layer", J. de Mecanique, Vol. 10, p. 205, 1971.
49. Scherberg, M. G., private communication, ARL Wright-Patterson AFB, Ohio, 1971.
50. Chapman, D. R. "An Analysis of Base Pressure at Supersonic Velocities and Comparison with Experiment," National Advisory Committee for Aeronautics TN-2137, Washington, D. C., June 1951.

51. Alber, I. E. and L. Lees. "Integral Theory for Supersonic Turbulent Base Flows," AIAA Journal, 6:1343-1351, July, 1968.
52. Behrens, W. "Flow Field and Stability of the Far Wake behind Cylinders at Hypersonic Speeds." Ph.D. dissertation, California Institute of Technology, Pasadena, California, 1966.
53. Hinze, O. J. Turbulence. New York: McGraw-Hill Book Company, Inc., 1959.
54. Bauer, R. C. Private Communication. Arnold Engineering Development Center, Arnold Air Force Station, Tennessee, August, 1969.
55. Nash, J. F., V. G. Quincy and J. Callinan. "Experiments on Two-Dimensional Base Flow at Subsonic and Transonic Speeds", NPL Aero. Report 1070 January 1963.
56. Stewartson, K. "Correlated Incompressible and Compressible Boundary-Layers", Proc. Roy. Soc., Vol. 200, p. 84, 1949.
57. Donaldson, I. S. "On the Separation of a Supersonic Flow at a Sharp Corner", AIAA J., Vol. 5, p.1086, 1967.
58. Brailovskaya, I. Yu. "Flow in the Near Wake", Soviet Physics - Doklady, Vol. 16, p-197, Sept. 1971.
59. Rom, J. "Near Wake Flow Studies is Supersonic Flow", TAE Report 38, Technion Research and Development Foundation, Haifa, Israel, March 1965.

APPENDIX A

REVIEW ON HOT-WIRE MEASUREMENTS IN LOW REYNOLDS NUMBER HYPERSONIC FLOWS

The technique of hot-wire measurements in low Reynolds number hypersonic flows was originally developed by Dewey [31]. The technique is described as follows.

The convective heat transfer from length l of a heated wire of infinite length to the surrounding fluid is

$$I_m^2 R^* = h\pi dl(T^* - T_{aw}) \quad (A-1)$$

where superscript $*$ refers to infinitely long wire and all the assumptions made in Chapter III, Section 2 are retained. The term "infinite wire" refers to a wire of sufficient length that end loss is not important. It should be emphasized that both h and T_{aw} are assumed to be independent of the wire length.

From Equation (A-1), the convective heat transfer coefficient is

$$h = \frac{I_m^2 R^*}{\pi dl(T^* - T_{aw})} \quad (A-2)$$

For a finite wire, the measured convective heat transfer coefficient is defined as

$$I_m^2 R_m = h_m \pi d \ell (T_m - T_{aw_m})$$

or

$$h_m = \frac{I_m^2 R_m}{\pi d \ell (T_m - T_{aw_m})} \quad (A-3)$$

where the subscript m denotes quantities measured by a finite wire, and the heat transfer includes both convection and conduction. In order to correct h_m to the value h for an infinitely long wire, one introduces the ratio of these two quantities at a given current. This ratio is defined as the Nusselt number correction factor

$$\psi_N = \frac{h}{h_m} = \frac{Nu_o}{Nu_m} = \frac{R^*}{R_m} \frac{T_m - T_{aw_m}}{T^* - T_{aw}} \quad (A-4)$$

Similarly the correction factor for the recovery factor is defined as

$$\psi_R = \frac{T_{aw}}{T_{aw_m}} = \frac{\eta^*}{\eta_m} \quad (A-5)$$

ψ_N and ψ_R are derived from the measurements with a finite wire in the following way.

From Equation (11), the measured wire temperature is

$$T_m = \frac{2}{\ell} \int_0^{\ell/2} T \, dx = \frac{n}{m^2} - \frac{[(n/m^2) - T_s]}{m\ell/2} \tanh \frac{m\ell}{2} \quad (A-6)$$

where

$$\frac{m\ell}{2} = \left(\frac{hd}{k_w} - \frac{b I_m^2}{\pi \ell k_w} \right)^{0.5} \frac{\ell}{d}$$

for an infinitely long wire,

$$\frac{\ell}{d} \rightarrow \infty$$

$$\left(\tanh \frac{m\ell}{2} \right) / (m\ell/2) \rightarrow 0$$

and

$$T^* = \lim_{\ell/d \rightarrow \infty} T_m = \frac{n}{m^2} \quad (A-7)$$

$$R^* = a + \frac{bn}{m^2} \quad (A-8)$$

Substituting Equations (A-7) and (A-8) into Equation (A-4), one obtains

$$\psi_N = \left[\frac{a + (bn/m^2)}{R_m} \right] \left[\frac{T_m - T_{awm}}{(n/m^2) - T_{aw}} \right] \quad (A-9)$$

After a lengthy expansion and neglecting the higher order terms with some approximations, Dewey finally obtained

$$\psi_N = \psi_N(S) = \psi_N(Nu_O) \quad (A-10)$$

since

$$S = \frac{\ell}{d} \left(\frac{hd}{k_w} \right)^{0.5} = \frac{\ell}{d} (Nu_O \frac{k_O}{k_w})^{0.5}$$

Substituting Equation (A-7) into Equation (A-6),
one obtains

$$T_m = T^* \left[1 - \frac{\tanh (m\ell/2)}{(m\ell/2)} \right] + T_s \left[\frac{\tanh (m\ell/2)}{(m\ell/2)} \right] \quad (A-11)$$

and

$$T_{aw_m} = \lim_{I \rightarrow 0} T_m = T_{aw} \left(1 - \frac{\tanh S}{S} \right) + T_s \left(\frac{\tanh S}{S} \right) \quad (A-12)$$

where

$$T_{aw} = \lim_{I \rightarrow 0} T^*$$

Rearranging Equation (A-12), one gets

$$\psi_R = \frac{T_{aw}}{T_{aw_m}} = \frac{1 - (T_s/T_{aw_m}) (\tanh S/S)}{[1 - (\tanh S/S)]} \quad (A-13)$$

or

$$\psi_R = \psi_R(S) = \psi_R(Nu_O) \quad (A-14)$$

Then, Equation (A-10) and (A-14), and the correlation formula for heat transfer and recovery factor were coupled together to determine the flow field parameters, i.e.,

$$T_{aw}(M, Kn) = T_{aw_m} \psi_N(Re_O)$$

$$Nu_O(M, Re_O) = Nu_m \psi_R(Re_O)$$

The method of successive substitution was used to solve the above system of equations and convergence of the solution was not obtained when $M < 1.5$.

At higher Mach number ($M > 2$), the correlation formula for T_{aw} and h becomes more simple. Behrens [52] used the following two equations for the data reduction of his hot-wire measurements

$$Re_O = 5.26 Nu_O + 5.74 Nu_O^2$$

$$\frac{T_{aw}}{T_O} = 1.167 - \frac{0.217}{1 + [1/(0.335 Re_O)^{1.33}]}$$

APPENDIX B

SOLUTION FOR h AND T_{aw}

Equations (13) and (14) are solved for h and T_{aw} by a Newton-Raphson iteration scheme.² The details are described as follows. Equations (13) and (14) can be rearranged as

$$F(h, T_{aw}) = (a + b T_{aw}) - \frac{b(T_{aw} - T_s) \tanh S}{S} - R_m \Big|_{I \rightarrow 0} \quad (B-1)$$

$$G(h, T_{aw}) = b \left(\frac{a + b T_{aw}}{\pi d l h} \right) \left(1 - \frac{\tanh S}{S} \right) + \frac{b^2 (T_{aw} - T_s)}{2S} \left(\frac{\operatorname{sech}^2 S}{\pi d \sqrt{h} k_w} - \frac{\tanh S}{\pi d l h} \right) - \frac{dR_m}{dI_m^2} \Big|_{I \rightarrow 0} \quad (B-2)$$

The partial derivatives of F and G with respect to h and T_{aw} are

$$\frac{\partial F}{\partial h} = -b(T_{aw} - T_s) \left(\frac{S \operatorname{sech}^2 S - \tanh S}{2h S} \right) \quad (B-3)$$

$$\frac{\partial F}{\partial T_{aw}} = b \left(1 - \frac{\tanh S}{S} \right) \quad (B-4)$$

²The author is indebted to Dr. K. C. Reddy for suggesting this method.

$$\begin{aligned}
\frac{\partial G}{\partial h} = & -b \left(\frac{a + b T_{aw}}{\pi d l h^2} \right) \left(1 - \frac{\tanh S}{S} + \frac{S \operatorname{sech}^2 S - \tanh S}{2S} \right) \\
& - \frac{b^2 (T_{aw} - T_s)}{4hS\pi d} \left(\frac{\operatorname{sech}^2 S}{\sqrt{hdk_w}} - \frac{\tanh S}{lh} \right) \\
& - \frac{b^2 (T_{aw} - T_s)}{2hS\pi d} \left[\frac{S (\operatorname{sech} S)^2 \tanh S}{\sqrt{hdk_w}} - \frac{\operatorname{sech}^2 S}{2\sqrt{dk_w h}} \right. \\
& \left. + \frac{S \operatorname{sech}^2 S}{2lh} - \frac{\tanh S}{lh} \right] \quad (B-5)
\end{aligned}$$

$$\frac{\partial G}{\partial T_{aw}} = \frac{b^2}{\pi d l h} \left(1 - \frac{\tanh S}{S} \right) + \frac{b^2}{2S} \left(\frac{\operatorname{sech}^2 S}{\pi d \sqrt{hdk_w}} - \frac{\tanh S}{\pi d l h} \right) \quad (B-6)$$

Equations (B-1) through (B-6) are then substituted into the following two equations, which are the Taylor series approximations of F and G.

$$F(h_i, T_{aw_i}) = \Delta h_i \left. \frac{\partial F}{\partial h} \right|_i + \Delta T_{aw_i} \left. \frac{\partial F}{\partial T_{aw}} \right|_i \quad (B-7)$$

$$G(h_i, T_{aw_i}) = \Delta h_i \left. \frac{\partial G}{\partial h} \right|_i + \Delta T_{aw_i} \left. \frac{\partial G}{\partial T_{aw}} \right|_i \quad (B-8)$$

Solving the above two equations for Δh_i and ΔT_{aw_i} , then the improved values for $(i + 1)^{th}$ iteration are

$$h_{i+1} = h_i - \Delta h_i$$

$$T_{aw_{i+1}} = T_{aw_i} - \Delta T_{aw_i}$$

and one goes on to find better approximations until the assigned convergence requirements are satisfied.

APPENDIX C

SOLUTION FOR M AND T_o

The Newton-Raphson iteration scheme is also employed for the numerical calculation of M and T_o . The details are described as follows. Equations (16) and (17) can be rearranged as

$$F(T_o, M) = \frac{hd}{k_o} - \xi(Re_o) \psi(Re_o, M) \quad (C-1)$$

$$G(T_o, M) = \frac{T_{aw}}{T_o} - \eta_c - \bar{\eta}_* (\eta_f - \eta_c) \quad (C-2)$$

Then the approximated equations for F and G at the i^{th} iteration are:

$$F(T_{o_i}, M_i) = \Delta T_{o_i} \left. \frac{\partial F}{\partial T_o} \right|_i + \Delta M_i \left. \frac{\partial F}{\partial M} \right|_i \quad (C-3)$$

$$G(T_{o_i}, M_i) = \Delta T_{o_i} \left. \frac{\partial G}{\partial T_o} \right|_i + \Delta M_i \left. \frac{\partial G}{\partial M} \right|_i \quad (C-4)$$

The partial derivatives of F and G with respect to T_o and M are:

$$\frac{\partial F}{\partial T_o} = - \frac{0.86 \text{ hd}}{6.7 \times 10^{-5} \times T_o^{1.86}} - \left(\psi \frac{\partial \xi}{\partial Re_o} - \xi \frac{\partial \psi}{\partial Re_o} \right) \frac{\partial Re_o}{\partial T_o}$$

$$(k_o = 6.7 \times 10^{-5} T_o^{0.86} \text{ BTU ft}^{-1} \text{ hr}^{-1} \text{ } ^\circ\text{R}^{-1})$$

$$\frac{\partial F}{\partial M} = - \psi \frac{\partial \xi}{\partial Re_o} \frac{\partial Re_o}{\partial M} - \xi \frac{\partial \psi}{\partial M}$$

$$\frac{\partial G}{\partial T_o} = - \frac{T_{aw}}{T_o^2} - \frac{0.589 (\eta_f - \eta_c) Kn_\infty^{0.193}}{(0.493 + Kn_\infty^{1.193})^2} \frac{\partial Kn_\infty}{\partial T_o}$$

$$\begin{aligned} \frac{\partial G}{\partial M} = & - \frac{0.206 M^{2.5}}{(1.175 + M^{3.5})^2} - \frac{0.589 (\eta_f - \eta_c) Kn_\infty^{0.193}}{(0.493 + Kn_\infty^{1.193})^2} \frac{\partial Kn_\infty}{\partial M} \\ & + \frac{0.516 \bar{\eta}_* M^{1.8}}{(0.8521 + M^{2.8})^2} \end{aligned}$$

where

$$\begin{aligned} \frac{\partial \xi}{\partial Re_o} = & [0.14 + 0.230 \left(\frac{Re_o^{0.7114}}{15.44 + Re_o^{0.7114}} \right) \\ & + \left(\frac{0.01569}{0.3077 + Re_o^{0.7378}} \right) \left(\frac{15}{15 + Re_o^3} \right)] \end{aligned}$$

$$\times [n \operatorname{Re}_O^{n-1} - \frac{0.862 (\ln \operatorname{Re}_O) \operatorname{Re}_O^n}{\operatorname{Re}_O^{0.3287} (2.571 + \operatorname{Re}_O^{0.6713})^2}]$$

$$+ \operatorname{Re}_O^n \left[\frac{2.524 \operatorname{Re}_O^{-0.2886}}{(15.44 + \operatorname{Re}_O^{0.7114})^2} \right.$$

$$- \frac{0.7065 \operatorname{Re}_O^2}{(0.3077 + \operatorname{Re}_O^{0.7378}) (15 + \operatorname{Re}_O^3)^2}$$

$$\left. - \frac{0.1737 \operatorname{Re}_O^{-0.2622}}{(15 + \operatorname{Re}_O^3) (0.3077 + \operatorname{Re}_O^{0.7378})^2} \right]$$

$$\frac{\partial \psi}{\partial \operatorname{Re}_O} = - \frac{5.01 \operatorname{Re}_O^{0.109}}{(2.765 + \operatorname{Re}_O^{1.109})^2} \left[1 + \left(0.30 - \frac{0.065}{M^{1.67}} \right) \left(\frac{\operatorname{Re}_O}{4 + \operatorname{Re}_O} \right) \right]$$

$$+ [1.834 - 1.634 \left(\frac{\operatorname{Re}_O^{1.109}}{2.675 + \operatorname{Re}_O^{1.109}} \right)]$$

$$\times \left[\left(0.30 - \frac{0.065}{M^{1.67}} \right) \left(\frac{2}{4 + \operatorname{Re}_O} \right)^2 \right]$$

$$\frac{\partial \psi}{\partial M} = - \frac{0.6039}{M^2} + \frac{1.0929 M^{0.9173}}{(1 + M^{1.222})^{2.569}} + \frac{\partial \psi}{\partial \operatorname{Re}_O} \frac{\partial \operatorname{Re}_O}{\partial M}$$

$$+ [1.834 - 1.634 \left(\frac{\operatorname{Re}_O^{1.109}}{2.675 + \operatorname{Re}_O^{1.109}} \right)] \left[\left(\frac{\operatorname{Re}_O}{4 + \operatorname{Re}_O} \right) \left(\frac{0.1085}{M^{2.67}} \right) \right]$$

$$Re_O = \sqrt{\gamma g / R} \frac{p_s d M}{1.04 \times 10^{-7} T_O^{1.26}} \left(1 + \frac{\gamma-1}{2} M^2\right)^{.5}$$

$$(\mu_O = 1.04 \times 10^{-7} \times T_O^{.76} \quad lb_m \sec^{-1} ft^{-1})$$

$$\frac{\partial Re_O}{\partial T_O} = \sqrt{\gamma g / R} \frac{p_s d M (-1.26)}{1.04 \times 10^{-7} \times T_O^{2.26}} \left(1 + \frac{\gamma-1}{2} M^2\right)^{.5}$$

$$\frac{\partial Re_O}{\partial M} = \sqrt{\gamma g / R} \frac{p_s d}{\mu_O T_O^{.5}} \left[\left(1 + \frac{\gamma-1}{2} M^2\right)^{.5} + \frac{\frac{\gamma-1}{2} M^2}{\left(1 + \frac{\gamma-1}{2} M^2\right)^{.5}} \right]$$

$$Kn_\infty = \left(\frac{\pi \gamma}{2}\right)^{.5} \frac{M}{Re_O} \left(1 + \frac{\gamma-1}{2} M^2\right)^{.76}$$

$$\frac{\partial Kn_\infty}{\partial T_O} = - \left(\frac{\pi \gamma}{2}\right)^{.5} \left(1 + \frac{\gamma-1}{2} M^2\right)^{.76} \frac{M}{Re_O^2} \frac{\partial Re_O}{\partial T_O}$$

$$\begin{aligned} \frac{\partial Kn_\infty}{\partial M} = & \left(\frac{\pi \gamma}{2}\right)^{.5} \left[- \frac{\left(1 + \frac{\gamma-1}{2} M\right)^{.76}}{Re_O} + \frac{.76 (\gamma-1) M^2}{Re_O \left(1 + \frac{\gamma-1}{2} M^2\right)^{.24}} \right. \\ & \left. - \frac{M \left(1 + \frac{\gamma-1}{2} M^2\right)^{.76}}{Re_O^2} \frac{\partial Re_O}{\partial M} \right] \end{aligned}$$

Equations (C-3) and (C-4) can be solved for ΔT_{O_i} and ΔM_i ,
and better approximations can be obtained by

$$T_{O_{i+1}} = T_{O_i} - \Delta T_{O_i}$$

$$M_{i+1} = M_i - \Delta M_i$$

APPENDIX D

STATIC PRESSURE DISTRIBUTION DOWNSTREAM OF BASE

The surface pressure distributions downstream of the base are presented in Figures 55, 56 and 57 for three typical Reynolds numbers at each of the three Mach numbers $M_\infty = 2.5, 3.5$ and 5.07 . p is the measured static pressure, p_1 is the static pressure measured 2.5 inches from the leading edge, and x is the distance downstream from the base. The boundary layer before separation was always laminar except at the conditions $M_\infty = 2.5$, $Re_{\infty,L} = 1.96 \times 10^6$. The flow field was entirely laminar until after reattachment at the lowest Reynolds number. At the largest and intermediate Reynolds numbers, the transition took place somewhere in the free shear layer, and the reattachment was therefore turbulent.

In the pressure distribution, there is a hump in the midst of pressure recovery process and a local peak after the pressure is sufficiently recovered. This hump and local peak are attributed to the interaction of the lip shock with the wake shock [8, 20]. However, it is found that this hump and peak may exist simultaneously under certain conditions.

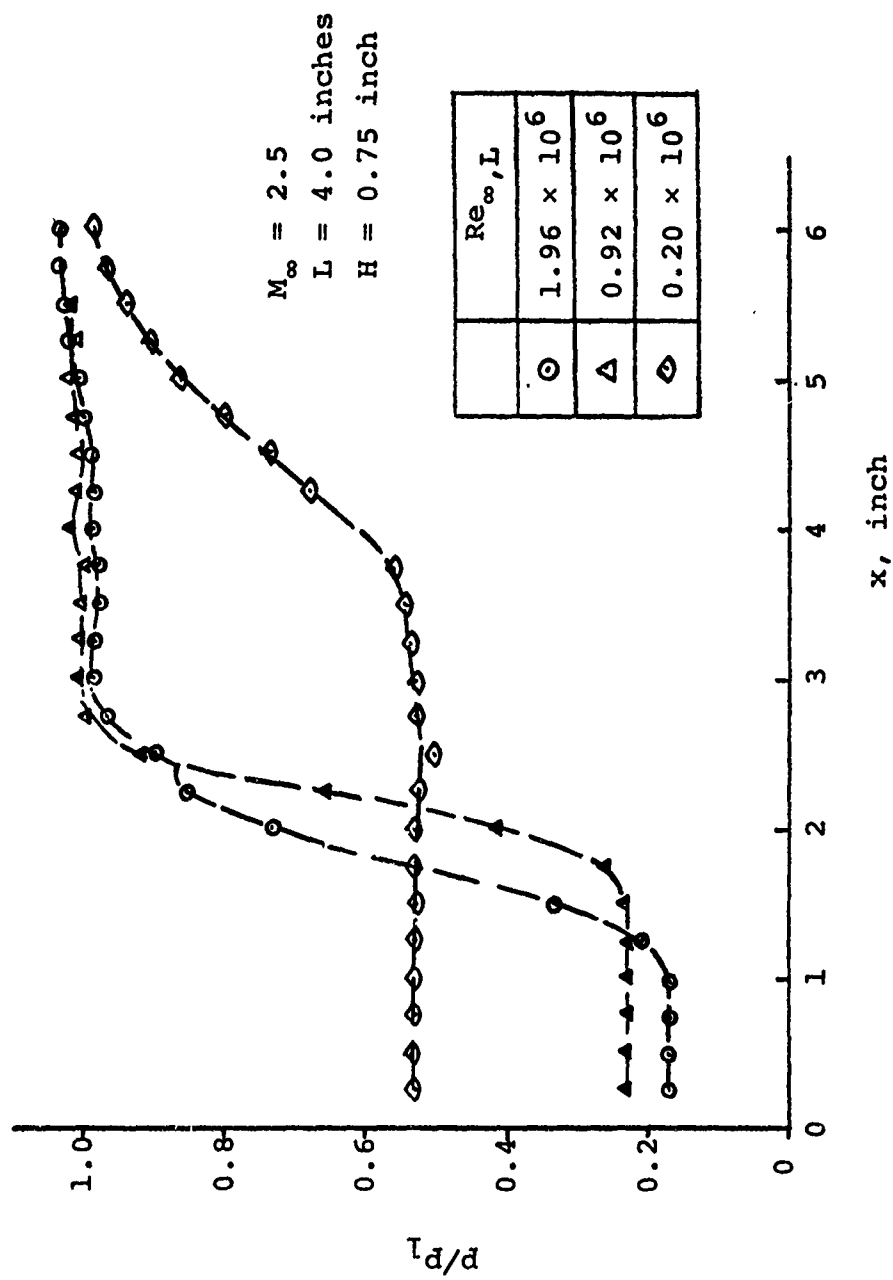


Figure 55. Pressure-Recovery Distribution at $M_\infty = 2.5$.

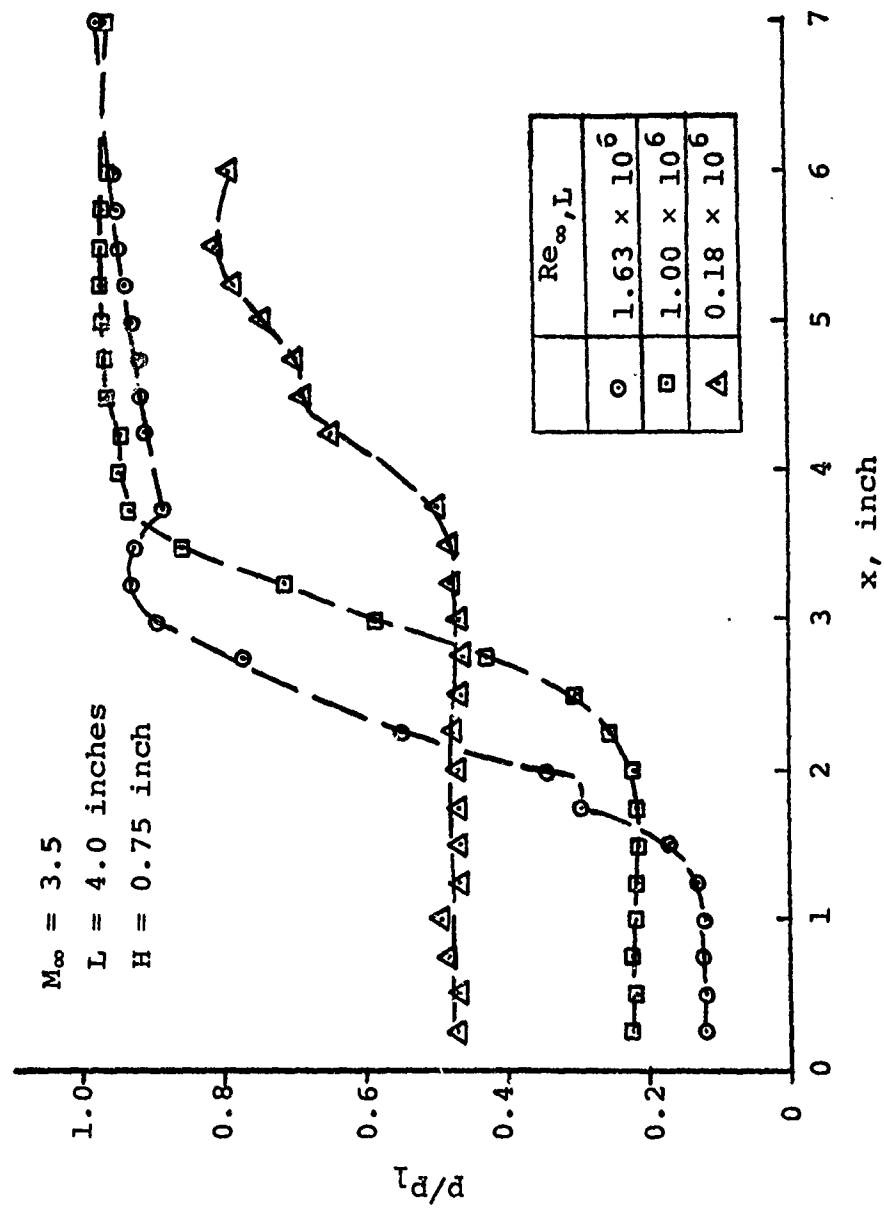


Figure 56. Pressure-Recovery Distribution at $M_\infty = 3.5$.

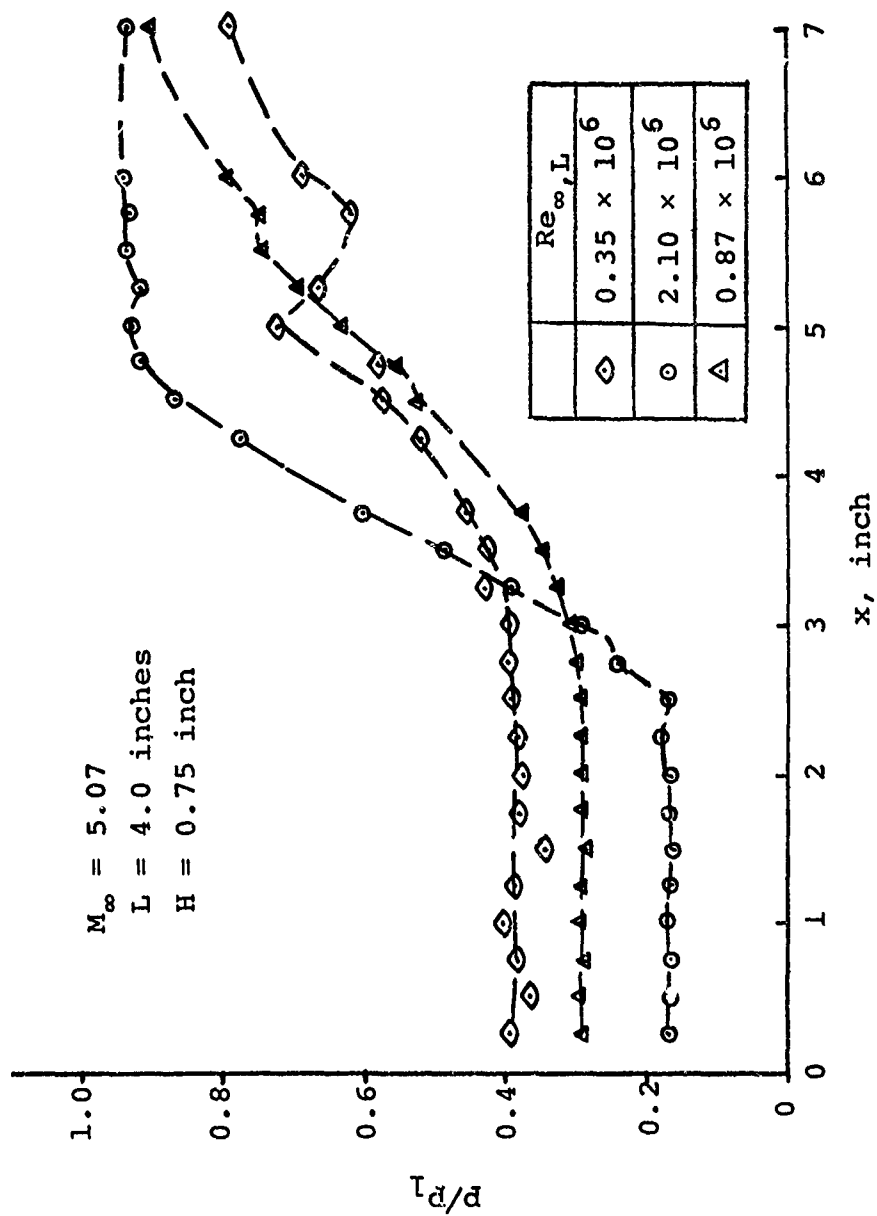


Figure 57. Pressure-Recovery Distribution at $M_\infty = 5.07$.

APPENDIX E

EFFECT OF VELOCITY FLUCTUATION ON RESISTANCE MEASUREMENTS

To simplify the analysis, the end losses due to heat conduction are neglected. The heat balance equation is then

$$I_m^2 R_m = hA(T_m - T_{aw}) \quad (E-1)$$

The convective heat transfer formula is also assumed to take the simplified form

$$Nu_o = c_1 + c_2 Re_o^n \quad (E-2)$$

Since only the velocity fluctuation is considered, Equation (E-2) becomes [53]

$$h = c_3 + c_4 U_{eff}^n \quad (E-3)$$

and

$$U_{eff}^2 = (\bar{U} + u')^2 + v'^2 + w'^2 \quad (E-4)$$

where \bar{U} is the steady velocity and u' , v' , w' , the fluctuation velocity component orthogonal to one another.

The instantaneous wire resistance is

$$R_m = \bar{R}_m + r' \quad (E-5)$$

Where \bar{R}_m is the steady resistance and r' is the fluctuation resistance due to velocity fluctuation.

The linear relationship between temperature and resistance is assumed

$$R = a + b T \quad (E-6)$$

Substituting Equations (E-3) and (E-6) into Equation (E-1), one obtains

$$I_m^2 R_m = \frac{1}{b} (R_m - R_{aw}) (c_5 + c_6 U_{eff}^n) \quad (E-7)$$

or

$$I_m^2 (\bar{R}_m + r') = \frac{1}{b} (\bar{R}_m + r' - R_{aw}) (c_5 + c_6 U_{eff}^n) \quad (E-8)$$

By series expansion

$$\begin{aligned} U_{eff}^n &= [\bar{U}^2 (1 + \frac{2u'}{\bar{U}} + \frac{u'^2 + v'^2 + w'^2}{\bar{U}^2})]^{n/2} \\ &= \bar{U}^n [1 + \frac{nu'}{\bar{U}} + \frac{n}{2} (\frac{u'^2 + v'^2 + w'^2}{\bar{U}^2}) + \dots] \end{aligned} \quad (E-9)$$

Substituting Equation (E-9) into (E-8), taking the mean time average and neglecting the higher order terms,

one obtains

$$\frac{\bar{R}_m}{R_{aw}} = \frac{c_6 \bar{U}^n (1 + \frac{n}{6} T^2) + c_5}{c_6 \bar{U}^n (1 + \frac{n}{6} T^2) + c_5 - I_m^2 b} \quad (E-10)$$

where

$$T = \frac{\left[\frac{1}{3} (u'^2 + v'^2 + w'^2) \right]^{0.5}}{\bar{U}}$$

which is the intensity of turbulence of a stream.

Expanding Equation (E-10) and neglecting the higher order terms, one gets

$$\frac{\bar{R}_m}{R_{aw}} = \left(\frac{c_6 \bar{U}^n + c_5}{c_6 \bar{U}^n + c_5 - I_m^2 b} \right) \left[1 - \frac{n}{6} \frac{T^2 c_6 \bar{U}^n I_m^2 b}{(c_6 \bar{U}^n + c_5) (c_6 \bar{U}^n + c_5 - I_m^2 b)} \right] \quad (E-11)$$

Bauer obtained the same expression using a different approach [54].

From Equation (E-7), one knows

$$\frac{I_m^2 b}{c_6 \bar{U}^n + c_5} \approx \frac{R_m - R_{aw}}{R_m}$$

also

$$\frac{c_6 \bar{U}^n}{c_6 \bar{U}^n + c_5 - I_m^2 b} \approx 1$$

$$0.5 < n < 1$$

If one assumes a 10 percent velocity fluctuation in the shear layer and recirculating region, then the percentage decrease in measured resistance due to turbulence is

$$\frac{n}{6} \left(\frac{c_6 \bar{U}^n}{c_6 \bar{U}^n + c_5 - I_m^2 b} \right) \left(\frac{I_m^2 b}{c_6 \bar{U}^n + c_5 - I_m^2 b} \right) T^2$$

$$\approx \frac{1}{6} \left(1 - \frac{R_{aw}}{R_m} \right) T^2 \approx \frac{(.04) (.01)}{6} = .000067 \ll 1$$

Therefore, one may conclude that the effects of turbulence on the resistance measurement is negligibly small.

APPENDIX F

REMARKS ON HOT-WIRE MEASUREMENTS

1. HOT-WIRE DIAMETER AND UNCERTAINTIES

As discussed in Chapter III, it is very difficult to apply the conventional calibration technique for hot-wire measurements in low Reynolds number compressible flow. However, the technique which relies completely upon the empirical heat transfer correlation formula is by no means perfect. There are inherited difficulties and uncertainties associated with this technique.

The diameter of the hot-wire is about 0.0002 inch. It cannot be made exactly circular and uniform. The cross-section of the wire may be elliptical or irregular, and there is no unique way of determining the wire diameter. If one assumes that the wire is circular and of uniform cross-section, then the wire diameter can be determined by

$$R = \frac{\rho l}{\pi d^2/4}$$

where R is the total resistance of the wire of length l and cross-sectional area $\pi d^2/4$, and ρ is the resistivity of the material.

The wire diameter was estimated to be 0.000217 inch by the above equation and with the following information (ρ supplied by wire manufactueres).

$$l = 0.1354 \pm 0.0002 \text{ inch}$$

$$R = 26.57 \text{ ohm}$$

$$\rho = 7.261 \times 10^{-6} \text{ ohm inch}$$

Since the hot-wire diameter is about seven wavelengths of visible light, optical methods for determining the wire diameter are not very accurate.

The physical constants of the materiel are not available for extremely thin wires. For instance, the wire thermal conductivity may be different from that of the same materiel with larger dimensions. This may introduce some error in calculating the conduction heat transfer to the hot-wire supports.

The reduced results of the hot-wire measurements depend entirely on the accuracy of the correlation formulas. These correlation formulas are not likely to be sufficiently accurate at the hypersonic and transonic Mach numbers. It is also very difficult to obtain satisfactory correlation formula at low Reynolds number and in the low subsonic range, since the data in this regime are very limited and diverged.

2. RADIATION HEAT LOSS

The radiation heat transfer from the hot-wire was neglected in the data reduction, and it remains to be justified. The ratio of the radiation heat loss to the convective heat transfer is

$$\frac{Q_r}{Q_h} = \frac{\sigma(T_m^4 - T_o^4)}{h(T_m - T_{aw})}$$

where σ is the Stefan-Boltzmann constant.

The calculated results given below show that even at the low Nusselt number radiation from the hot-wire is negligible.

M	Re _o	Nu _o	h	T _m , °R	T _{aw} , °R	Q _r /Q _h
3.4	4.4	0.544	468	590	582	0.0073
1.2	1.06	0.214	172	580	553	0.0088
0.34	0.27	0.155	125	570	521	0.0017

where h is in BTU/hr ft² °F and $T_o = 560^\circ\text{R}$.

3. NATURAL CONVECTION

Along the minimum velocity line in the recirculating region, the velocity may be very low and the velocity induced by buoyancy may be of equal magnitude. The natural convection shall be considered in the heat transfer analysis. However, as indicated in Chapter III, when the Mach number was less than 0.3, no converged solution was obtained.

When the Mach number is greater than 0.3, the velocity induced by buoyancy is small compared to the total velocity. Therefore, it is reasonable to neglect the gravity effect in the analysis of forced convection from the heated wire.

4. COMPARISON OF MEASURED RESISTANCES

Figure 51 shows the resistance traces for three different currents at a typical station. The comparison can be better explained by the following equation for the measured resistance, i.e.,

$$R_m = \frac{a + b (\eta T_o / \psi_R)}{1 - (\psi_n I_m^2 b / h A)}$$

which is derived from the hot-wire heat transfer equation with the conventional end loss correction factors.

The above equation shows that the effect of h on the measured resistance is amplified by I_m^2 . At very small current, the convective heat transfer has practically no influence on the wire resistance; and the wire measures essentially the recovery wire temperature. At the higher heating current, the relative contributions of h and I_m^2 on R_m depend on their magnitudes. Note, the changes in resistance traces when the current is increased from 1 to 7 and to 9 milliamps as indicated in Fig. 58.

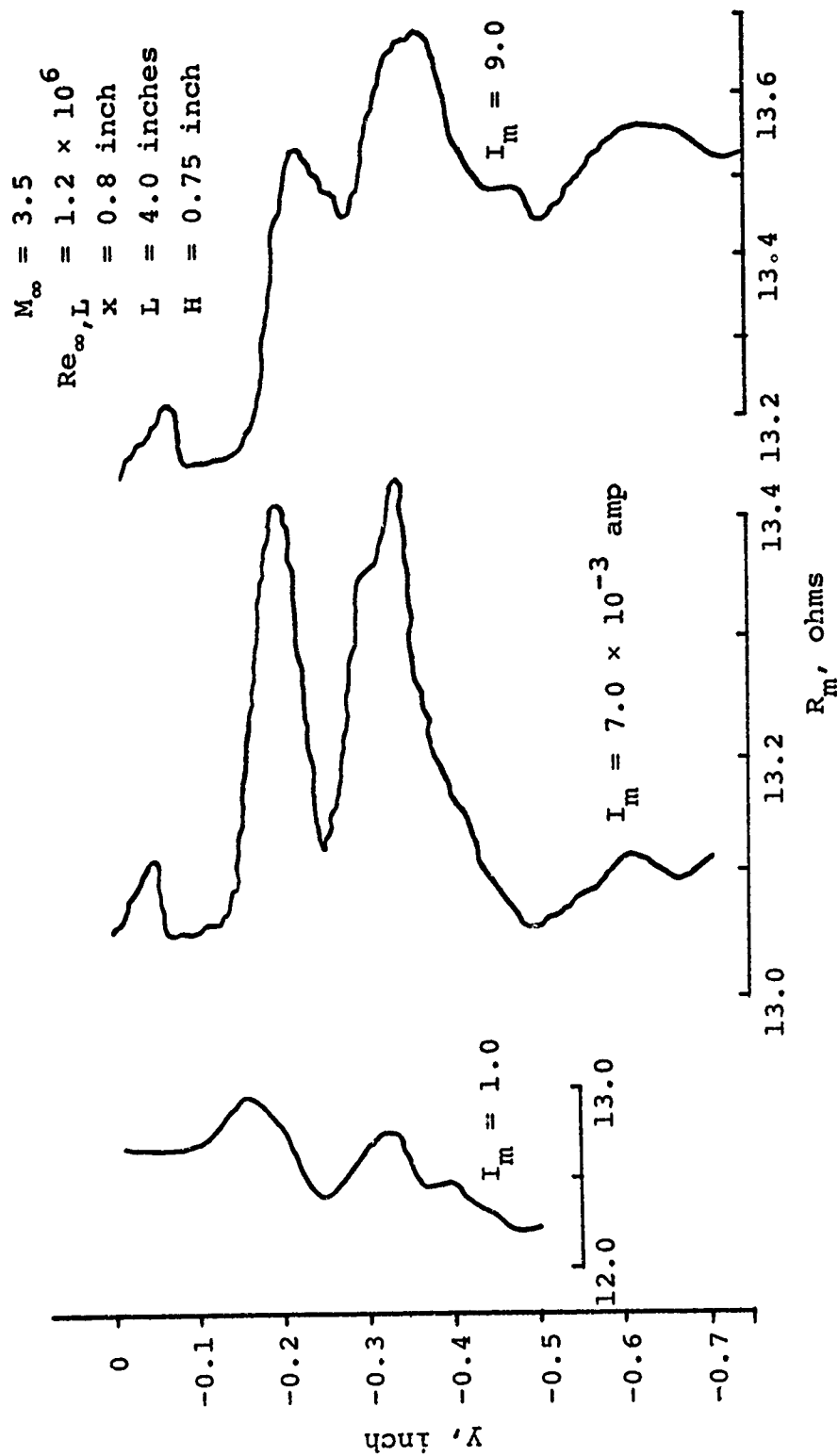


Figure 58. Comparison of Hot-Wire Resistances at Three Input Currents.

5. RECOVERY FACTOR IN TRANSITIONAL REGIME

The correlation of recovery temperature was discussed in detail by Dewey [34]. The recovery temperature was correlated by Equation (17) in terms of normalized recovery ratio $\bar{\eta}_*$, Mach number and Knudsen number. The recovery factor in the transitional regime was computed based on Equation (17), and is shown in Figure 59.

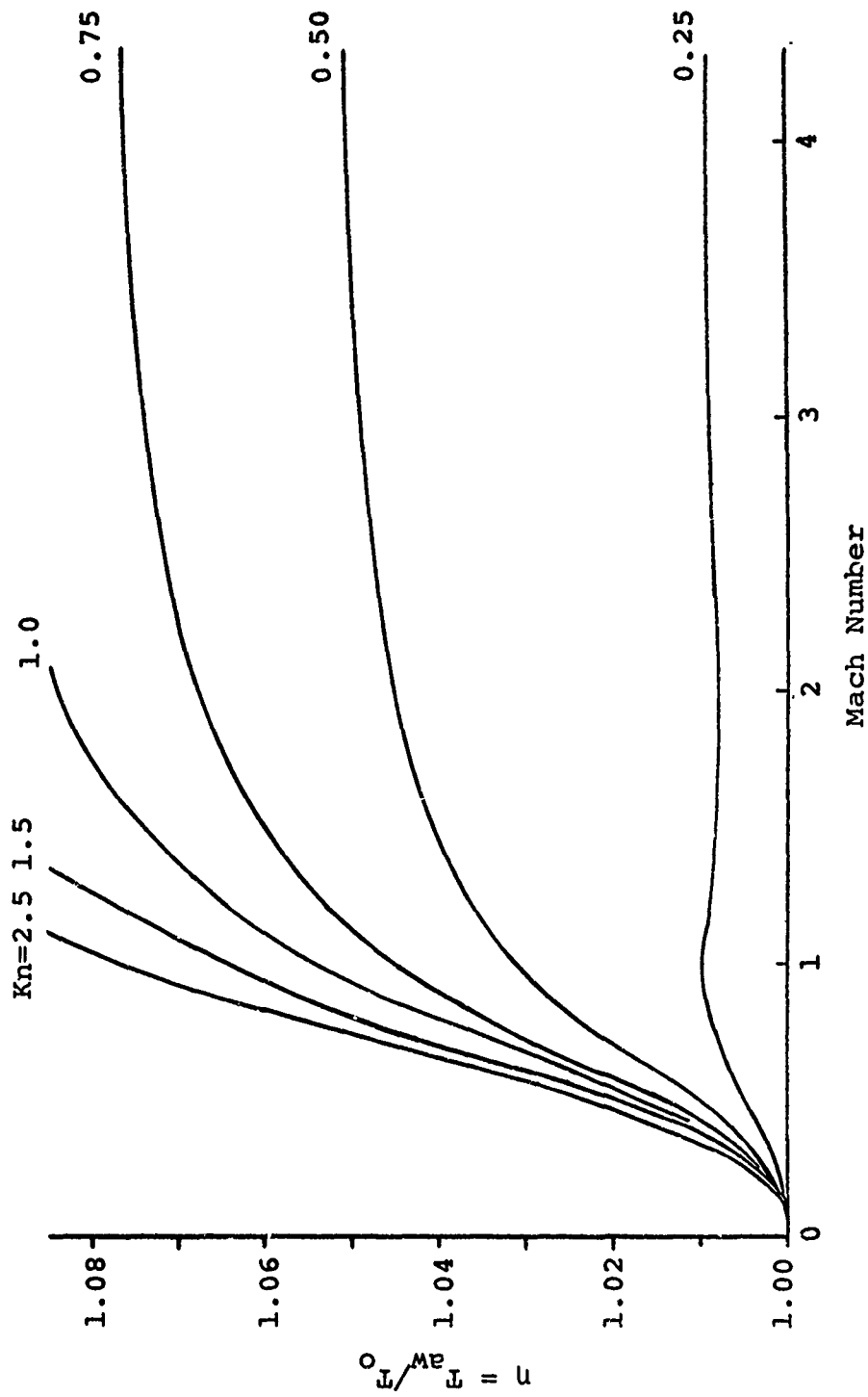


Figure 59. Recovery Factor in Transitional Regime.

APPENDIX G

ORIFICE DIMENSIONS

The detailed orifice dimensions in the wind tunnel model as shown in Figure 2, page 8, are presented in Table II.

Table II
ORIFICE DIMENSIONS IN WIND TUNNEL MODEL

Orifice Number	x	z	Orifice Number	x	z	Orifice Number	y	z
1	-1.520 ^a	0	27	2.270	-0.093	12.	-0.0375	0.664
2	-1.012	0.634	28	2.520	-0.187	13	-0.0625	0.610
2R	-1.000	1.500	29	2.770	0.187	14	-0.1080	0.542
2L	-1.000	-2.500	30	3.020	0.093	15	-0.2040	0.369
3	-0.760	0.120	31	3.270	0	16	-0.3520	0.120
4	-0.504	-0.392	31A	3.270	-2.625	17	-0.5020	-0.133
5	-0.386	-0.664	32	3.520	-0.093	18	-0.6550	-0.378
6	-0.264	-0.908	33	3.770	-0.187			
7	-0.190	-1.046	34	4.020	0.187			
8	-0.134	1.378	35	4.270	0.093			
9	-0.106	-1.220	36	4.520	0			
10	-0.062	-1.380	37	4.770	-0.093			
11	-0.038	-1.998	38	5.020	-0.187			
19	0.270	0.187	39	5.270	0.187			
20	0.520	0.093	40	5.520	0.093			
21	0.770	0	41	5.770	0			
21A	0.770	2.625	41A	5.770	2.375			
22	1.020	-0.093	42	6.020	-0.093			
23	1.270	-0.187	43	7.020	-0.187			
24	1.520	0.187	44	8.020	0.093			
25	1.770	0.093	45	9.020	-0.093			
26	2.020	0	46	10.770	0			
			46A	10.770	-2.375			

Orifice Diameter:
Upstream of Step 0.033
Vertical Face of Step 0.031
Downstream of Step 0.064

^aAll dimensions in inches